Processes affecting cirrus clouds life cycle at the tropical tropopause layer : contributions from the Stratéole-2 campaigns

Milena Corcos

Ecole doctorale n° 129
Sciences de l'environnement d'île-de-France.
Laboratoire de Météorologie Dynamique / Equipe DPAO

Processes affecting cirrus cloud life cycle at the tropical tropopause layer: contributions from the Stratéole-2 campaigns.

Par Milena Corcos
Thèse de doctorat de sciences du climat et de l'atmosphère
Dirigée par Albert Hertzog et Riwal Plougonven

Soutenue publiquement le 10 Mars 2023
Devant un jury composé de :

Hélène Chepfer, *professeure*, Sorbonne Université	**Présidente**
Bernd Kärcher, *professeur*, Deutsches Zentrum für Luft-und Raumfahrt	**Rapporteur**
Ulrich Achatz, *professeur*, Johann Wolfgang Goethe Universität	**Rapporteur**
Claudia Stephan, *chargée de recherche*, Max Planck Institute für Meterologie	**Examinatrice**
Claudia Stubenrauch, *directrice de recherche*, CNRS	**Examinatrice**
Emmanuel Rivière, *maître de conférences*, Université de Reims	**Examinateur**
Riwal Plougonven, *Professeur*, Ecole Polytechnique	**Directeur de thèse**
Albert Hertzog, *maître de conférences*, Sorbonne Université	**Co-Directeur de thèse**

Remerciements

J'aimerais tout d'abord remercier très chaleureusement mes deux encadrants de thèse, Albert et Riwal. Albert que je suis depuis mon stage de M1 sur des thématiques de dynamique tropicale, et qui m'a ensuite emmenée par deux fois en campagne dans cette région pour définitivement me convertir aux observations ballons. Merci à vous deux pour toutes nos conversations enrichissantes, captivantes sur le plan scientifique, et pleines de conseils précieux sur un plan plus humain, dans cette période importante entre les études et les premiers pas dans le monde de la recherche, mais encore plus dans un contexte sociétal troublé par une pandémie, une guerre et un défi climatique effrayant. Je voudrais les remercier pour leur enthousiasme, soutien, et leur confiance tout au long de la thèse, qui m'ont permis de pleinement profiter et apprécier ces quelques années qui ne sont que passées trop vite ! Merci aussi à Aurélien pour sa participation très constructive à mon encadrement, pour toutes ses remarques enthousiastes et ses questions pertinentes. J'ai adoré travailler avec vous trois. Mais notre petite équipe Stratéole-2 ne s'arrête pas là. Cette expérience de thèse n'aurait pas eu le même caractère sans Claire et Julio, que j'aimerais aussi grandement remercier. Merci de m'avoir ouverte aux instruments d'observations et d'avoir été si présents notamment en campagne pour me montrer vos activités. Nos discussions pleines d'humour et de bonne humeur ont changé mon quotidien. Enfin, merci à Cécile pour son soutien et ses conseils, Karim et Julien pour l'aide informatique, ainsi qu'à Sophie pour les rappatriements de données sur demande!

Outre-Atlantique, un grand merci à Martina et Joan pour leur accueil très chaleureux pour ma première expérience de stage à l'étranger, au NWRA. Merci pour leur apport très constructif et leurs explications sur les ondes de gravité, ainsi que leurs questions pertinentes lors de discussions scientifiques. J'aimerais aussi remercier Chris, Laura et Tyler pour leur accueil et sans qui cette expérience aux Etats-Unis n'aurait pas été aussi réussie.

Je suis très reconnaissante envers les membres de mon comité et jury de thèse, merci à Bernd Kärcher pour tous ses conseils et suggestions lors de nos conversations enrichissantes sur la microphysiques, en zoom et lors de sa visite à Paris. Merci aussi à Claudia Stubenrauch et Gwenael Berthet pour leur regard et questions sur mon travail. Je voudrais aussi remercier Ulrich Achatz, Claudia Stephan, Emmanuel Rivière, Hélène Chepfer pour m'avoir aussi fait l'honneur de participer à mon jury de thèse.

Mes remerciements s'adressent également à mes coboureaux, tout d'abord à Assia, avec qui nous nous sommes soutenues depuis le stage de M2, puis lors des oraux de thèse, et à chaque moment un peu difficile de ces trois années. Merci aussi à Clément, Jean et Alessandro. Nous avons lancé la tradition du gâteau hebdomadaire, qui j'espère restera même après nos départs respectifs. Merci aux autres doctorants de ma promotion, Doug biensûr, mais aussi Evangelos, et enfin merci à tous les autres membres de la TDGMCPB team dont la bonne humeur et le sourire ont contribué à la réussite de cette thèse.

Enfin merci à mes amis et ma famille!

Abstract

This thesis focuses on the observation of gravity waves at the tropical tropopause layer (TTL) by superpressure balloons, and their impact on cirrus clouds.

First, the gravity wave activity is quantified thanks to in situ observations of superpressure balloons from the first two Stratéole-2 campaigns. The link between tropical deep convection and wave activity is demonstrated at a synoptic scale by the decrease of wave amplitude with distance to convective cell. The geographical variability of gravity wave activity, its intermittency, as well as its interannual variability are also studied.
In a second step, the impact of gravity waves on cirrus clouds is studied thanks to the combination of Lagrangian measurements of temperature fluctuations with a microphysics model representing the homogeneous nucleation, growth and sedimentation of ice crystals, as well as a very simplified representation of the wind shear. The impact of the waves on ice crystals population and the consequences on the evolution of cirrus clouds and their capacity to dehydrate the air masses during the ascent in the TTL is quantified. The results are compared with observations from the ATTREX campaign in the TTL over the Pacific Ocean, and demonstrate the importance of a realistic representation of waves in microphysics simulations. Finally, a sensitivity study to the amplitude of gravity waves is discussed for the cirrus structure and ice crystal population.
Keywords: Tropical tropopause (TTL), gravity waves, cirrus clouds, 1.5 dimension microphysics model, ice crystals sedimentation, long duration superpressure balloons.

Résumé

Cette thèse s'intéresse à l'observation des ondes de gravité dans la tropopause tropicale (TTL pour tropical tropopause layer) par ballons pressurisés, et à leur impact sur les cirrus.

Dans un premier temps, l'activité des ondes de gravité est quantifiée grâce aux observations in situ des ballons pressurisés des deux premières campagnes de Stratéole-2. Le lien entre la convection profonde tropicale et l'activité des ondes est démontré à l'échelle synoptique par la diminution de l'amplitude des ondes avec la distance aux cellules convectives. La variabilité géographique de l'activité des ondes de gravité, de leur intermittence, ainsi que leur variabilité inter-annuelle sont également évaluées.
Dans un second temps, l'impact des ondes de gravité sur les cirrus est étudié grâce à la combinaison des mesures lagrangiennes des fluctuations de températures avec un modèle de microphysique prenant en compte la nucléation homogène, la croissance et la sédimentation des cristaux de glace, ainsi qu'une représentation très simplifiée du cisaillement de vent. L'impact des ondes sur la population de glace et les conséquences sur l'évolution des cirrus ainsi que sur leur capacité à assécher les masses d'air lors de l'ascension dans la TTL est quantifié. Les résultats sont comparés avec les observations de la campagne ATTREX dans la TTL au-dessus de l'océan Pacifique, et démontrent l'importance de la représentation réaliste des ondes dans les simulations de microphysique.
Enfin, une étude de sensibilité à l'amplitude des ondes de gravité est discutée pour la structure des cirrus et la population de cristaux.
Keywords: Tropopause tropicale (TTL), ondes de gravité, cirrus, modèle de microphysique 1.5 dimensions, sédimentation des cristaux, balloons surpressurisés longue durée.

Résumé long en français

Cette thèse s'intéresse à l'observation des ondes de gravité dans la tropopause tropicale (TTL pour tropical tropopause layer) par ballons surpressurisés, et à leur impact sur le cycle de vie des cirrus tropicaux.

Dans un premier temps, l'activité des ondes de gravité est étudiée et mise en relation avec le flux environnant grâce aux mesures in situ des ballons surpressurisés des campagnes Stratéole-2. Une première question est de comprendre le lien entre ces ondes observées et leur environnement convectif. Les ballons surpressurisés sont des traceurs quasi lagrangiens qui fournissent des observations sur plus de 600 jours entre les deux campagnes de 2019 et 2021 avec une résolution temporelle de 30 s. Ces observations, dans le repère intrinsèque des ondes, donnent accès à tout le spectre des ondes de gravité. Les flux de quantité de mouvement sont calculés grâce aux observations de pression, et différenciés selon deux intervalles de périodes, entre 15min et 1h, et 15min et 1 jour. Les périodes inférieures à 15min sont coupées pour éviter que les mesures ne soient impactées par les oscillations neutres des ballons. Les ondes de hautes fréquences (période inférieure à 1h) représentent plus de 30% des flux de quantité de mouvements totaux.

La convection alentoure est étudiée grâce à des cartes de température de brillance mesurées par satellites géostationnaires (produit NOAA/NCEP GPM_MERGIR), avec une résolution horaire. Les régions convectives sont identifiées comme ayant une température de brillance inférieure à 235 K. La distance au complexe convectif le plus proche est choisie comme metrique représentant l'environnement convectif.

Tout d'abord, à l'échelle du systeme convectif, un cas d'étude (15 janvier 2020) d'observations ballons au-dessus d'un système convectif à l'est des Iles Salomon, montre que la génération des ondes de gravité se fait lors du développement de la convection, avant qu'elle n'atteigne un stade plus mature. Ensuite, toujours à l'échelle synoptique, la dépendance de l'amplitude des ondes à la distance du système convectif le plus proche est mise en évidence. Non seulement l'amplitude diminue de manière monotone en s'éloignant de la convection, mais cette diminution est plus marquée pour les ondes de plus hautes fréquences. Statistiquement, 90 % des flux de quantité de mouvement supérieurs à la moyenne ont été mesurés à moins de 400 km de la convection, ce qui confirme que la convection est la source principale des ondes de gravité aux tropiques. Enfin, la variabilité des flux de quantité de mouvement diminue avec la distance à la convection, mettant en évidence à la fois le caractère intermittent des sources convectives, mais aussi une valeur de fond (autour de 4 mPa pour l'intervalle "WF") loin des systèmes convectifs.

A l'échelle planétaire, une correspondance entre activité convective et activité des ondes de gravité est mise en évidence, avec des flux de quantité de mouvement plus élevés là où la convection est la plus active. La convection tropicale est omniprésente, avec plus de la moitié des mesures effectuées à moins de 200 km d'une cellule convective, ce qui contribue à diminuer l'intermittence globale des ondes de gravité tropicales. Cette dernière se révèle donc comme modérée par rapport aux observations extratropicales.
Enfin, la comparaison de ces résultats à l'échelle planétaire entre les campagnes Stratéole-2 de 2019 et 2021 montrent la robustesse de la méthode, avec des valeurs comparables dans les régions convectives les plus actives, et des différences qui peuvent s'expliquer par différentes configurations convectives à l'échelle planétaire.

Un deuxième objectif est de quantifier la contribution au forçage de l'oscillation quasi-biennale (QBO), des ondes de gravité observées. Les deux campagnes ont eu lieu dans la phase est de la QBO, un peu plus près de la phase de transition pour la deuxième campagne, avec des vents légèrement plus faibles. Nous avons calculé pour les observations de 2019 que les ondes de gravité mesurées étaient responsables de près de la moitié du forçage de cette oscillation.

Le deuxième chapitre de cette thèse vise à décrire l'effet des ondes de gravité sur les cirrus in situ à la tropopause tropicale. L'approche utilisée pour aborder cette question est l'utilisation de simulations idéalisées de microphysique, combinées aux observations lagrangiennes des ondes de gravité, fournies par les ballons des campagnes Stratéole-2. Des scénarios simples sont explorés avec un modèle de microphysique suffisamment détaillé pour évaluer l'impact de cette dynamique petite échelle sur les caractéristiques microphysiques, essentielles pour comprendre le cycle de vie des cirrus et l'assèchement des masses d'air entrant dans la stratosphère.

Plus précisément, un modèle de microphysique inspiré de celui de Dinh et Durran a été implémenté pour décrire la nucléation homogène, la croissance diffusionnelle des cristaux, mais aussi l'effet de leur sédimentation différentielle ainsi qu'un mélange horizontal des masses d'air. La population de cristaux est décrite selon leur nombre et masse sur 36 bins de tailles, de $\sim$0.2 à $\sim$100 microns. Différentes simulations de complexité croissante sont présentées : d'abord, une simple ascension d'une parcelle d'air, puis l'ajout de dimensions sur la verticale et l'horizontale avec des colonnes de parcelles d'air, permettant la sédimentation et le mélange horizontal des cristaux par le cisaillement du vent. Dans toutes les simulations, les masses d'air suivent un profil vertical de température déduit des mesures de radiosondage, et montent à une vitesse faible de 0.5 mm/s, typique de la vitesse d'ascension à grande échelle dans la TTL. Les fluctuations de température induites par les ondes de gravité sont quand à elles directement déduites des observations des ballons Stratéole-2 et peuvent être superposées à cette ascension moyenne.

Ces simulations, et le cadre de la modélisation effectuée dans cette thèse en général, sont conçus pour explorer l'interaction des différents processus impactant les propriétés des cirrus in situ près de la tropopause tropicale, à savoir la nucléation, la croissance et la sédimentation des cristaux, les ondes de gravité et l'advection différentielle dans la verticale.

Le rôle de la sédimentation dans l'évolution de la population de cristaux de glace ainsi que dans la déshydratation associée est mise en évidence à l'aide de deux simulations simples complémentaires, représentant respectivement une sédimentation parfaite et une sédimentation différentielle des cristaux de glace. Dans ces simulations, les masses d'air ne sont pas impactés par les ondes de gravité. Cette première étape montre l'importance de chutes des cristaux (« fall streaks »). Dans un environnement sursaturé, les cristaux qui sédimentent peuvent grandir et atteindre des tailles bien plus grandes que celles atteintes pendant ou peu après la nucléation. Ils contribuent à déshydrater l'atmosphère sur un interval d'altitudes plus large que l'épaisseur des masses d'air où les cristaux nucléent.

Dans un second temps, l'impact des ondes de gravité sur la production de glace, la densité des cristaux et leur population est quantifié en comparant deux simulations similaires représentant l'ascension de masses d'air réparties sur plusieurs colonnes, l'une d'entre elles décrivant également la variabilité de la température induite par les ondes. Sans ondes de gravité, aucune nucléation de cristaux de glace n'est possible lorsque les masses d'air s'élèvent au-dessus du point froid de la tropopause. Les faibles taux de refroidissement de l'ascension lente génèrent une population de cristaux de glace plutôt étroite, avec un pic à 9 microns, différente des observations des campagnes ATTREX de 2014. En revanche, dans la simulation incluant les ondes de gravité, la production de glace est augmentée fortement avec de nombreux événements de nucléation générés à toutes les altitudes. L'augmentation des événements de nucléation et de la densité des cristaux de glace est une conséquence directe de l'augmentation des taux de refroidissement induits par les ondes. La distribution de la population de cristaux est élargie par la production de cristaux à différents moments avec un spectre plus large de taux de refroidissement, jusqu'à 4 K/h. Cette nouvelle distribution est plus proche des observations ATTREX, bien qu'aucun noyau de condensation n'ait été inclus dans les simulations. Ces résultats montrent l'importance d'une représentation réaliste des ondes de gravité pour reproduire les observations des cirrus dans la TTL. Enfin, nous avons constaté que les ondes de gravité augmentent significativement la fraction nuageuse près du point froid de la tropopause. Mais une étude plus précise de cette augmentation nécessiterait des simulations moins idéalisées.

Un deuxième objectif est de quantifier l'impact des ondes sur la déshydratation des masses d'air qui entrent dans la stratosphère. Dans la simulation sans les ondes, la déshydratation est plutôt faible avec une humidité relative diminuant seulement de quelques pourcents, associée à une faible production de cristaux de glace. La déshydratation près du point froid de la tropopause est presque nulle malgré des conditions initiales proches de la nucléation. La production de glace est fortement augmentée par les ondes de gravité. Les ondes sont associées à une diminution de 20% du rapport de mélange de vapeur d'eau pour les masses d'air qui ont pénétré la stratosphère. La déshydratation induite par les ondes au point froid est d'environ 2 ppmv. Enfin, nous avons mis en évidence que les nombreux petits cristaux générés par les ondes et advectés avec les masses d'air peuvent ne pas avoir d'impact direct sur la déshydratation, mais qu'ils peuvent arrêter la croissance des cristaux entrants qui sédi-

mentent à partir des masses d'air supérieures et ainsi réduire leur capacité de déshydratation.

Les observations ont montré que les fluctuations de température induites par les ondes de gravité ont un écart-type moyen de 1,5 K. Comme l'augmentation des taux de refroidissement par les ondes de gravité est déterminante dans la production de glace, l'impact de son évolution avec les amplitudes des ondes de gravité a également été étudié. Tout d'abord, lorsque toutes les fluctuations de température sont contraintes au même écart-type de 1,5 K, l'occurrence des densités de cristaux de 1 et 100 cristaux/L est augmentée, et les plus grandes concentrations sont diminuées. En effet, ces grandes concentrations sont créées dans les masses d'air qui subissent les plus grandes perturbations de température. La production de glace associée est encore plus proche de celles observées. Deuxièmement, la diminution de l'écart-type à 0.5 K donne des résultats plus proches de la simulation sans ondes, mais permet la nucléation au-dessus du point froid de la tropopause. Ce cas limite ainsi l'effet des ondesde gravité et pourrait être plus représentatif de la formation de cirrus régie par d'autres structures dynamiques plus grande échelle telles que les ondes planétaires. Enfin, à l'inverse, l'augmentation de l'amplitude des ondes avec un écart-type de 3 K génère des taux de refroidissement plus importants et diminue la taille moyenne de la population de cristaux.

Pour finir, l'effet des ondes sur la structure des nuages a également été abordé. Nous avons d'abord exploré deux situations simples opposées, avec l'effet des ondes de gravité complètement corrélé puis décorrélé d'une masse d'air à l'autre. Lorsque les fluctuations de température induites par les ondes sont complètement décorrélées, des cirrus apparaissent de manière aléatoire dans l'ensemble du domaine simulé. La structure du nuage est très hétérogène et différente des observations de cirrus. Les fluctuations de température associées aux ondes de gravité permettent la création de fins réservoirs de cristaux avec de fortes concentrations en glace, dans lesquelles l'humidité relative est proche de 1, ce qui pourrait rappeler certains profils des observations des campagnes ATTREX. En revanche, lorsque les fluctuations de température sont corrélées, ce qui pourrait être perçu comme plus réaliste au vu de la longueur d'onde verticale des ondes de gravité, des cirrus apparaissent à des périodes précises avec une structure plus homogène. Une structure plus stratifiée est également trouvée avec la diminution de l'amplitude des ondes ou la corrélation des fluctuations. Dans ce cas, des simulations plus longues pourraient permettre de représenter des nuages plus fins.

En guise de conclusion, nos résultats montrent l'importance d'un traitement couplé des observations des ondes de gravité et de la microphysique. Ils ont montré la portée d'une représentation réaliste de la variabilité de la température à petite échelle pour évaluer les propriétés et le cycle de vie des cirrus tropicaux.

Contents

List of Figures

List of Tables

List of symbols, acronyms and abbreviations

Symbol	Definition	Value (TTL)
	Chapter 1	
w_b	balloon vertical velocity (m/s)	
w	vertical wind velocity (m/s)	
ζ_ρ	altitude of isopycnal surface (m)	
$u_{\|\|}$	horizontal wind in wave direction of propagation (m/s)	
f	inertial frequency (rad/s)	$2\pi\sin\theta$ rad/s
N	Brunt-Väisälä frequency (rad/s) (in the stratosphere)	$\approx \frac{2\pi}{5min}$
M_a	air mass	
g	gravitational acceleration (m/s^2)	9.81
η	Added mass coefficient (for a sphere in a perfect fluid)	0.5
R	gas constant for dry air (J/kg/K)	287
H	density scale height (m) (in the stratosphere)	≈6000
ρ_a	air density at the balloon flight level as $\rho_a = RT_a/P_a$ (kg/m^3)	≈0.12
C_d	drag coefficient (in Antarctica)	0.5
c_p	specific heat at constant pressure per unit mass of air (J/kg/K)	1004
A_b	Cross sectional area of the balloon $\frac{\pi D_b^2}{4}$	D_b(TTL) = 11m
		D_b(STR) = 13m
M_b	Balloon system mass (kg)	≈ 100 kg
ω_b	balloon neutral oscillation frequency (rad/s)	$\frac{2\pi}{3-4min}$
$\hat{\omega}$	intrinsic wave frequency	
$\hat{c}$	intrinsic wave phase speed	
m	vertical wave number	

Symbol	Definition	Value (TTL)
	Chapter 2	
S_i	super saturation ratio with respect to ice	
p_v	partial pressure of water vapor (Pa)	
p_{sat}	saturation vapor pressure (Pa)	
k_b	Boltzmann constant (J/K)	1.38×10^{-23}
μ	chemical potential (J/mol)	
σ	surface tension of solution (J/m^2)	
ρ_{ice}	density of ice (kg/m^3)	918
v	molar volume (m^3/mol)	
ΔG	Gibbs free energy change (J)	
a_w	activity of solution	
J	nucleation rate coefficient (/vol unit /s)	
RH_i	relative humidity with respect to ice (%)	
γ	growth factor (m^2/s)	
D_v	water vapor diffusivity ($m^{-2}.s^{-1}$)	
α	deposition coefficient	
k_a	thermal conductivity of air (J/s/m/K)	
R_v	gas constant for water vapor (J/K/kg)	462
L_s	latent heat of sublimation (J/kg)	2.84×10^6
f	ventilation coefficient for thermal diffusion	
c_p	specific heat capacity (J/kg/K)	
M	molar mass of air (kg/mol)	29×10^{-3}
m_w	mass of a water molecule (kg)	3×10^{-26}
M_w	molar mass of water (kg/mol)	18×10^{-3}
R_e	Reynolds Number	
X	Davis Number	
C_D	drag coefficient	
A	cross sectional area (m^2)	
A_e	projected cross sectional area (m^2)	

Chapter 1

Introduction

Sommaire

1.1 The tropical tropopause layer

1.1.1 Definition and caracteristics of the Tropical Tropopause Layer

The transition between the troposphere and the stratosphere is well defined in the extra-tropics, with a sharp change in the stratification. Conversely, in the tropics, the interface between two different regimes, a fast ventilation during the day driven by convection in the troposphere, and a slower motion associated with the Brewer-Dobson circulation in the stratosphere, is more continuous. It is represented by the Tropical Tropopause Layer (TTL) where both regimes are found, making the level of this transition depending on the thermodynamic criteria and thus being a layer rather than a level. The TTL definition and location is motivated by large-scale dynamical structures. Its vertical extension as defined in Fueglistaler et al. (2009) ranges between 14 to 18.5 km (150 to 70 hPa): it starts above the main convective flow, as tropical deep convection most often detrains at altitudes of 10 to 15 km. From this altitude, the ascent of the air masses is no longer driven by convection but mainly by heating due to radiation. The TTL upper boundary is set at the average altitude of the highest clouds, the cirrus clouds, which are about 18 km. As for the latitudes, the TTL is limited by subtropical jets (30° latitude) (Haynes and Shuckburgh, 2000). The associated strong potential vorticity gradient acts as a barrier, limiting horizontal transport in the lower part of the TTL. Conversely, mixing and transport to higher latitudes is observed in the upper TTL. There is thus a difference between the upper TTL and the relatively isolated lower levels (Plumb, 1996).

At the base of the TTL, convection imposes a profile close to the wet adiabatic, but the cold temperature coupled with the low water vapour mixing ratios make the latent heat release small, the temperature profile is thus close to a dry adiabat. At about 17 km (90-100 hPa), the temperature reaches a minimum, the cold point tropopause, before the vertical gradient changes sign, so the top of the TTL is more stable.

The temperature is controlled mainly by radiative and convective forcing, its horizontal structure is influenced by the distribution of convection in the troposphere, while the vertical motion is dominated by the Brewer-Dobson circulation. From a dynamical point of view, the large-scale circulation of the upper troposphere, such as the Walker or Hadley cells, impact the lower part of the TTL, while the upper part is mainly influenced by the Quasi Biennial Oscillation (QBO) which modulates the zonal wind. It should be noted, however, that while the direct impact of convection decreases rapidly with altitude, the indirect effect through wave generation is persistent at higher levels.
Characteristics of the TTL are summed-up in figure 1.1, from Fueglistaler et al. (2009).

1.1.2 Importance of the TTL: a gateway to the stratosphere

Air enters the stratosphere from the troposphere mainly by ascending through the tropics, within the TTL (Brewer, 1949). There, the processes involved in troposphere-stratosphere transport are therefore essential for the composition of air masses entering the stratosphere. From the surface to the upper tropopause, air is lifted by convection via latent heat release.

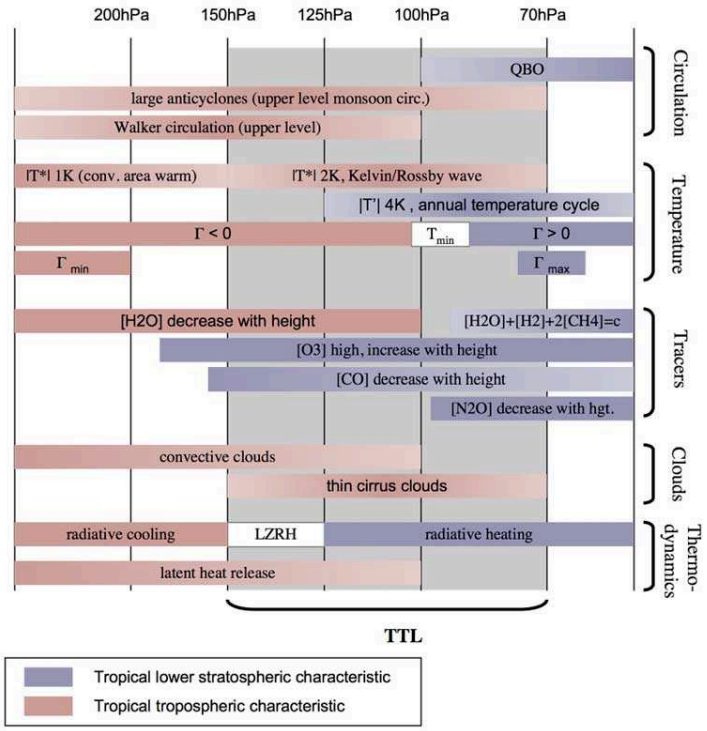

Figure 1.1: From Fueglistaler et al. (2009) Caracteristics of the TTL. $\Gamma = \frac{\mathrm{d}\bar{T}}{\mathrm{d}z}$, LZRH= level of zero radiative heating, $|T*|$ is the amplitude of temperature zonal anomalies, QBO is the Quasi Biennial Oscillation.

Convection does not rise high enough and is not sufficient to explain the transport of air masses to the cold point, despite convective overshoot or very rare convective towers which could transport the air directly to the stratosphere. Indeed, the flow transported by deep convection will subside again below the "level of zero net radiative heating" (LZRH), where radiative cooling is dominant. The altitude of the LZRH depends on the cloudy conditions, but in clear sky it is about 15km, therefore lower than the tropical tropopause cold point. Once high enough in the troposphere, the air masses are caught in the Brewer-Dobson circulation (figure 1.2), which is forced by the dissipation of synoptic and planetary scale waves (Holton et al., 1995; Plumb, 2002). The dissipation of these waves induces a poleward motion of air implying an ascent in the Tropics which generates cooling of air masses that stay in equilibrium with their environment. Holton et al. (1995) explained this air mass pumping as an effect of the wave drag from dissipation of upward propagating waves from the troposphere. Plumb (2002) calls it the "Rossby-pump" as the drag from dominant planetary-scale Rossby waves can only be eastward, resulting in a pumping action with the air driven poleward for angular conservation. The air is lifted in the tropics and pushed down in the middle and high latitudes. The discovery of this circulation explains the ozone and water vapour measurements in the tropics (Brewer (1949), Newell and Gould-Stewart (1981)).

Among all species that are transported through the TTL, water vapour is of particular importance. Air masses actually undergo a significant dehydration while ascending through a relatively humid troposphere to a rather dry stratosphere. Despite its low abundance, strato-

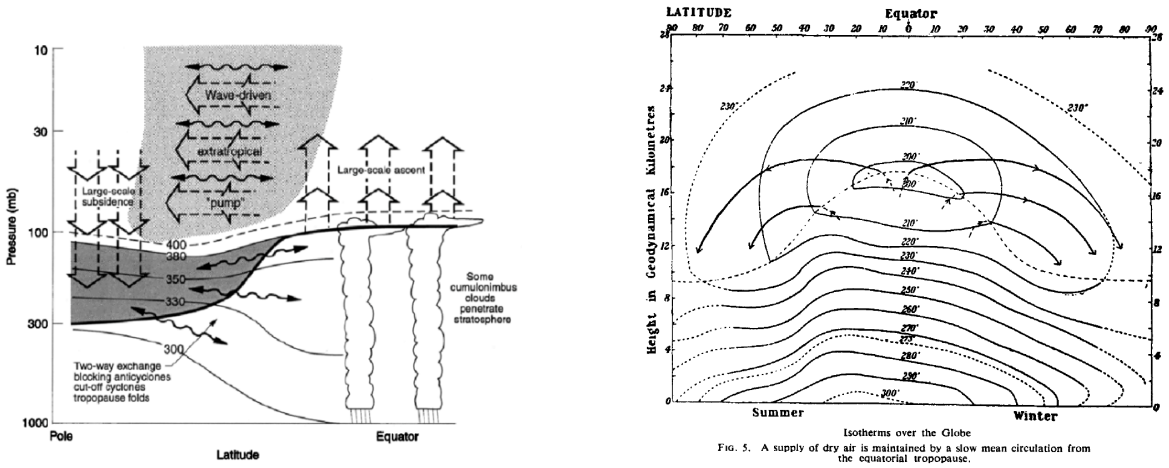

Figure 1.2: Brewer Dobson circulation from Brewer (1949), Holton et al. (1995).

spheric water vapour is essential to the chemistry (Solomon et al. (1986), Kirk-Davidoff et al. (1999)), and radiative balance of the stratosphere (de F.Forster and Shine, 2002; Solomon et al., 2010). Water is the most important greenhouse gas (Held and Soden, 2000) in gaseous form, as liquid droplets in clouds it also affects the earth's radiation balance. The dominant role of TTL transport to regulate the amount of water vapour entering the stratosphere was established for a long time (Brewer, 1949; Mote et al., 1996; Holton and Gettelman, 2001). For instance, it is well understood that the passage of air masses through the very low temperatures of the cold point tropopause limits water vapour mixing ratios to a few ppm (Brewer, 1949), but the detailed processes that control the precise level of dehydration of air masses passing through the TTL are not yet fully understood.

1.1.3 Importance of tropical cirrus clouds

Cirrus clouds are ubiquitous in the TTL. Satellite observations have shown horizontal extension of cirrus cloud systems up to 1000 of kms, and they were found to persist for several days in the tropics. Their importance in this region of lifting above the cold point was anticipated dynamically by Robinson (1980), Holton et al. (1995), Fueglistaler et al. (2009). Fine cirrus clouds have been detected by lidars on the ground, during airborne missions (McFarquhar et al., 2000), and from space (Wang et al., 1996). They are most often located below 16 km but sometimes up to 18 km and are particularly present over the Pacific warm pool (Fu, 2007).

Two processes of cirrus formation can be distinguished:
By detrainment, when the flow near the top of convective systems creates an anvil cloud. These clouds are characterized by a large ice water content. The large crystals sediment after only a few hours (Jensen et al., 1996) whereas the small crystals can form fine cirrus clouds which can persist after the dissipation of the cumulonimbus formed. They are usually called 'thin' cirrus (McFarquhar et al., 2000).
In situ: the ascent of air masses cools the air to its frost point, giving rise to optically fine cirrus clouds that can persist for several days if the crystals are fine enough (Jensen et al., 1996, 2010). These are often subvisible cirrus clouds.

Beyond their altitude and thickness, it is their microphysical characteristics such as the number of crystals, size distribution and shapes, that have a major influence on their life cycle and radiative properties (Smith et al., 1998). In addition, the size of the crystals determines their sedimentation speed and thus their efficiency in dehydrating air masses (Jensen et al., 2001): a small number of large crystals will dehydrate more efficiently than many small crystals. Also, the chemical reactions that take place on ice crystals are influenced by their size and number. Finally, for a given humidity, the final particle size will depend on the number of nucleated crystals.

Cirrus clouds impact on troposhere-stratosphere transport and radiative budget The limited measurements of the microphysical properties of cirrus clouds makes the understanding of their radiative impact complicated, especially for optically thin cirrus clouds. Lohmann and Roeckner (1995) argued that they have an impact on the global radiative budget. Subvisible cirrus clouds may only have a weak radiative heating that would not directly impact the surface, but their radiative effect on the dynamics of the upper troposphere is significant. Indeed, cirrus clouds may induce additional radiative forcing, enhancing the vertical transport in the TTL (Ueyama et al., 2015). Furthermore, in this region with a delicate balance between short-wave cooling and long-wave heating, thin and subvisible cirrus clouds with smaller heating rates are important (McFarquhar et al., 2000). Convective transport impacts low clouds whereas radiative transport is the main forcing for the transport of cirrus clouds through isentropes. Corti (2005) has shown that if convection is not sufficient to transport air masses beyond the LZRH level, the vertical transport due to cirrus clouds can be sufficient to feed the Brewer-Dobson circulation.

Cirrus clouds impact on dehydration Cirrus clouds radiative effect on the dynamics of the upper troposphere (Corti et al., 2006; Dinh and Fueglistaler, 2014) as well as their prevalence and long lifetime may be important and also act on the water vapour present (Rosenfield et al., 1998; Sherwood, 1999). High and cold cirrus clouds ($T<200$ K) influence the exchange of vapour between the troposphere and the stratosphere through their ability to dehydrate air masses entering the stratosphere (Brewer, 1949; Jensen et al., 1996; Dinh and Fueglistaler, 2014; Jensen and Pfister, 2004; Jensen et al., 2013). The large number of fine and high cirrus clouds in the TTL ($20-50\%$ of cirrus clouds) (Wang et al., 1996; Mace et al., 2009; Virts et al., 2010) indicates that they are generally the last ones to dehydrate air masses before they enter the stratosphere. Dehydration is achieved when ice crystals grow and sediment down a significant distance on the vertical before they start to sublimate (Dinh and Fueglistaler, 2014; Podglajen et al., 2016). The efficiency of this dehydration is still poorly quantified because it depends on the sizes and concentration of ice crystals (Kärcher et al., 2014) and thus on the type of nucleation.

1.2 Equatorial waves

1.2.1 Convection as a source of tropical waves

Solutions of shallow water equations on β plane Since the late 1950s, it was shown that the low-latitude region of a rotating planet could produce a special class of "trapped" motions along the equator (Yoshida, 1959; Bretherton, 1964). Matsuno (1966) solved a system of equations known as the "shallow water equations on an equatorial beta plane", which govern the motions in a fluid layer of constant density (shallow water) when the restoring forces are gravity and a linearly varying Coriolis parameter (beta plane), with zonally propagating wave solutions. These solutions correspond to the equatorial waves: namely the Kelvin, equatorial Rossby, westward and eastward inertial-gravity, and mixed Rossby-gravity waves, found in the atmosphere and the ocean. They are planetary scale waves. As early as the 1970s, spectral analysis of satellite tropical cloud cover data, strongly suggested a connection between the shallow water equatorial modes of Matsuno (Matsuno, 1966) and deep convection (Gruber, 1974; Zangvil, 1975; Zangvil and Yanai, 1980, 1981). For the convectively generated waves that were observed in the tropical UTLS, the source is associated with the diabatic heating by moist convection in the troposphere. Their vertical structure indeed indicates an upward propagation of energy, which requires a tropospheric forcing (Holton, 1972, 1973). Once generated, these waves are considered to be decoupled from convection or any other forcing.

Convectively generated gravity waves Gravity waves are of smaller scale than the tropical planetary waves. They are generated by a wide range of sources, such as convection, topography, wind shear and frontal systems (Fritts and Alexander, 2003). Unlike topographic waves, convective gravity waves are not characterized by a prominent ground-based period or phase speed, as convection generates a wide spectrum of waves with different time and space scales. The study of convection as a source of waves is challenging: first because of the highly transient nature of this source, and second as the propagation of lowest frequency waves are possible far from convection. Nonetheless, the link between convection and gravity waves has been observed and modeled. Idealized two-dimensional models showed that tropical squall lines were efficient sources of gravity waves (Fovell et al., 1992; Alexander et al., 1995; Alexander and Holton, 1997) and observations found a correspondence between deep convective clouds and gravity waves (Alexander and Pfister, 1995; Alexander et al., 2000; Sato et al., 1995; Dewan et al., 1998). In the tropical band, far from topography and baroclinic instability and in the most convective regions, observations showed that convection could trigger gravity waves (Tsuda et al., 1994; Karoly et al., 1996; Shimizu and Tsuda, 1997; Vincent and Alexander, 2000), and idealized models were able to reproduce the generation of gravity waves by convection (Mapes, 1993; Fovell et al., 1992; Lane et al., 2001; Piani et al., 2000). It was also found that the depth of convection was setting the amplitude of the generated waves, with their source point linked to the position of the developing convective cells. Furthermore, when convection was found to trigger gravity waves, convective gravity waves on the other hand impact the region around the convective cloud, communicating effects of latent heat from the cloud to its surroundings (Bretherton and Smolarkiewicz, 1989; Mapes, 1993; Shutts and Gray, 1994).

But how are these convective gravity waves generated ? Convection can be represented as a transient heat source, correlated to a change in the pressure and momentum field that will produce an atmospheric response. The generation mechanism of gravity waves in an overlying stable layer is complex and non linear but can be described with three main mechanisms, all of which are ultimately a response to a latent heating:

- the ***pure thermal forcing*** or diabatic heating term (1)
- the ***transient obstacle or moving mountain*** to the horizontal flow (or quasi stationary forcing), created by the rising convective element's pressure field, and requiring a mean flow relative to the convective element (2)
- the ***mechanical oscillator***, a thermal oscillation between updrafts and downdrafts that is causing the displacement of the isentropes at the base of the stable layer, exciting vertically propagating waves (3)

(1) The thermal forcing is associated with the latent heat release from convection, varying in time. This heat release will interact with overlying stable layers and shear, and produce buoyancy. This buoyancy source can be seen as a train of buoyancy pulses, in a moving stratified fluid (background flow) that will cause a downward displacement proportional to the strength of the pulse at the original heating position, creating a growing atmospheric response. The downward displacement is compensated by concentrated rising motions in the heated fluid as it is advected along with the mean flow (Fritts and Alexander, 2003). For the longer waves generated, the vertical wavelength of the generated wave is twice the depth of the heating (Salby and Garcia, 1987), but is divided by two by refraction when penetrating the stratosphere, so that the vertical stratospheric wavelength is similar to the depth of the tropospheric heating. For higher frequency waves, the vertical wavelength is larger, up to 4 times the heating depth (Holton et al., 2002). The produced wave field is isotropic but becomes anisotropic because of background wind filtering effects (Fritts and Alexander, 2003). The displacement field near the buoyancy source is dominated by small group velocities. McLandress et al. (2000) observed with a limb sounder the thermal forcing as a mechanism for gravity waves generation in convection, and Bretherton (1988), Chun and Baik (1998) modelled it.

(2) The transient obstacle mechanism can be seen as an atmospheric transient mountain's interaction with the background flow, and the gravity wave generation is almost topographic like. The heating from the convective element impacts the shape of the isentropes at the bottom of a stable layer, acting as a barrier to the environmental horizontal flow, and this modification evolves in time and space with the convective mountain/obstacle. This mechanism is the most effective when the updrafts or downdrafts are more persistent, as in mesoscale convective systems. The phase speed spectrum of the generated waves is affected by the time dependency of the obstacle, and their direction of propagation is opposite to the mean wind relative to the obstacle (it is therefore by nature non isotropic) (figure 1.3). Evidence of this obstacle effect for low frequency waves were recorded in radiosondes (Vincent and Alexan-

der, 2000), and it was also explicitly resolved in a linear approximation (Pfister et al., 1993b,a).

(3) The mechanical oscillator mechanism in a squall line/convective cell consists in convective overshot updrafts that form periodically and oscillate around their level of neutral buoyancy. It creates vertical velocity components up to the stratosphere, which generate waves with frequencies equal to the oscillation frequency. It is accompanied by a weaker oscillation from the stable surrounding air masses displacement from the rising updraft at the tropopause, which generates external wave modes propagating horizontally away from the updraft. Lane et al. (2001) represented this forcing as nonlinear sources in the form of momentum flux divergences and found that the oscillation of the air parcel was similar to the local tropospheric buoyancy, which limits the range of frequencies of the generated waves to high frequencies, when Fovell et al. (1992) found that the frequency of the oscillator was linked to the lifetime of each individual convective cell. The mechanical oscillator is symmetric in absence of mean wind, creating a symmetrical response, and the vertically propagating generated waves at the initial stage of the convection development are isotropic. The anisotropies are therefore created afterwards by background wind effects during propagation.

The relative prominence of the different mechanisms has been debated (Lane et al., 2001; Fritts and Alexander, 2003), as they are not distinct but coupled and the spectral characteristics of waves forced by diabatic and non linear forcings are similar (Song et al., 2003). However, more recent simulations have showed that mechanism 1 seems to dominate the others (Stephan and Alexander, 2015).

Observation of gravity waves As early as 1968, a breaking wave was already witnessed using a radar. Hicks and Angell (1968) were describing "an apparent horizontally twisted, braided, or helical-appearing atmospheric structure..." that proved to be a breaking gravity wave exciting a Kelvin-Helmotz instability (Fritts, 1979). At the same period of time, lidars enabled the study of gravity waves in California, over the Sierra Nevada Mountains, by the observation of waves structure in clouds (Collis et al., 1968). The observation of gravity waves given by the measurements of the induced perturbations (wave's signature) on dynamical variables, such as wind direction, temperature, but also atmosphere composition like trace gas or aerosols concentrations. For example, to have access to vertical and horizontal wavelengths, intrinsic frequency, phase speed and propagation direction of the waves, lidars were also used to study variations of chemical composition of the atmosphere created by the waves (Gardner and Shelton, 1985), whereas infrared spectrometers (Ern et al., 2004) provided temperature profiles that allow the retrieval of the amplitude, phase and vertical wavelength of gravity waves. These measurements can be performed remotely, either from the ground (meteorological stations) or space (radars, lidars in satellites), or in situ with radiosondes, superpressure balloons, or even airplanes. Depending on the observational technique, different wave characteristics are estimated with more or less uncertainty. From radiosondes one can attempt an estimate of the phase speed, but as this is a more derived quantity, it will be more uncertain than vertical wavelength. Therefore it can be useful to use different and complementary techniques, to achieve a more complete representation of the waves forcing and interaction on the

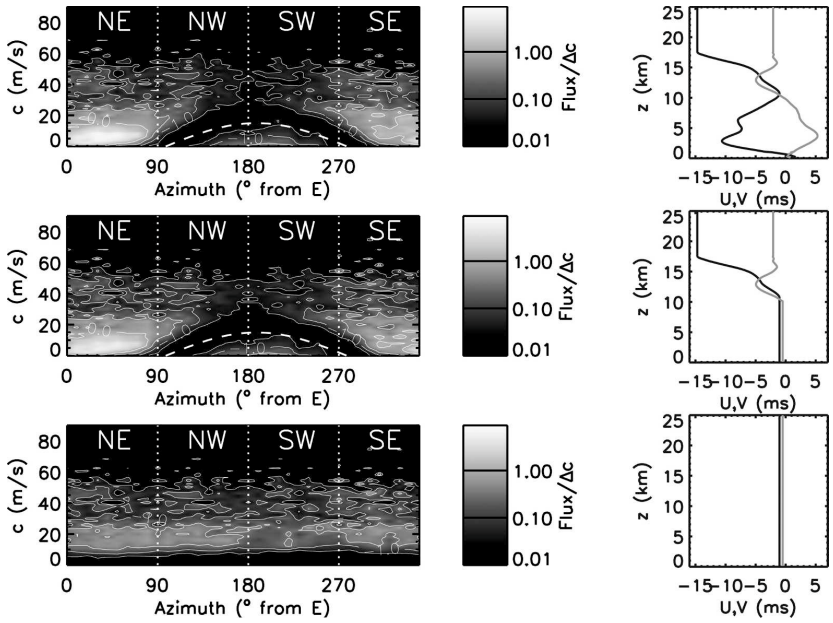

Figure 1.3: Simulations with Piani et al. (2000), Beres et al. (2002) model, of wave forcing with observed spatial and temporal variations in convective latent heating derived from precipitation radar. Momentum fluxes vs ground based phase speed and direction of propagation (left). Corresponding simulated wind profile (right). The wind shear between 10 and 17 km is key to the resulting wave spectrum, whereas wind below 10 km have a minimal effect. The peak in momentum flux at low phase speeds in NE direction is generated by upper tropospheric winds that interact with latent heating sources: it is the "obstacle effect". Figure from Alexander et al. (2006).

mean flow. The wave observation can also give information about their formation process: for instance in the tropical band, Tsuda et al. (1994) used radiosonde measurements of wind velocity and temperature fluctuations that gave access to the wave direction of propagation in the troposphere and stratosphere, giving clues about their convective nature.

1.2.2 Wave impact on dynamics and consequences on cirrus cloud

Wave impact on tropical dynamical cycles and dehydration

Planetary scale waves are fundamentally important to the structure and variability of the TTL. Mixed Rossby-gravity waves were identified with mostly meridional flow fluctuations, while Kelvin waves have been characterized by primarily zonal fluctuations, but the discovery of these waves also brought the question of their potential forcing on a residual circulation in the TTL (Kiladis et al., 2009). At a mesoscale, Kelvin waves are known to interact strongly with the MJO (Madden Julian oscillation) (Dunkerton and Crum, 1995; Straub et al., 2006). They also affect the tropopause height, temperature, cloud top height (Shimizu and Tsuda, 1997) and occurrence (Boehm and Verlinde, 2000; Holton and Gettelman, 2001), as well as the transport, first of water vapour by modulating dehydration (Jensen and Pfister, 2004), and of ozone-rich air from the stratosphere to the troposphere (Fujiwara et al., 1998, 2001). On the other hand Rossby waves are connected to tropical cyclone formation (Frank and Roundy, 2006; Straub and Kiladis, 2003; Zhou and Wang, 2007).

At larger timescale, the Brewer-Dobson annual cycle is forced by tropical and extratropical Rossby waves breaking (Ortland and Alexander, 2014). This circulation is characterised by a seasonal cycle with stronger wave activity during boreal winter.

A first hypothesis from Reed and Vicek (1969); Gage (1981) was that tropical tropospheric circulation is responsible for the annual cycle. Yulaeva et al. (1994) argued that the annual cycle was actually from the stratospheric circulation, with compensation between the tropics and extratropics of seasonal variation of lower stratosphere temperature. The seasonal variation is therefore dynamically driven with periods of stronger overturning related to stronger diabatic heating/cooling in the ascending/descending branch, which in turn requires lower/higher temperatures. The annual cycle is therefore explained by the Brewer-Dobson circulation being strongest in boreal winter and weakest during austral winter (see also Rosenlof (1995)). Later, Randel et al. (2002) showed that the correspondence of stratospheric wave breaking and tropical temperature response also holds on subseasonal time scale. Kerr-Munslow and Norton (2006) showed from ECMWF 15-year reanalysis (ERA-15) the importance of quasi-stationnary waves in the tropics in the tropical momentum flux deposition and Norton (2006) challenges the explanation proposed by Yulaeva et al. (1994) and suggests instead that the seasonally varying strength of tropical Rossby waves that drives the annual cycle of the upwelling and hence temperatures of the Brewer-Dobson circulation. Finally, Randel et al. (2008) concludes from ERA 40 and NCEP/NCAR data that the annual cycle in upwelling is forced by subtropical eddy momentum flux convergence due to waves originating both in the tropics and extratropics.

Other studies have focused on the potential of these waves to drive the QBO (Baldwin et al., 2001). Theoretical work had already established that waves propagating vertically in a wind shear could generate vertical flows of zonal momentum (Booker and Bretherton, 1967). It is the junction of the two that led to the development of the QBO forcing theory by Lindzen and Holton (1968), with Kelvin waves responsible for the eastward acceleration, and mixed Rossby gravity waves the westward acceleration. But these planetary waves are not the only ones responsible for this forcing, one must also take into account the whole spectrum of gravity waves.

A dominant example of the wave-mean flow interaction: the QBO Vertically propagating waves forced in the troposphere can attain large amplitudes in the middle atmosphere as a result of the diminishing background density. They induce a vertical flux of horizontal momentum, which is transferred to the mean flow during processes of wave attenuation as dissipation, saturation, breaking and absorption that occurs in the middle atmosphere. This transfer of momentum flux is the waves' forcing on the mean circulation of the flow or drag effect. It is a key process in driving the middle atmosphere (Holton, 1983). Fritts (1993) found that non orographic waves contribute significantly to the stratosphere momentum budget, and convectively generated gravity waves are known to play an important role in the tropics where deep convection is widespread.
The Quasi-Biennial-Oscillation of the equatorial zonal wind is a planetary scale phenomenon that dominates the lower tropical stratosphere circulation (Baldwin et al., 2001). This oscillation of easterly-westerly regimes has a period of 28-29 months, and consists in the downward motion of zonal wind at a rate of about 1 km per month, that develops at the top of the lower stratosphere (30 km) and dissipates above the tropopause (rapid attenuation from 23 km) (figure 1.4). It is the result of wave-mean flow interaction, with contributions of all upward-propagating tropospheric equatorial waves, from a planetary scale as Kelvin and Rossby waves, to the smaller scales as gravity waves. Their relative contribution is still debated, but the mechanism of their interaction with the mean flow (u) is essentially the same. They interact with the mean flow at the critical layers, defined as surfaces along which the Doppler-shifted phase speed (c) of the wave vanishes ($u - c = 0$). Namely, eastward-propagating waves tend to be damped preferentially in westerly shear zones, and similarly, the westward-propagating waves are damped in easterly shear zones, where their Doppler-shifted frequencies decrease with height. This decrease of the Doppler-shifted frequency is associated with a decrease of the vertical group velocity, until it vanishes at the critical level where u = c. This interaction mean flow/waves results in the dissipation of the wave (absorbed), and the momentum flux convergence associated with this damping provides a deceleration or acceleration (depending on the phase speed of the wave) of the zonal mean flow, and causes the westerly/easterly shear zone to descend since the maximum of this interaction appends right below the critical level.

The oscillating regime between the westward-eastward is further detailed in figure 1.5. It shows in (a) an initial wind profile with respect to altitude. It is a weak westerly wind, together with two waves of phase speed ± c for the eastward/westward propagation. The eastward

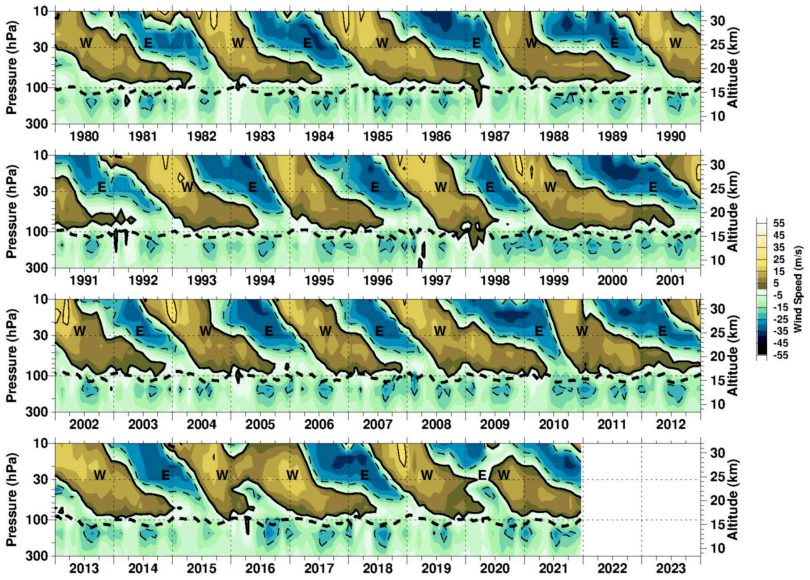

Figure 1.4: The westward and eastward phases of the QBO, with daily sondes data from Singapore. The thick dotted line represents the calculated tropopause from thermal lapse rate (P. A. Newman, NASA/GSFC).

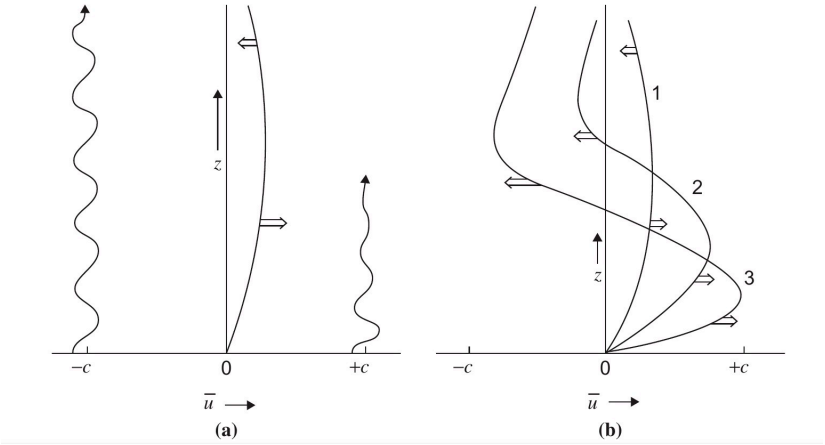

Figure 1.5: Schematic view of wave-driven accelerations of the background wind that lead to the eastward and then westward phases of the QBO, from Plumb (1982).

propagating wave will interact with the wind and be damped at lower levels, and produce a westerly acceleration by momentum transmission as described earlier (b, curve 1). This acceleration will shift downward in time as the westerly wind intensifies (b, 2 and 3). For the westward propagating wave, it is not interacting with the lower part of the wind profile and is able to reach higher altitudes where the wind profile is westward. There, it interacts with the background wind and creates a westward acceleration that also evolves downward (b). The acceleration of the wind profile by the ± c waves are represented with the different horizontal arrows at different times in (b). Around the upper tropopause, the eastward propagating layer of wind is thin enough to be dissipated by viscous diffusion and the stratosphere is then dominated by the easterly regime, so that this time, eastward propagating waves are not interacting with the wind and can penetrate higher altitudes, where they will produce a new westerly acceleration. The mean zonal regime therefore oscillates between westward and eastward phases and the period of this oscillation depends on the properties of the waves.

Impact of waves on cirrus clouds

One of the processes involved in TTL dehydration along with cirrus formation is wave-induced temperature variability (Potter and Holton, 1995; Jensen et al., 1996; Luo, 2003; Schoeberl and Dessler, 2011; Ueyama et al., 2015). The wave forcing on the residual and upwelling circulation modulates the zonal mean temperature. The waves also cause vertical displacements of air masses that induce adiabatic temperature variations. The saturation vapour pressure with respect to ice is related to the temperature. Temperature decrease forces supersaturation and formation of cirrus clouds.

Planetary scale waves We have seen that tropical cirrus clouds can form as residual outflow from deep convection (Massie et al., 2002; Wang and Dessler, 2012) or in situ. This in situ formation can actually be associated with transient temperature perturbations associated with tropical waves that trigger cloud formation (Boehm and Verlinde, 2000; Immler et al., 2008; Fujiwara et al., 2009). Indeed, for convective waves, the induced diabatic circulation on a global scale can extend to the more stratified and stable layers above the convection and directly impact cirrus clouds. Jensen et al. (1996) and Potter and Holton (1995) were the first to emphasize the role of waves in cirrus formation. At planetary scale, tropical cirrus clouds are concentrated in cold anomaly regions. Taylor et al. (2011) highlighted the correspondence between cold anomalies and cirrus clouds in observations, Bramberger et al. (2022) that the temperature anomaly was a very good indicator for cirrus occurrence. Virts et al. (2010) showed that cirrus clouds are formed largely in situ in the planetary-scale ascent regions, in particular that cirrus clouds extend along the Kelvin and Rossby waves. More precisely they pointed out the coincidence of the upwelling and westerly winds, in quadrature with the temperature and cloudiness anomalies, is in agreement with the theoretical structure of Kelvin waves trapped at the equator, described by Holton (1979). Boehm and Verlinde (2000) showed that cirrus clouds are detected during the cold phase of Kelvin waves propagating from the lower stratosphere to the TTL. Similar results were obtained by Immler et al. (2008) who additionally showed the formation and dissipation of cirrus clouds above the warm pool, with

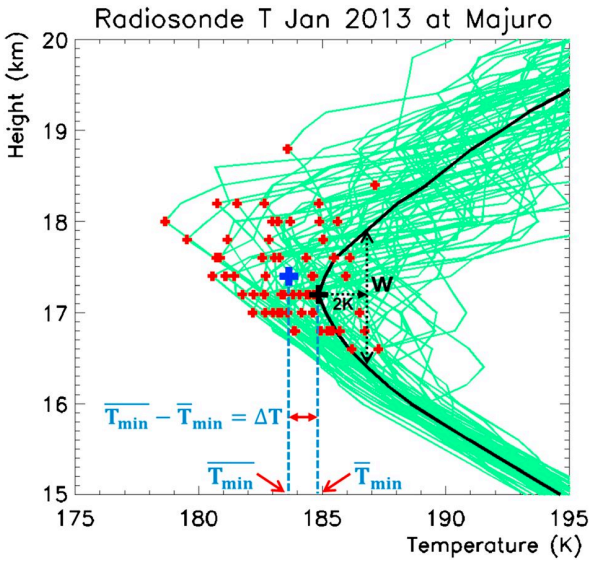

Figure 1.6: From Kim and Alexander (2015), temperature profiles from radiosondes (Majuro, 171°E, 7°N) in January 2013. Green lines are individual profiles, the black thick line is their mean. Red plus signs are the cold point tropopause from each of these individual profiles. The blue plus sign is the average of all the red plus signs. The black plus sign is the coldest point of the mean profile.

Kelvin wave packets having the greatest influence (Fujiwara et al., 2009).

Yet, studies such as (Spang et al., 2002; Massie et al., 2002), who used backward trajectories found that most tropical cirrus clouds originated from cumulonimbus anvils. Thanks to the ATTREX (Airborne Tropical Tropopause Experiment) campaign, Kim et al. (2016) has shown for the first time through direct observations the correspondence between negative wave-induced temperature anomalies and the occurrence of cirrus clouds, and more particularly where the vertical gradients of temperature anomalies are negative. This relationship is prevalent in the highest levels of the TTL over the western Pacific where most tropospheric air enters the stratosphere (Fueglistaler et al., 2004).

Simplified models of water transport using Lagrangian trajectories from the troposphere to the stratosphere (Fueglistaler, 2005) have shown that the water vapour in the stratosphere is controlled by the temperature minimum encountered, potentially from the cold point of the tropopause. The cold point tropopause is located at around 17 400 m and its temperature sets the water vapour mixing ratio of the air parcels entering the stratosphere, by sedimentation of nucleated ice crystals. Among other processes, waves impact this temperature both spatially and temporally. Kim and Alexander (2015) estimated the decrease of the cold point temperatures at Majuro (7°N, 171°E) by comparing the mean cold point and the lowest temperature of the time mean radiosondes profiles and found that waves lower the temperature of 1.6 K on average (figure 1.6, which corresponds to a diminution in entry of water vapour of around 1 ppmv (25% of water vapour entering the stratosphere).

Impact of gravity waves Gravity waves have been known to interact with cirrus clouds. They generate temperature fluctuations that force the formation of ice particles in cold anomalies (Holton et al., 1995; Pfister et al., 2001). Prasad et al. (2019) observed both pre-existing anvil-like cirrus clouds and finer cirrus clouds located away from the convection being modulated by gravity waves excited by deep convection. In both cases, the cirrus responds rapidly to the change in relative humidity (within an estimated 30 min). Numerical simulations of case studies with overshoot observations have confirmed that gravity wave surge is the primary mechanism for the formation of anvil (Homeyer et al., 2017) and thin cirrus (Trier and Sharman, 2016). Gravity waves also impact the wind, which can carry air masses in a different direction than the sedimenting ice crystals, which can impact the life cycle of cirrus clouds and their ability to dehydrate air masses, depending on whether this wind slows or accelerates the vertical motion of ice crystals (Podglajen et al., 2018). The crystals are guided by the waves in areas where $RH_i \approx 100\%$.
High-frequency waves furthermore generate large cooling rates that dominate the properties of newly created clouds (Jensen et al., 2010; Spichtinger and Krämer, 2013; Dinh et al., 2016; Jensen et al., 2016; Podglajen et al., 2016). For instance, Dinh et al. (2016) distinguished two types of nucleation events, limited by available water vapour or by temperature fluctuations. The latter is associated with lower crystal density, which corroborates the conclusion of Spichtinger and Krämer (2013) that high-frequency temperature fluctuations can limit the density of ice crystals obtained by homogeneous freezing.
Finally, studies have used Lagrangian models (Jensen and Pfister, 2004; Ueyama et al., 2015; Schoeberl et al., 2016), and showed that gravity waves can increase the frequency of occurrence of cirrus clouds, especially the higher ones, and change their geographical distribution without affecting sedimentation and dehydration. Simplified microphysical models (Fueglistaler and Baker, 2006) found that at low temperature the time required for efficient dehydration is of the order of 10 h. Thus, the intrinsic higher frequency waves would only have a limited effect on dehydration. But this does not predict the cloud cover.

1.3 Objectives of the thesis

In this context, this thesis aims at better characterizing the activity of gravity waves in the tropics, and to study their impacts on the properties of cirrus clouds and on dehydration of air masses. We mainly address two main questions, using different techniques based on observations and modelling:

1 **Gravity wave activity in the tropics**:
How is the observed activity of gravity waves related to tropical deep convection? At mesoscale, how does the amplitude of the waves vary with distance from the convection and at planetary scale how is the activity of gravity waves related to convective patterns? Finally, what is the contribution of measured gravity waves to the driving of the QBO? This question is also used to better constrain gravity waves parameterizations.

2 **Effect of waves on microphysics**:
Using a microphysical model that takes into account sedimentation, we look at the effect

of temperature variability generated by gravity waves on ice crystal nucleation and growth in the TTL. As the microphysical characteristics are essential to understand the life cycle of cirrus, what is the effect on the populations of crystals, but also on the drying of air masses? To what extent do gravity waves explain observations of ice crystals populations? Finally, what is the sensitivity of ice production to the variability of temperature fluctuations and the gravity waves amplitude?

1.4 Tools

1.4.1 Lagrangian observations from superpressure balloons

Superpressure balloons were developed in 1960s, when Angell and Pack (1960) described the construction of balloons with an internal pressure of 100 hPa and a nearly constant volume. With a balloon volume constrained to be constant, the balloon's density is also constant, and the balloon drifts along an atmospheric level of constant density (isopycnal surface). These first super pressure balloons were called 'tetroons' as they were built with seals in straight lines, forming a tetrahedron shape. In the 1960-70s hundreds of superpressure balloons flights already demonstrated the interest of these devices for scientific purposes: Global Horizontal Sounding Technique (GHOST (1966–70)), Éole (1971–72), Global Atmospheric Research Programme (GARP), Tropical Wind, Energy Conversion, and Reference Level Experiment (TWERLE; 1975). Since then, superpressure balloons have become an accepted and widely used observational tool for gravity waves, but the data were at first limited in frequency and accuracy by a lack of global communication and effective positioning systems.
The Stratéole project started with the Vorcore campaign (2005) that consisted in 27 superpressure balloons that flew for a few months at about 50 and 70 hPa in and around the polar vortex. Stratéole, compared to previous balloons campaign, proposed a benefit from a more modern spaceborne communication and positioning systems to provide a unique and unprecedented high frequency set of observations of the polar stratosphere (Hertzog et al., 2007). With the success of the Vorcore campaign, the Concordiasi project (2010) was later performed with heavier balloons, capable of carrying more instruments and a measurements resolution of 30 seconds (Rabier et al., 2013). The Stratéole-2 balloons, used in our study, are thus built on prior successful long duration balloon campaigns: Stratéole/Vorcore, Concordiasi, and pré-Concordiasi test-flights which initiated tropical long duration balloon flights.

Stratéole-2 campaigns Stratéole-2 is a program of observation of the tropical dynamics, developed in partnership between France (CNRS and CNES) and the United States (LAPS, NWRA, NSF). From 2019 to 2025, three campaigns are planned with about fifty flights in the TTL. Particular characteristics of the tropics make it a region of interest to understand all the climate variability. All balloons are launched from the international airport on Mahé Island (Seychelles) (4S, 55E) (see figures 1.8a and 1.8b for more details). The first campaign took place in boreal winter 2019, and the second one in boreal winter 2021. They launched 8 and 17 flights respectively. The balloons trajectories of the two campaigns are displayed figure 1.7.

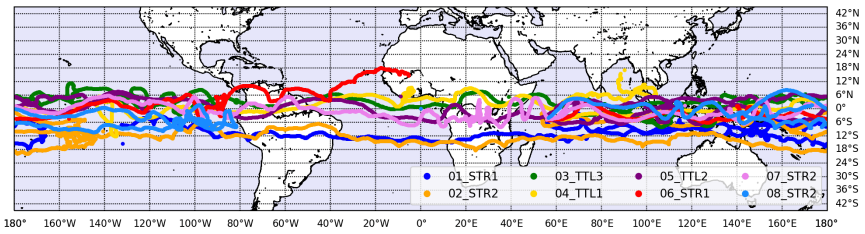

(a) During C0 campaign (2019). Note the oscillations above Africa, followed by 03_TTL3 and 04_TTL1 (yellow and green) corresponding to a planetary scale wave, as well as the one measured by 07_STR2 (pink) eastern of Africa.

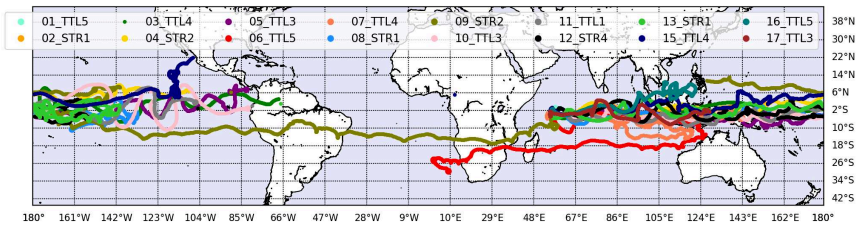

(b) During C1 campaign (2021). Note the oscillations of 10_TTL3 west of Southern America corresponding to a planetary scale wave.

Figure 1.7: Balloons trajectories. All balloons departed eastward, in the same phase of the QBO, two years apart.

Superpressure balloons are closed spherical plastic balloons filled with a given quantity of a light gas such as Helium. They are able to withstand, superpressure i.e $Pg > Pa$ (Pg being the pressure of the gas inside the balloon envelope, Pa of the surrounding environment), and will expand during their ascent until reaching their equilibrium level, at which $\rho_b = \rho_a$. At their equilibrium level, they are spherical, their envelope does not stretch, their volume is stable. Therefore they drift on constant density surfaces in the atmosphere, while air parcels undergo (at first order) adiabatic displacement, and stay on constant potential temperature surfaces (isentropes). So these balloons are quasi Lagrangian tracers, as they follow the air flow horizontally but not vertically.
Two types of balloons were used, either 11 and 13 m of diameter, to fly at respectively $\sim$ 19 and $\sim$ 21 km of altitude at their equilibrium level. The flight duration was limited by the length of qualification tests. Currently, balloons are able to fly for $\sim$ 4 months. The balloons carried sets of instruments listed in the table 1.1, distributed among the different gondolas to address specific questions:

1. **Understanding the dynamics of the atmosphere** and more precisely the role of atmospheric waves responsible for the QBO as well as the processes responsible for the vertical transport of air masses between the troposphere and stratosphere that remains puzzling.

2. **Understanding the transport troposphere-stratosphere and dehydration of air parcels** by analyzing atmospheric compounds. The way greenhouse gases are transported, the characteristics of aerosols and cloud formation are atmospheric processes that can modulate global warming. To obtain profiles of these compounds, instruments

(a) The last step before the launch of the balloon is its inflation. The balloon has previously been laid on the table (1). It is inflated (4) with a fixed amount of gas through its valve (2), that does not fill it completely (see explanation in text). The rest of the balloon is still folded on the table, under the pink layer and a weight (3) separates the inflated part from the rest and prevents the balloon from flying away. Note the red balloon at the top left (5), used to know the local wind at the airport and to approve the launch (the wind must be quite weak near the surface).

(b) Two consecutive photos taken at the release of the balloon: the lower one shows the balloon still on the table (1) and the flight chain still on the ground. The latter is made up of the CNES EUROS gondola (2) in charge of flight safety, then the ZEPHYR gondola (3) which carries the various scientific instruments listed in the table (1.1). The top photo shows the moment when the balloon is released. It will soon carry the whole flight chain to the stratosphere.

Figure 1.8: Pictures of the launch of a balloon at the airport of the Seychelles. As you can see flights were starting at night to avoid planes.

Table 1.1: List of instruments carried on the Stratéole-2 balloons gondolas.

C0	C1	Instrument	Measurement	Precision
all flights	all flights	GPS	Position	1.5 m
all flights	all flights	TSEN	P and T	0.2 K, 0.1 hPa
TTL1	TTL1, TTL5	SAWfPHY	H_2O	5%
TTL1	TTL1, TTL4	B-BOP	Ozone	10 ppbv
TTL1	TTL1	LOAC	Aerosol counter	
TTL2	TTL4	Pico-SDLA	H_2O, CO_2, CH_4	
TTL2	TTL5	FLOATS	high frequency T° profiles down to 2 km under balloon	
STR1	STR1	BOLDAIR	radiometer	
STR1	STR1	ROC	GPS radio-occultation	
STR1	STR1	BeCOOL	Backscatter lidar	
TTL3	TTL3	LPC	Aerosol counter	
TTL3	TTL3	RACHUTS	nighttime cloud/water vapour T profiles down to 2 km below balloon	

are deployed up to 2 km below the balloons. For example, a mini aerosol counter, called LOAC, weighing only 800 g, measures the concentration of fine particles and their characteristics (number, size distribution, nature, typology). The BeCOOL lidar allows to characterize the geometric and optical properties of cirrus clouds.

3. **Operational meteorology, satellite data validation of AEOLUS** by comparison of satellite observations of wind (AEOLUS)/ operational meteorology models to actual Lagrangian measurements.

The overreaching goal is to improve the reliability of current climate models, as the uncertainties in climate predictions are related to our gaps in knowledge of atmospheric processes. Providing observations in the whole tropical band, the project focuses on small scale processes (from the order of the tiny ice crystal for clouds up to ten kilometers for the interactions of clouds with atmospheric dynamics), and Stratéole-2 thus comes here as a complement to the already existing observations by plane, radiosondes or satellites and improve the models regarding medium- and small-scale phenomena, which are mostly parameterized.
We will use in this study the TSEN and GPS instruments, which both have a time resolution of 30 s that enables to resolve the whole spectrum of atmospheric waves (figure 1.9). The BeCOOL lidar will be also used for comparison to cirrus observations.

1.4.2 In-situ airborne observations: ATTREX

The Nasa Airborne Tropical TRopopause Experiment (ATTREX) is a airborne program that focused on TTL processes, and addresses key uncertainties regarding TTL composition, transport, and cloud processes affecting water vapour and short-lived trace gases. Measurements were performed from the Global Hawk unmanned aircraft (see figure 1.10a), which flew at $\approx$ 20 km of altitude on long distances (16 000 km). The payload carried 12 instruments

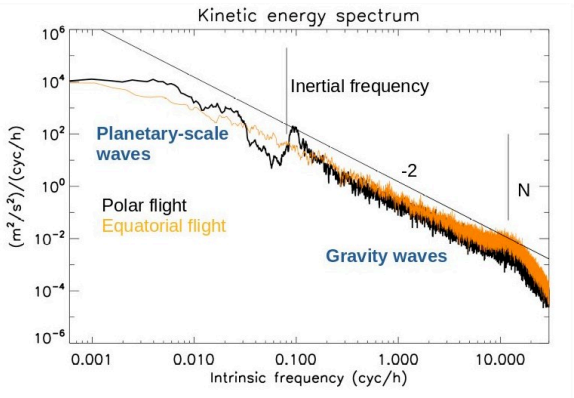

Figure 1.9: Kinetic energy spectrum measured by polar and equatorial flights of stratospheric balloons. Note the difference between spectrum from polar and tropical flights. The latter does not exhibit any peak at the inertial frequency.

to measure cloud properties, water vapour, meteorological conditions, chemical tracers and radicals, as well as radiation. The whole project lasted for 5 years.
We use here only two instruments part of Hawkeye, in charge of ice crystal size distributions and habits:

- **FCDP (Fast Cloud Droplet Probe)** measures forward scattered light from individual cloud particles to determine the particle diameter in the range from 1 μm to 50 μm. It was calibrated with liquid droplets.

- **2DS (Two Dimensions Stereo)** is an optical imaging instrument that uses photodiode arrays using linear array shadowing. It measures the dimensions of individual cloud particles with diameters from 5 μm to 4 mm and gives also ice concentrations.

We focus on 3 flights of the 2014 deployment from Guam in the western Pacific, during boreal winter (January–March). This campaign gathered more than 34 h or cirrus sampling with temperatures between 185 and 207 K (Thornberry et al., 2017) (figure 1.10b). The prevailing meteorological pattern has a pool of cold temperatures located just east of the most active convection (Randel et al., 2006). The cold temperatures prevented the flights to climb more than 17.8 km.
The 12-13 February flight was far away from convection which was most active well west of Guam. The measurements are therefore associated with in in situ formed cirrus clouds. Conversely, the 4 March flight occurred in the vicinity of a typhoon, and is therefore impacted by deep convection. At last, the 6 March flight did not encounter many "fresh" convective systems but took place a few days after a strong MJO that dominated the meteorological conditions at the end of February.

1.5 Outline of the manuscript

The development of the manuscript is articulated in two main chapters:

(a) Image of the Hawkeye unmanned airborne during take off the 20.12.2013 (D. Fratello).

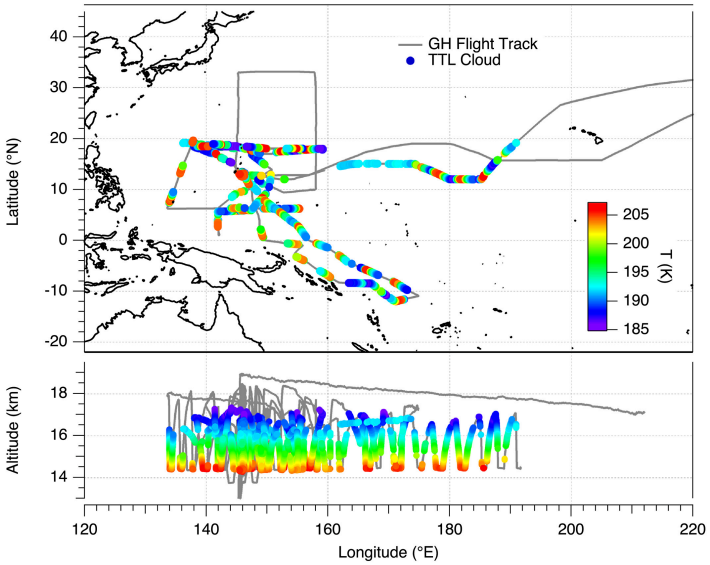

(b) Figure from Thornberry et al. (2017): Map showing the flight tracks (grey) of the Global Hawk during the ATTREX 2014 deployment from Guam. Symbols along the flight track indicate where cirrus clouds were encountered in the TTL, colored by temperature. (bottom) Vertical profiles of the flight tracks showing the altitudes of the encountered clouds.

Figure 1.10: ATTREX campaigns.

Chapter 2 presents observations of momentum fluxes and temperature variance associated with gravity waves from the Stratéole-2 campaign balloons. The wave amplitudes variability and the intermittency are studied and related to the tropical convection.

Chapter 3 focuses on the effect of temperature fluctuations generated by these waves on microphysics and more particularly on ice crystal populations. In a first part, the model we have developed is explained in detail, first following an air parcel simulation during an ascent, then adding a dimension to set the differential sedimentation of ice crystals. This allows us to highlight the importance of this phenomenon to represent the final size of the crystals and the impact of fall streaks.
In a second step, we compare a simulation with and without waves to understand their impact on the density of crystals, their characteristics and effects on air mass dehydration. We test the sensitivity to the variability of these temperature fluctuations.

Chapter 4 tests the effect of the amplitude of the waves, as chapter 2 shows how it varies with the distance to the convection.

Chapter 2

Observation of convectively generated gravity waves at the Tropical Tropopause Layer

Sommaire

This chapter focuses on the observation of tropical gravity waves by Stratéole-2 superpressure balloons.
We use the superpressure balloon observations in order to highlight the prevailing convective nature of gravity waves in the tropical band and investigate the quantitative relation between gravity waves and convection. This chapter introduces the balloons dynamics and derives waves characterisations from the balloon borne observations.

2.1 Calculation of phase speed and momentum flux from balloons observations

Balloon motion equation The horizontal motion of balloons is well tracked by GPS, with a horizontal speed close to the air parcel horizontal velocity ($v_h \approx u_h$ with u_h the horizontal background wind), it is suited to study atmospheric horizontal motion (Vincent and Hertzog, 2014). Conversely, the vertical motion is more difficult to measure and is related to the balloons motion around their buoyancy level and the displacement of this level by the presence of gravity waves. Massman (1978) used numerical integration of the governing equation of motion to explore the response of a superpressure balloon to a gravity wave sinusoidal perturbation. Nastrom (1980) extended these results and developed the equations of spherical objects in a stratified fluid, taking into account simultaneous wave-induced variations of density and vertical wind, such as:

$$(M_b + \eta M_a)\frac{\mathrm{d}w_b}{\mathrm{d}t} = \underbrace{-g(M_b - M_a)}_{\text{buoyancy force}} + \underbrace{(1+\eta)M_a\frac{\mathrm{D}w}{\mathrm{D}t}}_{\text{dynamics term}} - \underbrace{\frac{1}{2}\rho_a C_D A_b (w_b - w)|w_b - w|}_{\text{drag force}} \tag{2.1}$$

with $\frac{\mathrm{D}}{\mathrm{D}t} = \left(\frac{\partial}{\partial t} + u\nabla\right)$ the Lagrangian time derivative, following an air parcel, when $\frac{\mathrm{d}}{\mathrm{d}t} = \left(\frac{\partial}{\partial t} + v_b\nabla\right)$ is the Eulerian derivative in the center of mass of the balloon system. All symbols are defined in the List of symbols, acronyms and abbreviations at the beginning of the manuscript. η is an added mass coefficient which corresponds to the boundary layer of air around the balloon, displaced by its movement. The motion in the vertical direction results from the sum of the buoyancy force that acts as a restoring force whenever the balloon is displaced vertically from its equilibrium position, a dynamic force from the surrounding atmosphere when it is in motion, and finally a drag force, which acts as a resistance to the balloon motion and depends on the difference between the balloon and the background vertical velocities. Other acting forces such as skin friction drag or small-scale turbulence are assumed to be small in comparison and are being neglected here.
In an atmosphere at rest, when $w = 0$, the equilibrium level ($\frac{\mathrm{d}w_b}{\mathrm{d}t} = 0$) of the balloon is given by $M_b = M_a$. Thus, $M_b = \rho V_b$ with the volume of the balloon V_b as $M_b = \rho_b V_b$. It implies $\rho_b = \rho$: the density of the balloon at its equilibrium level is the same as the density of the air parcel. The balloon rests vertically on an Equilibrium Density Surface (EDS) or isopycnic surface, the altitude of which varies in time and space: $\zeta_\rho(\rho_b, x, y, t)$. On the other hand, at first order air parcels follow isentropes.

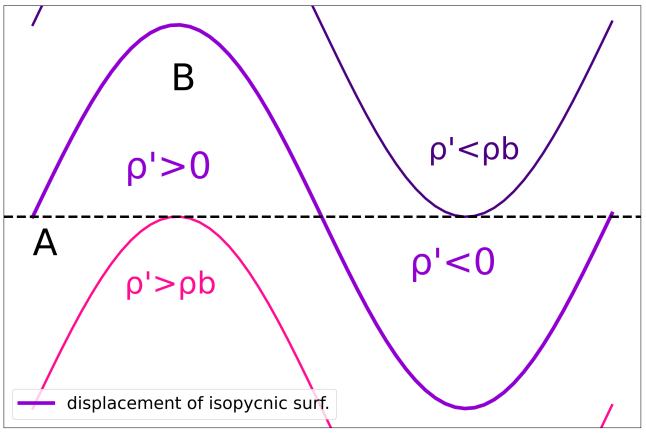

Figure 2.1: (purple) Vertical displacements of an isopycnic surface of the same density of the balloon (ρ_b) generated by an Eulerian disturbance in air density ρ induced by a gravity wave.

Theory of balloon as a perfect isopycnic tracer Figure 2.1 represents the vertical displacements of an isopycnic surface generated by an Eulerian disturbance in air density induced by a gravity wave (purple line).
On the figure, the density at A is not affected by the wave-induced disturbance, $\rho' = 0$, whereas density at B becomes:

$$\rho(z_0 + \zeta'_\rho) = \bar{\rho}(z_0 + \zeta'_\rho) + \rho'(z_0 + \zeta'_\rho) \tag{2.2}$$

Since A and B are on the same isopynic surface:

$$\begin{aligned} \bar{\rho}(z_0) &= \bar{\rho}(z_0) + \frac{\partial \bar{\rho}}{\partial z}\zeta'_\rho + \rho'(z_0) \\ \zeta'_\rho &= \frac{-\rho'(z_0)}{\partial \bar{\rho}/\partial z} = H\frac{\rho'(z_0)}{\bar{\rho}(z_0)} \text{ (at first order)} \end{aligned}$$

with H the density scale height as $H^{-1} = -\frac{1}{\bar{\rho}}\frac{\partial \bar{\rho}}{\partial z}$, with a typical value of 6 km in the stratosphere.
In addition, the wave-induced pressure perturbation at B is expressed by a Lagrangian disturbance term added to the mean background pressure:

$$p(z_0 + \zeta'_\rho) = \bar{p}(z_0) + \underbrace{\zeta'_\rho \frac{\partial \bar{p}}{\partial z} + p'(z_0)}_{\text{Lagrangian disturbance } p'_L} \tag{2.3}$$

The Lagrangian perturbation p'_L, which is directly recorded by the balloon, is the sum of the Eulerian perturbation caused by the wave noted p'_e, and a contribution associated with motion of the balloon in the background vertical pressure gradient noted p'_g. In the hydrostatic limit:

$$p'_g = -\bar{\rho} g \zeta'_\rho \tag{2.4}$$

Similarly, the same equation can be derived for the horizontal wind:

$$u(z_0 + \zeta'_\rho) = \bar{u}(z_0) + u'_e(z_0) + \zeta'_\rho \frac{\mathrm{d}\bar{u}}{\mathrm{d}z} \tag{2.5}$$

where the Lagrangian contribution is negligible compared to the Eulerian one (u'_e). Indeed, typically, $u'_e \sim 1$ m/s, $\frac{\mathrm{d}\bar{u}}{\mathrm{d}z} \sim 0.01\ s^{-1}$ therefore $\zeta'_\rho \ll 100$ m, which is true for gravity waves. The balloon follows the air flow horizontally.

The complex wave-driven perturbations noted respectively $(u'_{||}, w', p', \rho')$ are linked together via the polarization relations. Fritts and Alexander (2003) describes the relation between the Eulerian pressure disturbance p'_e and the perturbation of velocity in the direction of propagation of the wave $u'_{||}$ in the horizontal momentum equation:

$$p'_e = \bar{\rho}\hat{c}\left(1 - \frac{f^2}{\hat{\omega}^2}\right) u'_{||}\,, \tag{2.6}$$

with f the inertial frequency, and $\hat{\omega}$ the wave intrinsic frequency. $\hat{c}$ denotes the horizontal intrinsic phase speed i.e the phase speed in the referential of the air mass. It can be different from the ground based phase speed, measured by remote sensing or ground based instruments. On the other hand, from the vertical momentum equation, we can link the perturbation of density ρ' to p'_e:

$$-i\hat{\omega}w' + \left(im - \frac{1}{2H}\right)\frac{p'_e}{\bar{\rho}} = -g\frac{\rho'}{\bar{\rho}} \tag{2.7}$$

In the above, the first term may be ignored when dealing with hydrostatic waves. m is the vertical wave number, w' the vertical velocity perturbation.

From (2.4) and (2.7) the Lagrangian perturbation measured by the balloons can be related to the wave driven pressure perturbation as:

$$p'_L = p'_g + p'_e = p'_e\left(1 + \left(imH - \frac{1}{2}\right)\frac{N^2}{N^2 - \hat{\omega}^2}\right) \tag{2.8}$$

In the limit of hydrostatic waves, $\hat{\omega}^2 \ll N^2$:

$$p'_L = p'_g + p'_e = \left(\frac{1}{2} + imH\right) p'_e \tag{2.9}$$

As p'_e is described as dependent on the intrinsic phase speed by (2.6), it yields in the general case:

$$p'_L = \left(\frac{1}{2} + imH\frac{1}{1 - \frac{\hat{\omega}^2}{N^2}}\right)\bar{\rho}\hat{c}\left(1 - \frac{f^2}{\hat{\omega}^2}\right) u'_{||} \tag{2.10}$$

For gravity waves in the hydrostatic hypothesis, with a typical vertical wavelength of 3 km so a vertical wavenumber $m \approx 2.10^{-3}$ rad/m, the imaginary part dominates the real part of (2.10). The Lagrangian perturbation of pressure p'_L and the horizontal wind perturbation $u'_{||}$ in the wave propagation direction are therefore primarily in phase quadrature, when the Eulerian perturbation p'_e and $u'_{||}$ are in phase (2.6).

From the covariance between p'_L and $u'_{||}$ the horizontal intrinsic phase speed can be expressed as:

$$\hat{c} = \frac{\mathfrak{Re}(p'_L u^*_{||})}{\bar{\rho}u'^2_{||}} \frac{1 - \frac{\hat{\omega}^2}{N^2}}{1 - \frac{f^2}{\hat{\omega}^2}} \frac{1}{\frac{1}{2} - \frac{\hat{\omega}^2}{N^2}} \tag{2.11}$$

and in the hydrostatic hypothesis:

$$\hat{c} = \frac{2}{\bar{\rho}\left(1 - (\frac{f^2}{\hat{\omega}^2})\right)} \frac{\mathfrak{Re}(p'_L u^*_{||})}{u'^2_{||}} \tag{2.12}$$

with $u'^*_{||}$ the complex conjugate of $u'_{||}$. Note the limitation for $\hat{\omega}^2 = N^2/2$. Similarly, from 2.10 the polarization relation between vertical velocity perturbation w' and $u'_{||}$ is used to obtain the wave absolute momentum fluxes:

$$\begin{aligned} w' =& \frac{-\left(m + \frac{i}{2H}\right)\hat{\omega}}{N^2 - \hat{\omega}^2} p'_e \\ p'_e =& \frac{\hat{\omega}^2 - f^2}{\hat{\omega} k_h} u'_{||} \end{aligned} \tag{2.13}$$

with k_h the horizontal wavenumber.

$$\mathfrak{Re}(u'^*_{||} w') = -\frac{\hat{\omega}}{\bar{\rho} H N^2} \mathfrak{Im}(p'_L u'^*_{||}) \tag{2.14}$$

We retain here only the real part of the momentum flux as it is the only contribution that does not fade when averaged over a wave period. Note that the expression of the momentum fluxes doesn't change in the hydrostatic approximation. N is the Brunt-Väisälä or buoyancy frequency, only depending on the background gradient of temperature:

$$\frac{1}{\bar{\rho} H N^2} = \frac{1}{\bar{\rho} g} \frac{g/R + \mathrm{d}\bar{T}/\mathrm{d}z}{g/c_p + \mathrm{d}\bar{T}/\mathrm{d}z} \tag{2.15}$$

We have assumed here that the balloons are perfect isopycnic tracers, and thus follow the purple curve. It is making the assumption that $\zeta'_b/\zeta'_\rho(\rho_b) << 1$. Nastrom (1980) showed that the vertical displacement of a balloon can slightly depart from that of a perfect isopycnic tracer. This assumption leads to errors for frequencies $\hat{\omega} \sim N$.

From isopycnic surfaces to isentropes The vertical motion of the balloon results from its small oscillation around its EDS (the neutral buoyancy oscillation) at a frequency ω_b of typically 3 to 4 min, a drag forcing from the vertical wind w and the altitude of the isopycnic surface ζ_ρ (figure 2.2).

For a small perturbation, this can be written:

$$\rho' + \zeta'_\rho \frac{\mathrm{d}\bar{\rho}}{\mathrm{d}z} \approx 0 \tag{2.16}$$

with ρ' the density fluctuation at a fixed Eulerian location and ζ'_ρ the isopycnic surface displacement. Similarly, the isentrope ζ_θ can be related to a potential temperature anomaly θ' in a vertically stratified fluid:

$$\theta' + \zeta_\theta \frac{\partial \bar{\theta}}{\partial z} = 0 \tag{2.17}$$

The same way as (2.17), in a non compressible fluid $\frac{\theta'}{\bar{\theta}} = \frac{T'}{\bar{T}} = -\frac{\rho'}{\bar{\rho}}$. It comes:

$$-\frac{\zeta_\theta}{\bar{\theta}} \frac{\mathrm{d}\bar{\theta}}{\mathrm{d}z} = \frac{\zeta_\rho}{\bar{\rho}} \frac{\mathrm{d}\bar{\rho}}{\mathrm{d}z} \tag{2.18}$$

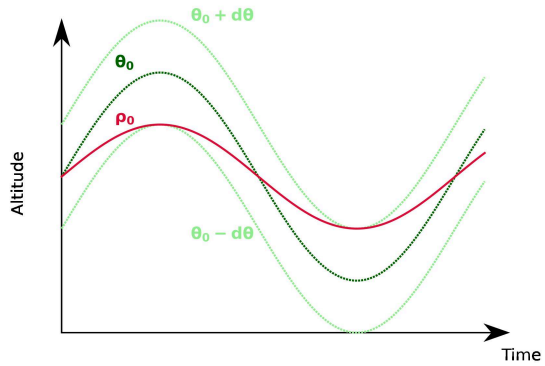

Figure 2.2: (green) Vertical displacements of an isentrope surface generated by an Eulerian disturbance. (red) The corresponding isopycnal vertical displacement followed by the balloons.

With $\bar{\theta} = \bar{T}\left(\frac{P}{P_0}\right)^{\frac{-R}{c_p}}$, P_0 the reference level of pressure. Using the approximation of perfect gas and hydrostatic equilibrium:

$$\frac{1}{\bar{\theta}}\frac{\mathrm{d}\bar{\theta}}{\mathrm{d}z} = \frac{1}{\bar{T}}\left(\frac{\mathrm{d}\bar{T}}{\mathrm{d}z} + \frac{g}{c_p}\right) \tag{2.19}$$

From (2.19) and using the similar method of (2.18) but for the perfect gas law, it yields that the altitude of the isopycnic surface can be linked to the altitude of the isentrope as:

$$\zeta_\rho = -\frac{\frac{1}{\bar{\theta}}\frac{\partial\bar{\theta}}{\partial z}}{\frac{1}{\bar{\rho}}\frac{\partial\bar{\rho}}{\partial z}}\zeta_\theta = \frac{\frac{g}{cp} + \frac{\partial\bar{T}}{\partial z}}{\frac{g}{Ra} + \frac{\partial\bar{T}}{\partial z}}\zeta_\theta = \alpha\zeta_\theta \tag{2.20}$$

α is typically of 0.33 in the lower stratosphere. Thus, at a first order, the air parcels displacements (isentropes surfaces) and the balloons displacements (isopycnic surfaces) are in phase, but the balloons displacements are of smaller amplitudes than the ones of air parcels. The balloons vertical motions are forced by the isentrope vertical displacements.

2.2 Balloon motion and gravity wave activity observation

2.2.1 A simple parameter to assess the impact of convection on balloon motions

A first, very schematic, approach to assess the relationship between the recorded gravity-wave activity and the surrounding convection, is to link the disturbances of the balloons vertical motion to the surrounding convective activity. Indeed, as described in the previous section, the vertical motion of the balloon is linked to that of the air parcels. It is therefore impacted by Eulerian disturbances such as the ones generated by gravity waves. In the deep tropics, moist convection is supposed to be the most prominent source of gravity waves. The convective activity has a geographical pattern, with stronger convection and more overshooting systems over the continents (Alcala and Dessler, 2002; Liu and Zipser, 2005). Deep convection also follows a diurnal cycle (Nesbitt and Zipser, 2003). In this first attempt, we have used the standard deviation of the temperature fluctuations T' with periods between 15min and ∼1 day, therefore supposedly generated by the gravity waves (figure 2.4). We didn't use the direct

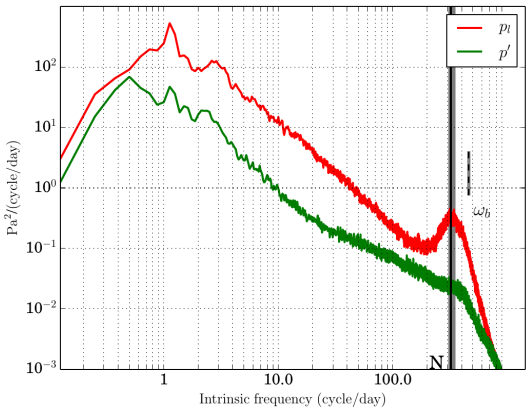

Figure 2.3: Power spectra of the Eulerian pressure perturbation (green) and contribution from the balloon vertical displacement in the background of pressure (red).

measurement of temperature which actually results from number of processes, such as radiative exchange with solar radiation and the surrounding atmosphere, heat conduction through the thermistor wires, Joule effect. The sole one that brings the thermistor temperature back to that of the air is the heat conduction/convection to ambient air which is less efficient when balloons move with the winds. Thus the recorded temperature may deviate from the one of the air (Hertzog et al., 2004) and we reconstructed temperature from pressure measurements instead.

The pressure measurements are linked to the balloons vertical displacement as expressed by (2.8). The Eulerian perturbation of pressure is considered negligible compared to the term linked to the balloons vertical displacement in the background gradient of pressure, as demonstrated by figure 2.3. The previous section described the transformation of an isopycnic vertical displacement into a fluctuation following isentrope surfaces (2.20). An adiabatic transformation $T' = -\frac{g}{c_p}\zeta'_\theta$ is then applied to get the temperature disturbance of the air parcel.

This transformation between the vertical motion of the balloon and the temperature perturbation will be used in section 2.3 and chapter 3 for the impact on ice crystals. We introduce it here as a simple metric to measure the impact of dynamics variability on the measurements. In figure 2.4 the upper panel (a) displays the global daily evolution of the standard deviation recorded by all the balloons, over the continent or the ocean. Even though a time dependence is not obviously noticeable, it clearly shows a difference between the continents and oceans. This observation of a more substantial geographical pattern than a temporal one led to the second part of our paper (see section 2.3) which aims at studying the global distribution of the wave's magnitude and to compare it with convective activity. The lower panels (b) show the daily evolution of the 5^{th} and 95^{th} quantiles of the T' standard deviation over an hour. The weakest values (dashed curve) are preferentially measured at night, and reversely in the afternoon for the highest. This temporal pattern is more clear over the continents. Overall, the signal from a time pattern does not clearly stand out, as the temperature variance is more influenced by lower frequency waves. The observed standard deviation fluctuations come from

longer time scale perturbations, and this parameter is therefore limited in order to study the whole gravity waves spectrum. In the following, we will rather use the momentum fluxes, useful for the gravity waves parameterizations.

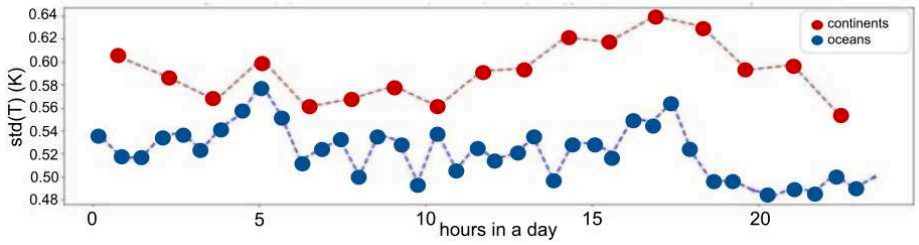

(a) Average of the standard deviation of temperature on intervals of 100 (continents in red) and 200 (oceans in blue) points according to the time of day.

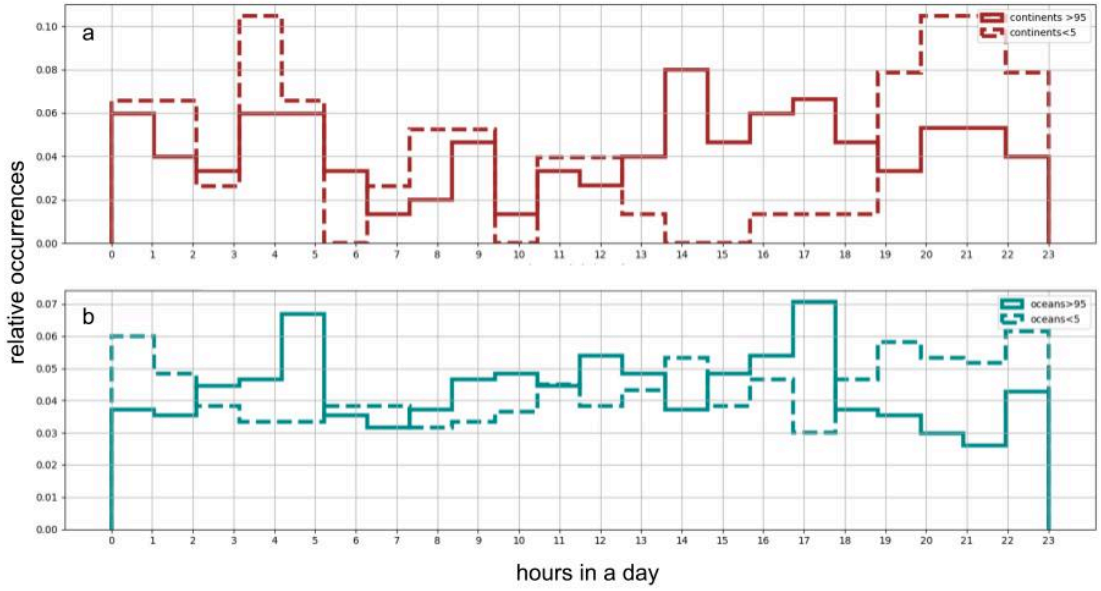

(b) Histogram of the 5 % highest (line) and 5% lowest (dashed) standard deviation of the temperature fluctuations over 1 hour, over continents (a) and oceans (b).

Figure 2.4: The spatial and temporal variation of the recorded standard deviation of temperature fluctuations.

2.2.2 From measurements to momentum flux and phase speed time series

Following the method of Vincent and Hertzog (2014) and Boccara et al. (2008) described in section 2.1, time series of the measured pressure, horizontal velocity, temperature and density are decomposed upon wavelets analysis (Torrence and Compo, 1998). Wavelet analysis like S transforms are common tools to analyze and locate variations of power in a time serie. Their principle is to decompose the time serie in the time-frequency space, enabling the determination of the dominant modes of variability and their time evolution (figure 2.5). We have used a complex Morlet mother wavelet with periods ranging between 1 to 24 h, enabling

us to retrieve the energy and phase of the signal decomposed in small bins of time/intrinsic frequency. The resulting momentum flux and phase speeds are positive as they represent the wave direction of propagation. Figure 2.5 displays the decomposition of momentum flux in the time-frequency space for one flight of the first campaign. It shows the different planetary scale wave packets in the upper panel. The lower panels displays the sporadic gravity wave packets, as well as the signal from the balloons neutral oscillations at the smallest periods.

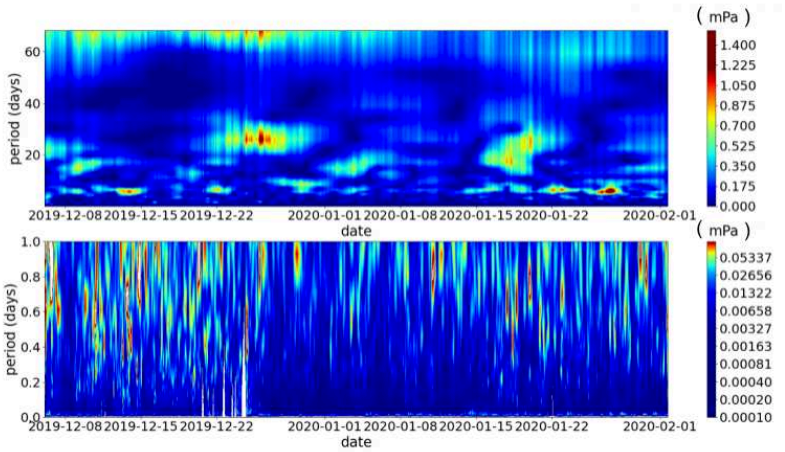

Figure 2.5: Decomposition of momentum flux of C0_06_STR1 flight for the whole spectrum (upper panel) and gravity waves spectrum (lower panel).

The coefficients corresponding to the different wave packets can be summed over the range of wanted periods. Here, we have chosen to select gravity waves with periods between 15 min and a day to cut off the effect of the neutral oscillations of the balloons and the planetary scale waves. Our assumption is that at these periods, the main dynamical processes impacting the measurements are gravity waves.

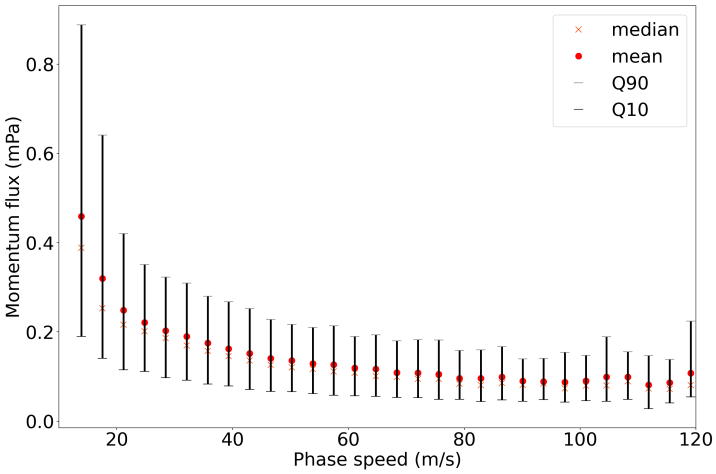

Figure 2.6: Normalized boxplots of momentum fluxes in bins of phase speed with periods between 15 min and a day, for all the C0 flights.

Figure 2.6 shows the increase of momentum fluxes for $\hat{c} \to 0$. The mechanisms responsible

for the generation of the waves impose smaller phase-speeds. Thus, the distribution tending to a stable value of momentum fluxes around 5 mPa (table 2 of publication), is related to the limitation of the phase speed computation for now. It thus won't be used in the observation of gravity waves. A better calculation would be useful to investigate the source mechanism of the observed gravity waves more precisely.
The following article summarizes the results for the first campaign of Stratéole-2. It highlights the prominent convective nature of observed gravity waves at the tropics by evidences at a convective and planetary scale.

2.3 Article: Observation of Gravity Waves at the Tropical Tropopause Layer using Superpressure Balloons

AGU ADVANCING EARTH AND SPACE SCIENCE

JGR Atmospheres

RESEARCH ARTICLE
10.1029/2021JD035165

Observation of Gravity Waves at the Tropical Tropopause Using Superpressure Balloons

Milena Corcos[1], Albert Hertzog[1], Riwal Plougonven[2], and Aurélien Podglajen[3]

[1]Laboratoire de Météorologie Dynamique/IPSL, Sorbonne Université, Paris, France, [2]Laboratoire de Météorologie Dynamique/IPSL, Ecole Polytechnique, Institut Polytechnique de Paris, Palaiseau, France, [3]Laboratoire de Météorologie Dynamique/IPSL, CNRS, Ecole Polytechnique, Institut Polytechnique de Paris, Palaiseau, France

Key Points:

- Tropical gravity wave activity is characterized from long-duration superpressure balloon flights
- Gravity-wave momentum fluxes exhibit a clear dependence to the distance to the nearest convective system
- Observed wave intermittency results from the time- and spatially-varying distribution of the source

Correspondence to:

M. Corcos,
milena.corcos@lmd.ipsl.fr

Citation:

Corcos, M., Hertzog, A., Plougonven, R., & Podglajen, A. (2021). Observation of gravity waves at the tropical tropopause using superpressure balloons. *Journal of Geophysical Research: Atmospheres*, *126*, e2021JD035165. https://doi.org/10.1029/2021JD035165

Received 29 APR 2021
Accepted 9 JUL 2021

Author Contributions:

Formal analysis: Milena Corcos, Albert Hertzog, Riwal Plougonven, Aurélien Podglajen
Methodology: Milena Corcos, Albert Hertzog, Riwal Plougonven, Aurélien Podglajen
Writing – original draft: Milena Corcos
Writing – review & editing: Albert Hertzog, Riwal Plougonven, Aurélien Podglajen

Abstract Tropical gravity wave activity is investigated using measurements of momentum fluxes gathered during Strateole-2 superpressure balloon flights. The data set consists of eight balloon flights performed in the deep tropics from November 2019 to February 2020. The flights lasted for 2–3 months each, and in-situ meteorological data were collected every 30 s. The relation between gravity waves and deep convection is investigated using geostationary satellite data from the NOAA/NCEP GPM_MERGIR satellite data product, at 1 h resolution. The amplitude of gravity wave momentum fluxes shows a clear dependence on the distance to the nearest convective system, with a strong decay as distance to convection increases. The largest momentum-flux values (>5mPa) are only found less than 200 km away from deep convection. The sensitivity of the wave flux to distance from convection is stronger for high frequency gravity waves (periods shorter than 60 min). Lower frequency waves tend to a non-zero, background value away from convection, supporting some background value in gravity-wave drag parameterizations. On the other hand, the wide range of momentum flux values observed close to the convection emphasizes the intermittent nature of the gravity-wave source. The large scale variation of gravity-wave intermittency within the equatorial belt is also studied. The results highlight spatial variations of gravity wave activity, with the highest momentum flux recorded over land.

1. Introduction

Tropical deep convection excites a broad range of waves. At the low-frequency end, planetary-scale equatorial waves, like Kelvin or Yanai waves, have periods of a few to tens of days and horizontal scales that are a fraction of the Earth circumference (Matsuno, 1966). At the high-frequency end, gravity waves have periods as low as a few minutes and horizontal scales as short as that of individual convective cells. Yet, despite their short temporal and spatial scales, gravity waves significantly impact the global tropical atmosphere. They can influence synoptic systems (Lane & Moncrieff, 2008; Piani et al., 2000), and are an essential driver of the Quasi-Biennial Oscillation (QBO) together with (or even more importantly than) planetary waves (Dunkerton & Dunkerton, 1997; Ern et al., 2008, 2014; Kawatani et al., 2010). At smaller scales, gravity waves initiate cirrus clouds and modulate their life cycle (Dinh et al., 2016; Jensen et al., 2016; Podglajen et al., 2016, 2018), which both impact the local dynamics and the global climate (Fueglistaler & Baker, 2006; Jensen et al., 2010; Solomon et al., 2010). Last, all tropical waves contribute to modulating the tropopause temperature, and thus influence water vapor transport to the stratosphere (Kim & Alexander, 2015).

Whereas the resolution of atmospheric general circulation models enables the explicit resolution of large-scale waves in most circumstances, it remains too coarse to fully resolve shorter-scale gravity waves. These are notably parameterized in climate models in order to represent their significant contribution in shaping the mean circulation of the middle atmosphere (Fritts, 1993; Fritts & Alexander, 2003; Holton et al., 1995). In particular, the QBO, which is a major feature of the Earth climate (Baldwin et al., 2001), is partly driven by gravity waves, and its simulation in climate models remains particularly challenging (Butchart et al., 2018; Holt et al., 2020; Schirber et al., 2015). The evolution of the QBO under climate change is furthermore currently unclear (Richter et al., 2020), calling for enhanced observational constraints on tropical gravity waves to improve parameterizations.

In the deep tropics, moist convection is the most prominent source of gravity waves: satellite observations have for instance shown the coincidence in location and seasonality of stratospheric gravity waves and

Journal of Geophysical Research: Atmospheres 10.1029/2021JD035165

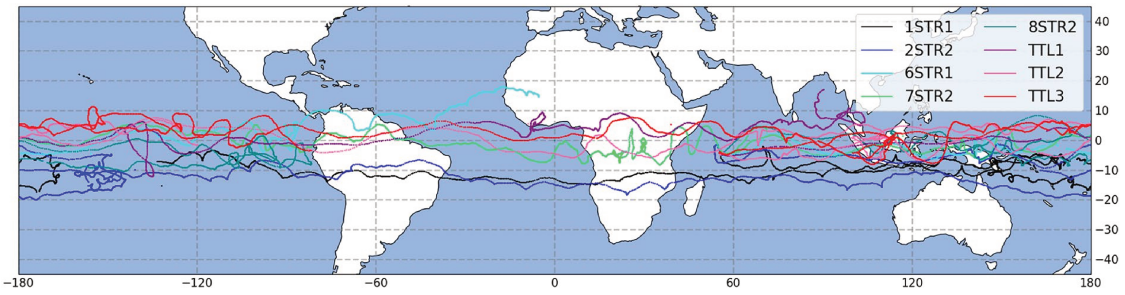

Figure 1. Map of the eight superpressure balloon flights of the first Strateole-2 campaign, which were launched in November-December 2019.

deep tropospheric convection (Alexander et al., 2008; Ern et al., 2011). Mechanisms involved in convective gravity-wave generation have been revealed thanks to idealized simulations of numerical models (Alexander et al., 1995; Lane et al., 2001; Piani et al., 2000). Convective gravity waves have also been observed with further techniques like radar (Larsen et al., 1982), aircrafts (Alexander & Pfister, 1995; Jensen et al., 2013; Pfister et al., 1993), and radiosoundings (Karoly et al., 1996; Dhaka et al., 2011). Yet, because of their short spatial scales and of their intermittency, global observations of gravity waves remain challenging (Alexander et al., 2010). To better constrain gravity-wave parameterizations in global models therefore requires more observations. In the present study, we use observations gathered during long-duration stratospheric balloon flights within the Strateole-2 project (Haase et al., 2018). Strateole-2 will release a total of 50 long-duration balloons in three campaigns between 2019 and 2024. These balloons are intended to drift around the whole tropical belt to enable studies of climate processes in the Tropical Tropopause Layer (TTL) and the lower stratosphere. Since they can fly for months, continuous observations at high-resolution performed during the flights provide unique measurements of the global activity of gravity waves (Boccara et al., 2008; Hertzog et al., 2008; Hertzog & Vial, 2001; Jewtoukoff et al., 2013; Vincent et al., 2007), with a potential to provide valuable insights on their contribution to the QBO (Vincent & Alexander, 2020).

This study is thus aimed at characterizing equatorial gravity-wave activity during boreal winter, and at describing its relation to deep convection. After describing the data set used and our methodology in Section 2, we present in Section 3 a case study of a large gravity-wave momentum-flux event, associated with a convective complex in the intertropical convergence zone (ITCZ). In Section 4, we statistically study the dependence between recorded momentum fluxes and the balloon distance to convective cells. The discussion section then addresses the observed differences in the behavior of short- and long-period gravity waves, as well as geographical contrasts in wave activity and intermittency in the tropics. The last section of the article is devoted to a brief summary and conclusion.

2. Data and Methodology

2.1. Balloon Observations

Gravity-wave information used in this study is derived from observations collected by superpressure balloons in the deep tropics. These flights were performed during boreal winter (November 2019–February 2020), within the first Strateole-2 campaign. The trajectory of the 8 balloons released from Seychelles Islands (55.52°E, 4.67°S) during this campaign are displayed in Figure 1. To a good approximation, superpressure balloons drift on constant-density surfaces in the atmosphere (Hertzog & Vial, 2001), and thus behave as quasi-Lagrangian tracers in the flow. During the campaign, two different flight levels were used. Low-level "TTL" flights flew at ∼19 km, typically 1.5 km above the Cold-Point Tropopause (CPT), near the top of the TTL. Higher-level "STR" flights on the other hand flew at ∼20.5 km, in the stratosphere. The mean altitude and pressure of each of the flights are reported in Table 1. All observations were collected within 20° of the equator.

Every balloon carried a GPS receiver and a Tsen instrument (Thermodynamical sensor), which records the in-situ air pressure and temperature (Hertzog et al., 2004, 2007). Both the GPS receiver and the Tsen provide observations every 30 s during the flights. In theory, this time resolution enables us to resolve the

Journal of Geophysical Research: Atmospheres 10.1029/2021JD035165

Table 1
Characteristics of 2019 Strateole-2 Balloon Flights

Flight	Altitude (km)	Pressure (hPa)	Launch (UT)	End (UT)	Duration (day)
01_STR1	20.7	50.8	2019-11-12	2020-02-28	107
02_STR2	20.2	55.0	2019-11-11	2020-02-23	103
03_TTL3	19.0	66.2	2019-11-18	2020-02-28	101
04_TTL1	18.8	69.4	2019-11-27	2020-02-02	66
05_TTL2	18.9	67.6	2019-12-05	2020-02-23	79
06_STR1	20.5	51.4	2019-12-06	2020-02-01	57
07_STR2	20.2	54.8	2019-12-06	2020-02-28	83
08_STR2	20.2	54.6	2019-12-07	2020-02-22	77

full spectrum of atmospheric waves in the tropical lower stratosphere. As usually performed with superpressure balloon observations, the zonal and meridional components of the wind are deduced from successive positions of the balloon, with a precision of ∼0.1 m/s (Podglajen et al., 2014; Vial et al., 2001). The air-parcel vertical displacements (ζ'), on the other hand, are inferred from the pressure time series: the pressure measurements are preferred over the raw GPS records, since they have a higher precision (0.1 hPa, typically corresponding to 0.1 m at the balloon flight level) than the GPS altitudes (precision of ∼1.5 m). Actually, the wave-induced total pressure disturbances (p'_T) measured by superpressure balloons read:

$$p'_T = p' + \frac{d\overline{p}}{dz}\zeta'_b \tag{1}$$

where the first term in the RHS corresponds to the Eulerian pressure perturbations (p'), and the second term is a Lagrangian contribution associated with the vertical displacement of the balloon (ζ'_b) in the background pressure gradient ($\frac{d\overline{p}}{dz}$). For wave motions with intrinsic periods longer than $2\tau_N$, where $\tau_N = 2\pi / N \sim 4.5$ min is the Brunt-Väisälä period in the tropical lower stratosphere, superpressure balloons stay on constant-density surfaces (Vincent & Hertzog, 2014). Their vertical displacements are then readily related to those of air parcels:

$$\zeta' = \frac{g / c_p + d\overline{T} / dz}{g / R + d\overline{T} / dz}\zeta'_b \tag{2}$$

where g is the gravitational acceleration, c_p and R are the heat capacity at constant pressure and the perfect gas constant per unit mass respectively, and $d\overline{T} / dz$ the background vertical gradient of temperature.

The balloon timeseries are processed through a wavelet analysis, as was done in Hertzog and Vial (2001), Boccara et al. (2008) and Hertzog et al. (2012). The wavelet analysis provides information in the time/intrinsic-frequency domain for each of the timeseries. We use a complex Morlet mother wavelet, which enables us to retrieve the local amplitude and phase of the signals every 30 s on a finite number of intrinsic frequencies ($\hat{\omega}_i$) (Torrence & Compo, 1998). Gravity-wave momentum fluxes are inferred from the cross-correlation of total-pressure and horizontal-wind disturbances. Here, we take benefit from the fact that the two terms in the RHS of Equation 1 are in phase quadrature, so that only the cross-correlation with the second term (that is linked to the air-parcel vertical displacements) is retained (see, e.g., Equation 26 in Vincent and Hertzog (2014)). The wavelet coefficients are then combined and summed over the intrinsic frequency axis to obtain timeseries of for example, zonal momentum fluxes $\overline{\rho u' w'}(t)$, where $\overline{\rho}$ is the flight-averaged balloon density. The gravity-wave polarization relations are used to infer the local wave direction of propagation (Fritts & Alexander, 2003), and thus the total momentum-flux timeseries $\overline{\rho u'_{\parallel} w'}(t)$, which is the sum of the absolute momentum fluxes over all propagation directions.

Note that temperature fluctuations (T') used in this study were also reconstructed from the air-parcel vertical displacements according to the adiabatic equation:

$$T' = -\frac{g}{c_p}\zeta', \tag{3}$$

which typically holds for periods shorter than a few days in the tropical lower stratosphere. Temperature disturbances obtained this way are generally less noisy than the raw temperature measurements: since superpressure balloons move with the wind, the ventilation of temperature sensors on such flights is very weak, and the measured temperature may deviate from that of the air, especially during daytime (Hertzog et al., 2004). In Equation 3, the air-parcel vertical displacement is inferred from Equations 1 and 2, where we have assumed that the Eulerian pressure perturbations are negligible compared to the Lagrangian ones. This assumption is notably valid for low-frequency waves, which are those that contribute the most to the temperature variances (see discussion at the end of this section).

Journal of Geophysical Research: Atmospheres 10.1029/2021JD035165

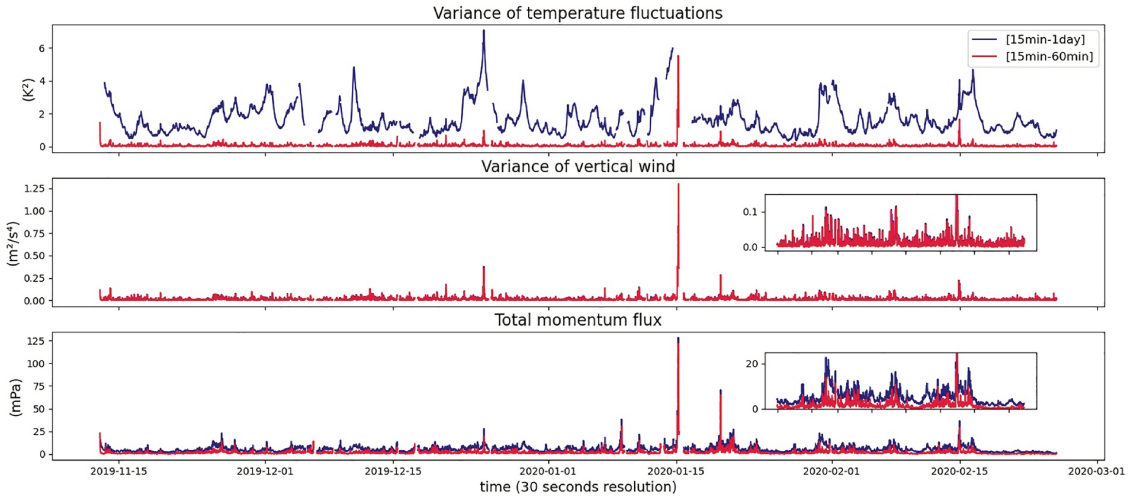

Figure 2. Timeseries of variance of temperature (top panel), vertical wind (middle panel) and total momentum flux (bottom panel) for balloon 01_STR1. Smaller graphs represent time corresponding zooms of the curves. Note the gaps in the timeseries, which correspond to balloon depressurization events.

When a superpressure balloon flies over a deep convective system at night, the associated decrease of outgoing infrared flux may cause the balloon to depressurize. In such circumstances, the balloon volume decreases, and the balloon temporarily lowers its flight level by a few hundred meters typically until the longwave flux increases back or the sun rises. During a depressurization event, the balloon behavior is therefore no longer isopycnic. Wavelet coefficients influenced by such events were discarded from the following analysis. Those events represent less than 5% of the data from all the flights.

In the following, we will use two different intrinsic-frequency bands. The wide frequency range (WF) corresponds to intrinsic periods between 15 min and 1 day, and includes a broad range of gravity-wave frequencies. The high-frequency range (HF), on the other hand, provides a focus on intrinsic periods between 15 and 60 min, and is associated with high-frequency waves that propagate nearly vertically in the atmosphere (Preusse et al., 2008). Note that the high-frequency limit of each band has been chosen to avoid concerns with either the balloon oscillations about its equilibrium density level (which occur at $\hat{\omega}_b \sim N$) with $\hat{\omega}_b$ the balloons natural frequencies, or the balloon tendency to depart from a perfect isopycnic behavior when disturbed by high-frequency waves (Vincent & Hertzog, 2014).

Figure 2 displays timeseries of the variances of temperature and vertical velocity, and of the total momentum flux for balloon 01_STR1. The blue curve corresponds to the contribution of WF waves, whereas the red curve represents the contribution of HF waves.

The temperature variance timeseries highlight the strong contrast in the behavior of the WF and HF components: the contribution of high-frequency waves to the total variance of temperature fluctuations accounts only for a very small fraction. This contrast is in agreement with the $\sim\hat{\omega}^{-2}$ scaling of gravity-wave temperature fluctuations in the lower stratosphere, which implies that waves with long-intrinsic periods are responsible for most of the temperature variance (Podglajen et al., 2016, 2020). Note also that sporadic events are responsible for most of the variations in the HF temperature variance timeseries.

The vertical-velocity variance timeseries exhibits an opposite picture: high-frequency waves are this time almost entirely responsible for the total variance. This is consistent with the nearly flat intrinsic-frequency spectrum of the vertical wind (Podglajen et al., 2016). A second major difference is associated with the variability (or intermittency) present in the vertical-velocity timeseries. Sporadic events can induce short, local peaks of vertical-velocity variance one order of magnitude larger than the baseline, which are responsible for the large tails of the probability distribution of vertical velocity described in (Podglajen et al., 2016).

Journal of Geophysical Research: Atmospheres 10.1029/2021JD035165

Table 2
Averaged Momentum Fluxes and Temperature Variances Observed During the Strateole-2 2019 campaign

	Momentum fluxes (mPa)		Temperature variances (K^2)	
Flight	15 min–1 day	15–60 min	15 min–1 day	15–60 min
01_STR1	5.42	1.97	1.64	0.08
02_STR2	4.88	1.60	1.18	0.04
03_TTL3	5.84	1.92	1.52	0.05
04_TTL1	4.96	1.34	1.31	0.03
05_TTL2	5.99	1.84	1.60	0.04
06_STR1	3.71	1.13	1.35	0.05
07_STR2	4.39	1.36	1.73	0.07
08_STR2	4.28	1.43	1.44	0.04
All flights	5.02	1.62	1.48	0.05

Note. The all flights line is the time averaged momentum fluxes from all the flights.

The total momentum flux timeseries displays an intermediate behavior between these two extremes as it results from the product of the vertical velocity with the wind horizontal component, which scales as $\hat{\omega}^{-2}$ like the temperature. This intermediate behavior corresponds to the $\sim\hat{\omega}^{-1}$ scaling of the momentum-flux spectrum (Hertzog et al., 2008; Podglajen et al., 2020). The intermittent character of momentum fluxes is observed in both the HF and WF contributions, even though HF waves contribute to only ∼1 / 3 of the total momentum flux (see also Table 2). We will show in the rest of the study that the peaks in wave activity occur when balloons are flying over deep convective systems.

2.2. Infrared Brightness Temperatures

To locate Strateole-2 balloons with respect to deep convective systems, we have used the NOAA/NCEP GPM_MERGIR product. This product consists in merged images of brightness temperature in the atmospheric window (at $\sim 11\,\mu$m) provided by European, Japanese, and U.S. geostationary satellites (Meteosat, Indoex, Himawari, GOES-W, and GOES-E). The product is available with a spatial and temporal resolution of 4 km and 30 min, respectively (Janowiak et al., 2017). To reduce the number of images to be processed and as an hourly resolution was sufficient for our purposes, we have averaged pairs of successive satellite images.

Timeseries of distance between balloons and convection have been computed from these brightness temperature images. First, the raw balloons 30-s timeseries were averaged at the same hourly resolution as the satellite images. Then, the distance between the balloon and the closest pixel with a brightness temperature lower than 235 K was defined as the balloon distance to the nearest convective system. Sensitivity tests performed on the threshold brightness temperature (±5 K difference) did not show any significant impact on the results presented in the following sections.

As a simpler proxy for the influence of underlying convective systems, we have also used the infrared brightness temperature directly below the balloons. The results obtained this way, though generally in agreement with those obtained with the distance to convection, are noisier. Convective gravity waves may actually propagate slantwise in the atmosphere, and the distance to convection therefore seems a wiser proxy to determine whether the wave activity in the balloon timeseries has a convective origin.

3. A Case Study

In this section, we use a case study to illustrate the treatment done on the balloon and brightness temperature datasets. The wave event took place in the Western Pacific Ocean (∼170°E,5°S) to the east of Solomon Islands, on January 15th, 2020. Figure 3 displays maps of infrared brightness temperatures over 10 days

Journal of Geophysical Research: Atmospheres 10.1029/2021JD035165

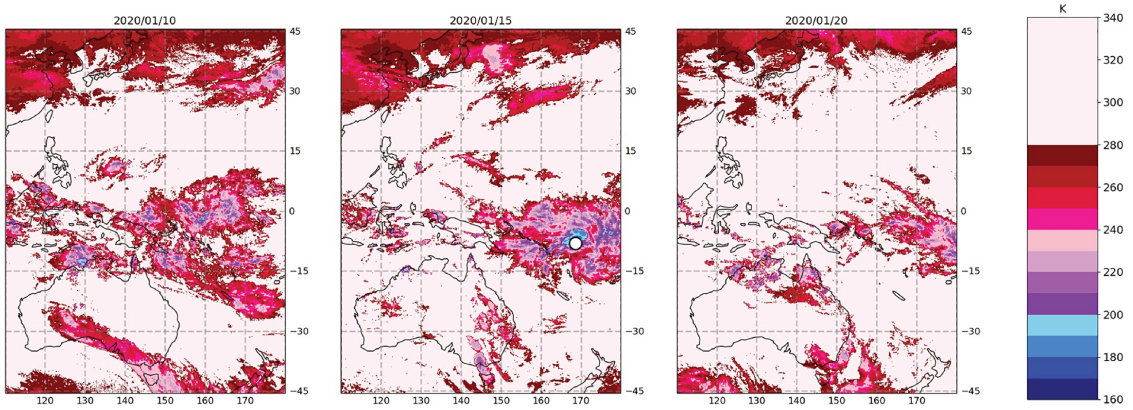

Figure 3. Maps of infrared brightness temperatures between January 10th and January 20th, 2020. Balloon 01_STR1 location on January 15th is shown with a white circle on the middle map.

centered on the event. The position of balloon 01_STR1 that recorded the event is displayed in the middle map. The maps illustrate the eastward propagation of a large-scale convective complex in the course of these 10 days. This complex is related to an active phase of a Madden-Julian Oscillation event (Madden & Julian, 1971, 1972; Zhang & Mu, 2005). The convection is particularly active on January 15th, and balloon 01_STR1 is flying over the center of the convective area on that day.

Figure 4 presents a zoom on the convective complex from January 14th 19 UT to January 15th 23 UT. The beginning of this 1-day time period, which corresponds to the morning (6 LT to 12 LT), is characterized by the development of several isolated convective systems within the complex. Most of these systems progressively dissipate during the afternoon. Yet, a system located in the center of the convective complex, right below balloon 01_STR1 position, intensifies from mid-afternoon (15 LT) on to the sunset (18 LT). Shortly after, the convection is re-activated over the whole complex, producing a wide area of brightness temperatures below 200 K. Whatever the time during that day, balloon 01_STR1 remains within 4 km from a "convective" pixel, that is, less than a pixel away from brightness temperatures lower than 235 K.

The sunset and the wide area of low infrared flux are the reasons that cause balloon 01_STR1 to depressurize for 10 h. The corresponding period is shown with red-framed maps in Figure 4. The balloon records associated with the depressurization event are discarded from our analysis.

Figure 5 displays the total WF and HF components of the gravity-wave momentum flux estimated from balloon 01_STR1 observations over a 30-h period centered on January 15th, 2020. Missing data in this figure are associated to the depressurization of balloon 01_STR1. Both momentum flux timeseries exhibit a marked increase after 02 UT (13 LT) on January 15th. This timing corresponds to the development of the convective system in the center of the convective complex. The WF momentum flux typically undergoes a variation of one to two orders of magnitude, with a peak value over 120 mPa. More than half of this increase is accounted for by high-frequency waves, which vary by two orders of magnitude. In agreement with Lane et al. (2001), this increase in momentum fluxes seems to correspond to the developing phase of the convective system. In particular, momentum fluxes associated with both frequency ranges exhibit some decrease just before the balloon depressurization, at which stage the convective system is more mature and less prone to trigger gravity waves (Stephan & Alexander, 2015). This decrease is even more drastic in the high-frequency component. Momentum flux values estimated right after the balloon has pressurized back (at sun rise) are similar to those observed prior to the peak, despite the large area of low brightness temperatures that remains at that time (see 18 UT, 7 LT on January 15th in Figure 4). Of course though, one can not rule out other episodes of increased momentum flux during

Journal of Geophysical Research: Atmospheres 10.1029/2021JD035165

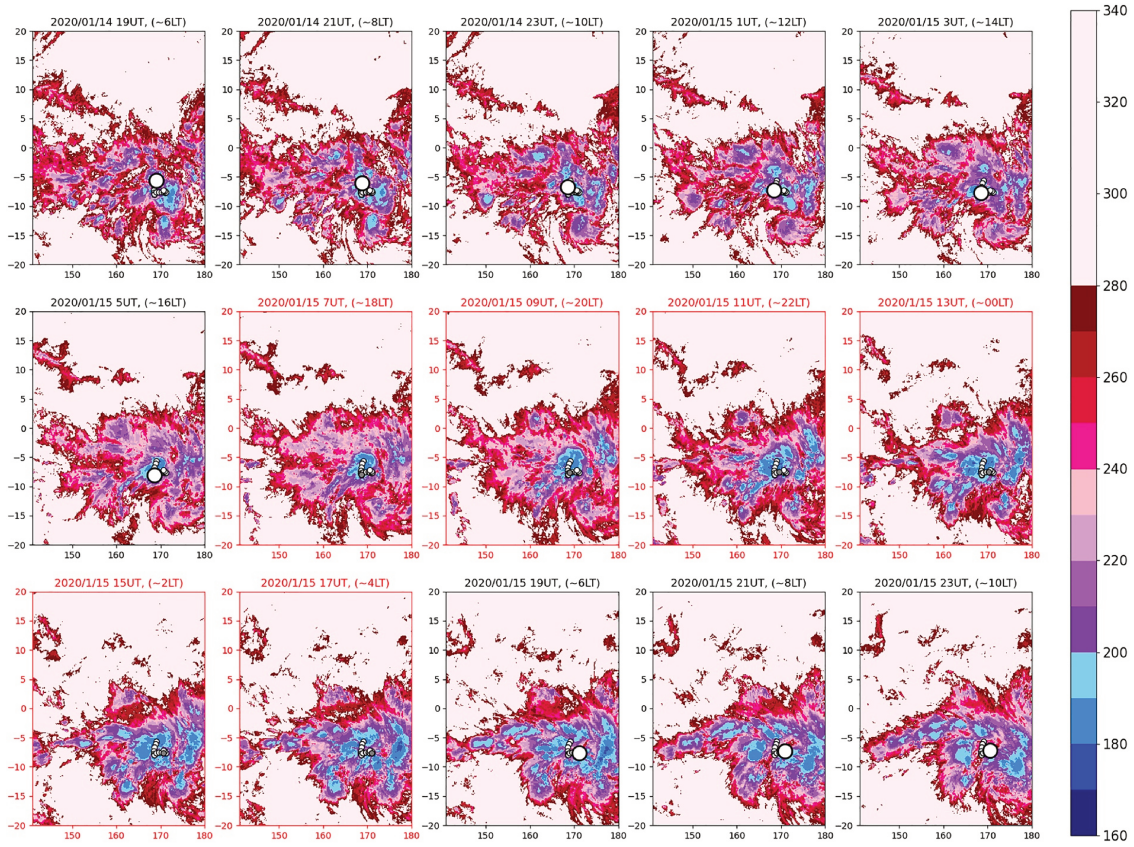

Figure 4. Same as Figure 3, but from January 14th 20 UT to January 15th 20 UT. The large white circle on each map represents balloon 01_STR1 position at the corresponding date and time. The lower white circles show the balloon trajectory during this 1-day period. Maps with red axes and title correspond to the time period during which the balloon depressurized. In these maps, the balloon position is indicated with a small gray circle, distance to convection was less than 4 km all along.

the balloon depressurization. We finally notice that the hourly resolution of momentum fluxes (dots in Figure 5) is sufficient to represent the major variation of this wave event given the frequency range under investigation. Those averaged momentum fluxes are used in the next section in association with distances to convection to quantify statistically the relation between momentum fluxes and distance to convection.

The oceanic convective event depicted in this case study illustrates the complexity associated with the organization of tropical convection. Regarding gravity-wave generation, superpressure balloons observations collected in the direct vicinity of such systems therefore provide a quantitative assessment of gravity-wave activity that complement numerical simulations, which tend to address more idealized situations (Lane et al., 2001; Lane & Sharman, 2006; Lane & Zhang, 2011). Note that the case study depicted here corresponds to the largest momentum-flux event identified during the eight balloon flights of the 2019 Strateole-2 campaign. About five events with momentum-flux values larger than 60 mPa have been identified in those flights. Events associated with values lower than 40 mPa are, on the other hand, more common (see next Section). This event was chosen to illustrate a clear event of convectively generated waves, with the balloon located right above the convective area, together with an episode of depressurization. These depressurization events altogether represent less than 5% of the data.

Journal of Geophysical Research: Atmospheres 10.1029/2021JD035165

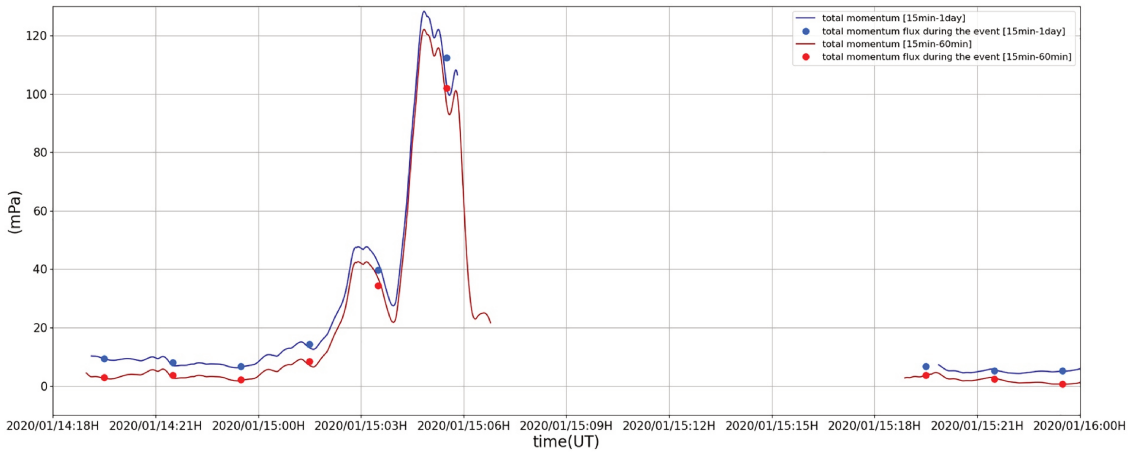

Figure 5. Gravity-wave total momentum flux estimated from balloon 01_STR1 observations around January 15th, 2020. Dots on each curve represent the hourly averaged momentum flux associated with maps shown in Figure 4.

4. Statistical Results

We now statistically examine the whole 30-s data set recorded during the eight flights of the 2019 campaign. Timeseries associated with STR and TTL balloons have been treated altogether, after careful examination that the differences between flights were not attributable to physical factors (e.g., different flight levels), but resulted from different sampling of the tropical area. This is illustrated by the summary statistics for each flight given in Table 2.

Figure 6 shows boxplots of total momentum fluxes for WF and HF waves displayed with respect to the balloon distance to convection. The distance bins have been chosen to ensure a minimum number of 300 observations per bin to reduce the noise in the distribution tails, and with a finest resolution of 25 km. The most prominent feature exhibited by these boxplots is the monotonic decrease of gravity-wave momentum fluxes as distance to convection increases. This is a clear confirmation that deep convection constitutes the main source of gravity waves in the tropics (Alexander et al., 2008; Alexander & Pfister, 1995; Ern et al., 2004; Lane et al., 2001). One can also notice that this decrease is steeper for high-frequency waves than for waves with longer periods. Whereas mean momentum fluxes associated with HF waves differ by a factor ∼5 when observations are performed within 25 km or 1,000 km away from a convective system, momentum fluxes associated with WF waves vary only by a factor ∼2.5. This differential variation is likely linked to the fact that high-frequency waves propagate almost vertically in the atmosphere, and are thus preferentially observed close to their source in the lower stratosphere. On the other hand, the more oblique propagation of longer waves enables them to be observed farther away from their source region. Other sources than convection may also contribute to the observed background gravity-wave activity.

The other striking feature of momentum fluxes displayed in Figure 6 is the inter-quartile range between the 10th to 90th quantiles in each distance bin. This range expresses how widely momentum fluxes may vary when observations are performed at a given distance from convection. Figure 6 shows that gravity-wave momentum fluxes are significantly more variable close to convection than farther away. This is even more conspicuous for the higher frequency waves considered in this study: in the 15–60 min frequency band, the 10th quantile hardly varies with the distance of the balloon to convection, whereas the 90th percentile undergoes a factor ∼5 variation. This statistical increase in the range of momentum fluxes close to convection has been already noted in the previous section: it is likely linked to the preferred generation of gravity waves at specific stages of the convection life cycle and/or filtering of directional propagation. The intermittent nature of convective gravity waves is also illustrated in Figure 6 by the larger departure close to convection between the mean and median momentum fluxes in each distance bin.

Journal of Geophysical Research: Atmospheres 10.1029/2021JD035165

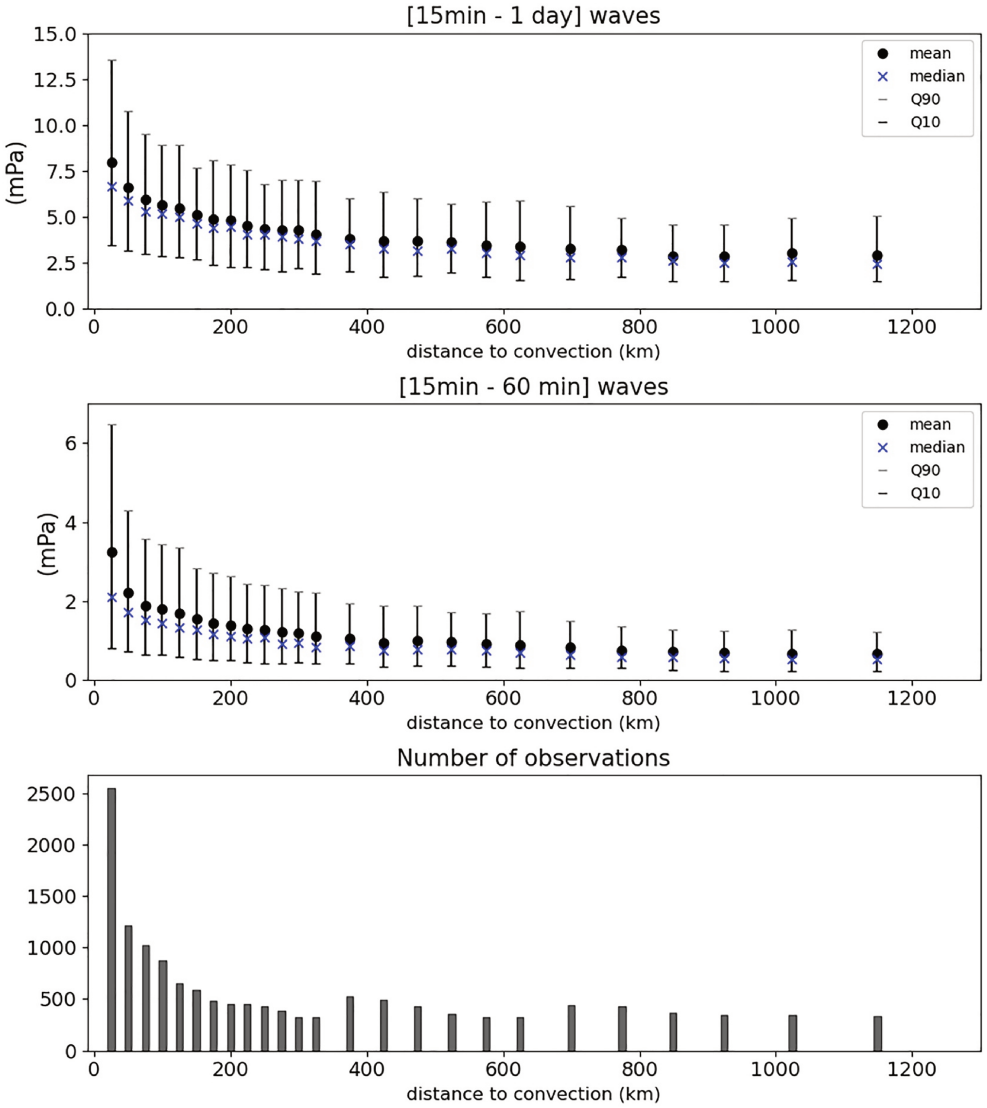

Figure 6. Boxplots of total momentum fluxes associated with (top) WF waves and (middle) HF waves with respect to the balloons distance to convection. In both panels, the mean, median, as well as the 10^{th} and 90^{th} quantiles in each bin are presented. (Bottom) Number of observations within each distance bin.

Last, it is also interesting to note that at a distance of more than 300 – 400 km away from convective systems, momentum fluxes associated with gravity waves in the tropical lower stratosphere look rather constant (typically 3 mPa for 15 min–1 day waves), which would support some background values in gravity-wave drag parameterizations.

The lowest panel of Figure 6 displays the number of observations per bin of distance to convection. This panel emphasizes how often the balloons were located close to convective systems during the 2019 campaign: observations were collected less than 200 km away from convection more than half of the time (53%), and less than 50 km away more than a quarter of the time (26%).

To further exemplify the relation of tropical gravity waves to convection, we show in Figure 7 the reverse distribution: boxplots of distance to convection with respect to WF- and HF-wave momentum fluxes. As previously, we have ensured a minimum number of 300 observations per bin. The figure clearly illustrates

Journal of Geophysical Research: Atmospheres 10.1029/2021JD035165

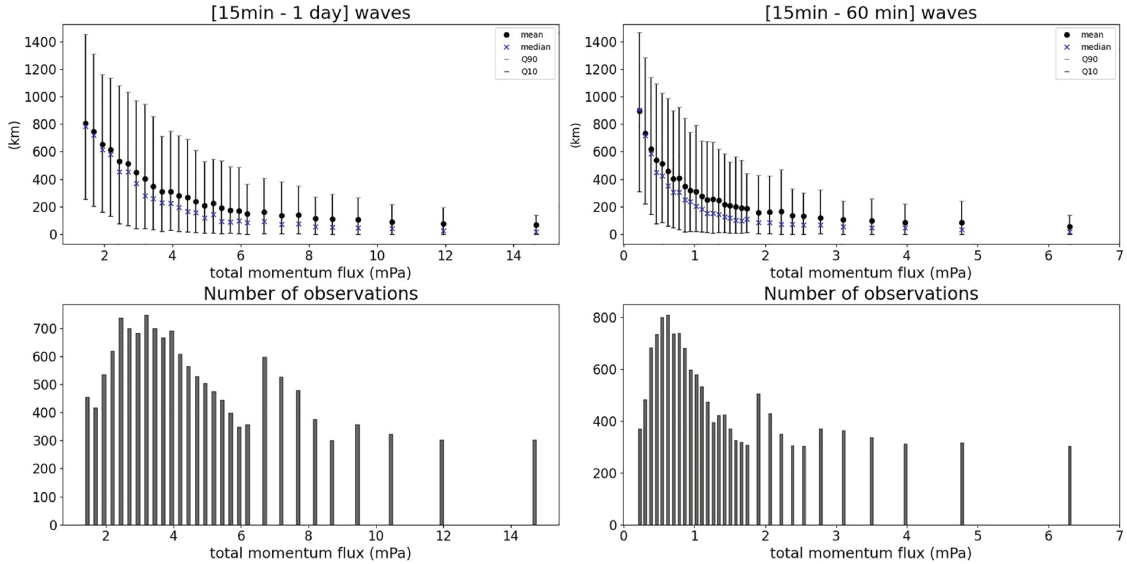

Figure 7. (Top) Boxplots of distance to convection with respect to gravity-wave momentum fluxes associated with (left) WF and (right) HF waves. The same quantities as in Figure 6 are displayed. (Bottom) Number of observations per momentum-flux bin.

that the largest momentum fluxes (>5 mPa) are only recorded when the balloons are located at short distances from convective systems, typically less than 400 km away. In contrast, and as previously noticed, lower momentum fluxes are generally associated with larger distances to convective systems, but may also be observed sometimes in the vicinity of such systems. Note that the smallest momentum fluxes (<2 mPa

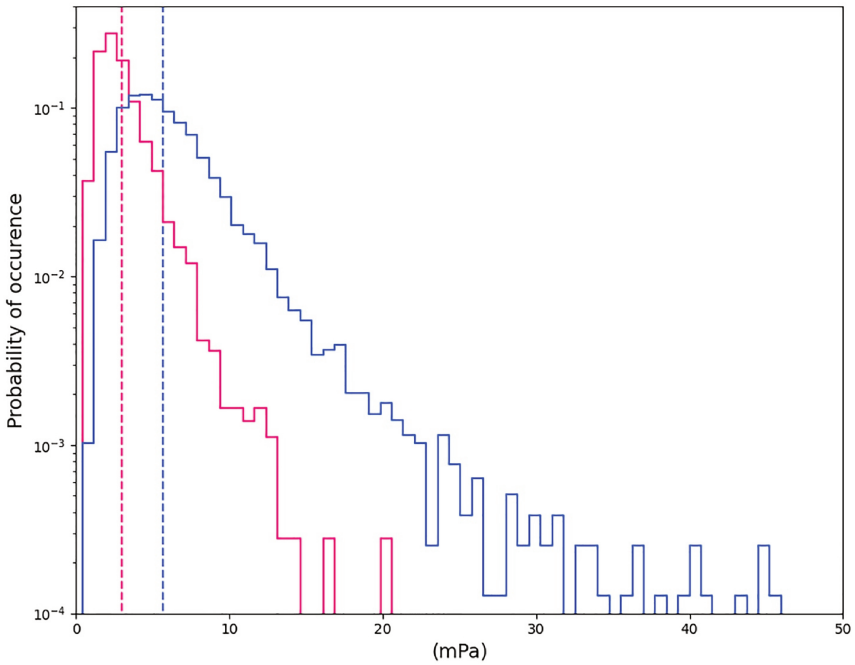

Figure 8. Pdf of momentum flux for WF waves: (pink) observations collected more than 500 km, and (blue) observations collected less than 200 km away from a convective system. Vertical dashed lines represent the corresponding means.

Journal of Geophysical Research: Atmospheres 10.1029/2021JD035165

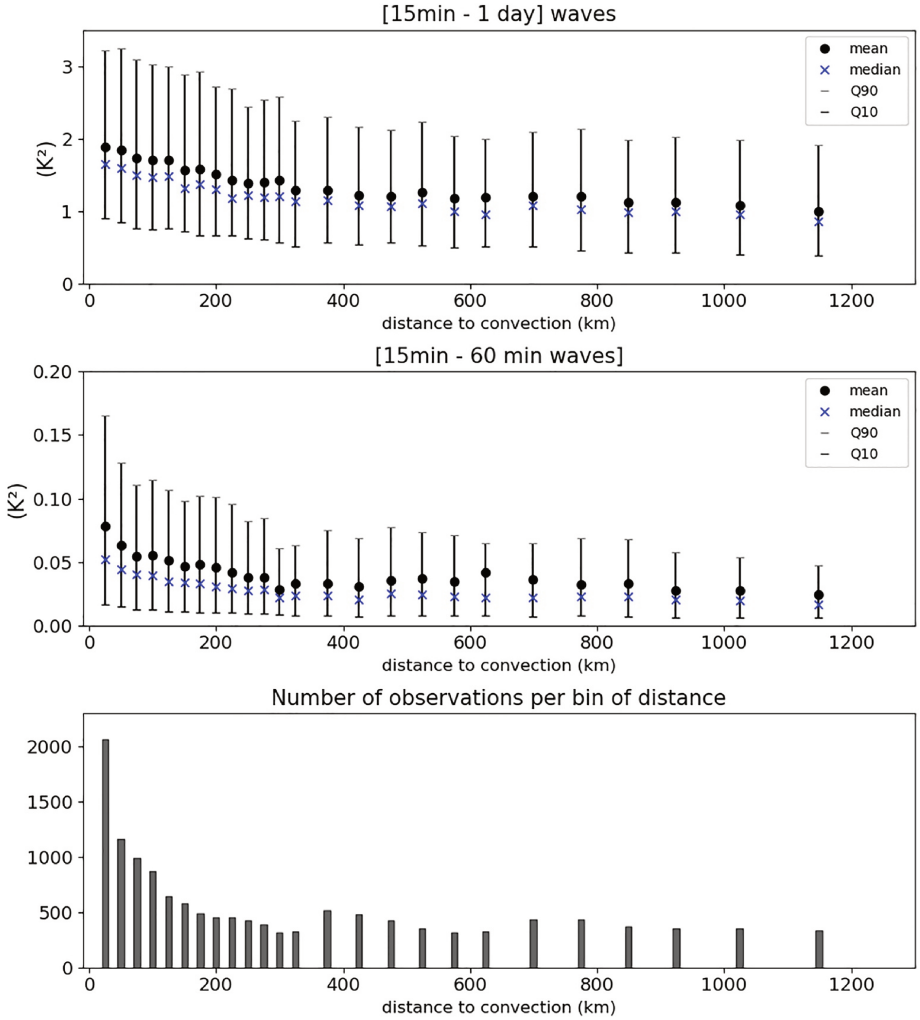

Figure 9. Same as Figure 6, but for gravity-wave temperature variances.

for WF waves, and <0.5 mPa for HF waves) are not observed in the direct proximity of convection. These two figures have hence demonstrated that a short distance to convective systems is a necessary, but not sufficient condition to observe large gravity-wave momentum fluxes in the tropical lower stratosphere. In other words, convection is the most prominent gravity wave source in the tropics, but the generation process is intermittent.

We finally display in Figure 8 the probability distribution function (pdf) of momentum fluxes associated with WF waves. We show the pdf obtained with observations collected more than 500 km away from convection, as well as that obtained with observations collected less than 200 km away from a convective system. The two pdfs differ remarkably from each other, the one associated with observations close to convection exhibiting a larger tail of large-amplitude wave events, in agreement with previous figures. Jewtoukoff et al. (2013) also reported on gravity-wave momentum-flux pdf in the tropical area during the Pre-Concordiasi campaign. Despite similar averaged momentum fluxes (i.e., between 4 and 5 mPa), Jewtoukoff et al. (2013)'s pdfs have significantly longer tails than those obtained in this study. In their study, Jewtoukoff et al. (2013) did not remove the balloon depressurization events, unlike what is done here. This difference in treatment may explain the observed differences in the pdfs, since depressurization events

Journal of Geophysical Research: Atmospheres 10.1029/2021JD035165

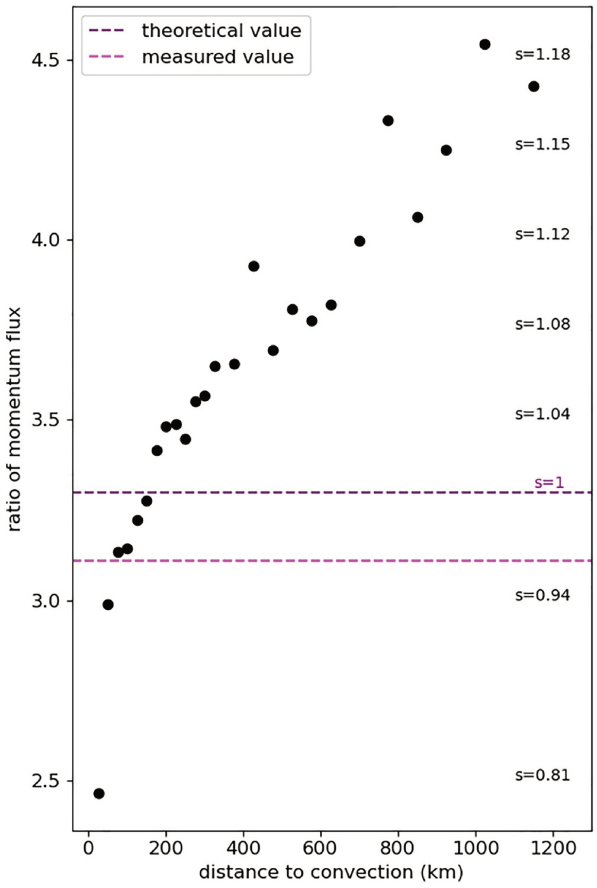

Figure 10. Ratio of WF-wave (15 min–1 day) to HF-wave (15 min–60 min) momentum fluxes as a function of balloon distance to convection. The purple horizontal line shows the ratio associated with the $\hat{\omega}^{-1}$-scaling of momentum fluxes. The measured power-law scaling is shown by the pink horizontal line. The correspondence between the WF to HF momentum-flux ratios and the power-law scalings is displayed on the right-hand side of the figure.

may be associated with large vertical displacements of the balloons. Furthermore, momentum fluxes are overestimated during such events as the balloon is no longer isopycnic.

For completeness, we also show in Figure 9 boxplots of temperature variances associated with gravity-wave disturbances with respect to the balloon distance to convection. The general behavior of temperature variances is similar to that of momentum fluxes: larger variances are observed closer to convection, and the largest temperature variances (represented by the 90th quantiles) are strongly linked to convective systems. Yet, the range of variation of the mean temperature variances is significantly smaller than that of momentum fluxes: it varies by typically less than a factor 2 for WF waves when the balloon distance to convection changes from 0 to 1,000 km. Values level off to a background value from 400 km on at 1.2 K^2 for WF waves. This is reminiscent of timeseries displayed in Figure 2, which showed less intermittency in temperature variances than in momentum fluxes. In contrast with momentum fluxes, temperature variances therefore appear less strongly linked to gravity-wave sources in the tropical lower stratosphere, which is consistent with the larger contribution of low-frequency waves that propagate more horizontally in those variances, as discussed in Section 2.

5. Discussion

5.1. Ratio Between HF and WF Waves

It is common to characterize gravity waves in terms of universal spectra. For example, numerous studies have provided evidence that gravity-wave energy scales as m^{-3}, with m the vertical wavenumber (Fritts & Alexander, 2003, and references therein). Similarly, long-duration balloon observations have shown that the spectrum of gravity-wave momentum fluxes scales as $\hat{\omega}^{-s}$ with $s = 1$ (e.g., Hertzog et al., 2008). Such laws imply a constant ratio between different ranges of wavenumbers or frequencies. For instance, the ratio of momentum fluxes associated with WF and HF reads:

$$\frac{\int_{\mathrm{WF}} \overline{u'_{\parallel} w'}(\hat{\omega}) d\hat{\omega}}{\int_{\mathrm{HF}} \overline{u'_{\parallel} w'}(\hat{\omega}) d\hat{\omega}} = \frac{\ln \frac{86400}{900}}{\ln \frac{3600}{900}} \approx 3.3 \tag{4}$$

assuming the $\hat{\omega}^{-1}$ scaling.

Results shown in the previous sections indicate that this ratio is only statistically valid in the tropical lower stratosphere. It holds when observations collected over different meteorological situations are averaged altogether. Indeed, Figure 6 for instance shows that momentum fluxes associated with HF waves are more sensitive to the distance to convection than those associated with WF waves. This result is further explored in Figure 10, which displays the ratio of WF to HF wave momentum fluxes as a function of the balloon distance to convection. It is obvious that this ratio increases as waves observations are collected farther away from convection. In other words, short-period waves contribute more to the total momentum flux close to convection than they do far away. The momentum-flux spectral slope consequently varies by a few percents as well with the proximity to convective wave sources, at least in the tropical lower stratosphere. It might well be that this dependence is lost farther above (when the distance to the wave sources has increased), but this remains to be explored. The 3.3 momentum-flux ratio, associated with the $\hat{\omega}^{-1}$ scaling, thus only corresponds to a mean value, which is close to the mean value measured 3.1 during the campaign.

Journal of Geophysical Research: Atmospheres 10.1029/2021JD035165

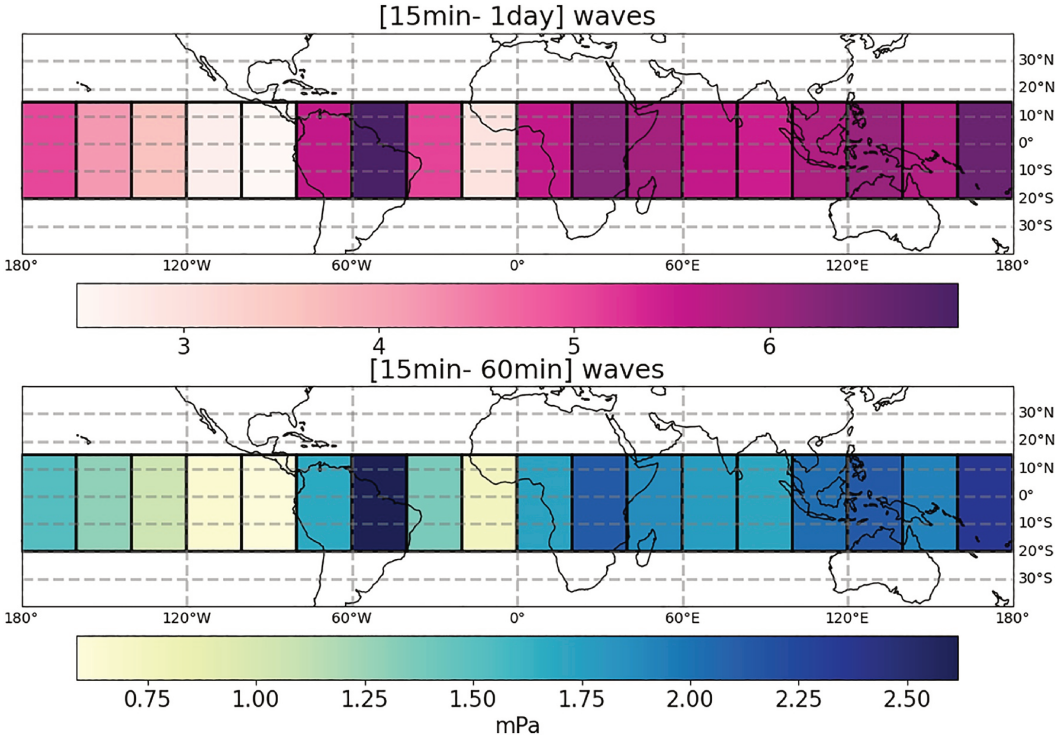

Figure 11. Maps of campaign-mean momentum flux: (top) 15 min–1 day waves, (bottom) 15 min–60 min waves.

5.2. Geographic Distribution of Gravity-Wave Momentum Fluxes

The previous sections have stressed the link between gravity-wave activity in the tropical lower stratosphere and deep convection below. In this section, we report on the associated geographic distribution of gravity-wave momentum fluxes in the tropical lower stratosphere.

Figure 11 displays maps of WF and HF wave momentum fluxes averaged over all flights in 20°-longitude bins. The geographical bins encompass the whole 20°S – 15°N latitude range sampled by the balloons, since the number of collected observations during the first Strateole-2 campaign did not enable us to clearly demonstrate inter-hemispheric differences. Both maps highlight a clear contrast between quieter regions (Eastern Pacific Ocean, Eastern Atlantic Ocean) and more active regions (South America, Eastern Africa, and the Maritime Continent), in agreement with maps from Randel et al. (2021). The amplitude of geographic variability is different than that of Randel et al. (2021), but this difference is certainly associated with their use of temperature disturbances to study gravity waves, while we have chosen momentum fluxes. Ern and Preusse (2012) also reported on 20 – 30% enhancements in gravity-wave momentum fluxes over convective regions as compared to non-convective ones. The variability of wave momentum fluxes displayed in Figure 11 is somewhat larger, which is likely associated with the capability of superpressure balloons to observe higher-frequency waves than the High Resolution Dynamics Limb Sounder (HIRDLS) instrument used in Ern and Preusse (2012).

Momentum fluxes are found generally larger above the continents than above the oceans. Yet, the western part of the South Pacific Convergence Zone stands out as the second region with largest wave activity. The convection there was particularly active during the campaign, as highlighted in the case study shown previously. The geographic behavior of gravity-wave momentum fluxes is in line with properties of tropical convection in the troposphere: regions associated with larger momentum fluxes are also those where convective systems are more prone to overshoot in the upper troposphere (Alcala & Dessler, 2002; Liu & Zipser, 2005).

Journal of Geophysical Research: Atmospheres 10.1029/2021JD035165

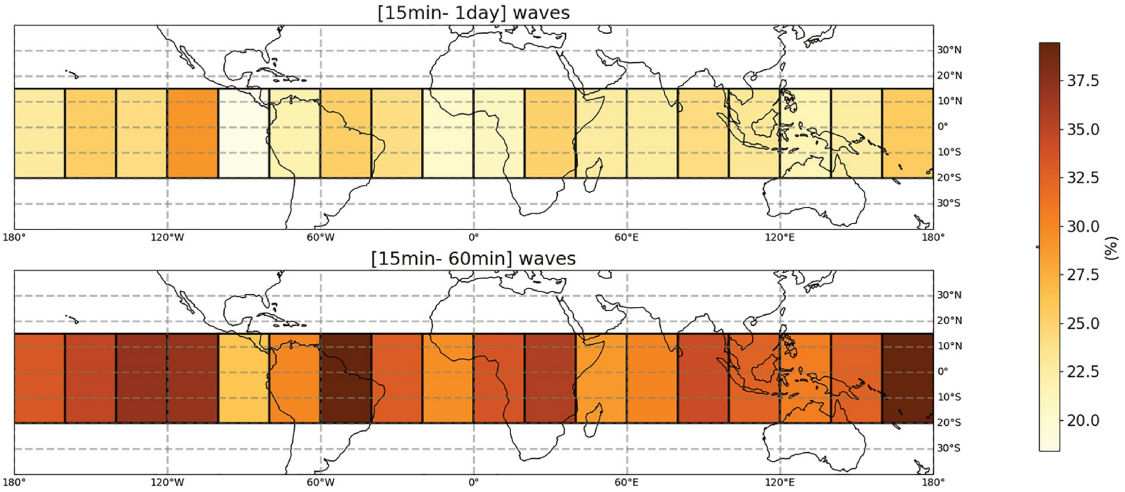

Figure 12. Contribution of the top 10% momentum-flux events to the mean momentum flux: (top) 15 min–1 day waves, (bottom) 15 min–60 min waves.

WF and HF wave maps look very similar, except for a slightly larger decrease in the HF-wave momentum fluxes away from the most active regions. The width of the longitude bins used here is indeed too large to capture the differential behavior of short- and long-period waves with respect to the convective source that was stressed in the previous sections. We finally note the striking west-east monotonic decrease in wave momentum fluxes over the Pacific Ocean, and, on the other hand, the relatively uniform distribution of momentum fluxes over the Indian Ocean. This latter feature is likely linked to the historically anomalous positive event of the Indian Ocean Dipole (IOD) that took place in 2019 (Lu & Ren, 2020). In a positive IOD phase, equatorial sea surface temperatures in the western Indian Ocean are warmer than their climatological values. Such positive IOD phases therefore reduce the climatological positive west-east gradient in convection over the basin (Saji et al., 1999; Webster et al., 1999), and thus likely contribute to a more balanced distribution of wave activity in that region.

Figure 12 shows maps of the contribution of the top 10% momentum-flux events to the mean momentum flux, for both the WF- and HF-bands considered in this study. These contributions are computed as:

$$\frac{\sum\limits_{f_i > f_{q90}} f_i}{N_{\text{obs}}} \times 100 \Big/ \sum_{i=1} f_i \tag{5}$$

where f_i represents the instantaneous momentum flux integrated in either the WF or HF frequency band, f_{q90} the associated 90^{th} quantile, and N_{obs} the number of observation points. Those maps therefore characterize the intermittency of gravity waves in the equatorial lower stratosphere (Alexander et al., 2010; Hertzog et al., 2012; Plougonven et al., 2013; Wright et al., 2013).

In agreement with the raw timeseries displayed in Figure 2, Figure 12 shows that the intermittency associated with the highest-frequency waves is significantly larger than that obtained when the full 15 min–1 day band is considered: the top most 10% events contribute to 30–40% of the mean momentum flux associated with HF waves, whereas their contribution to the WF-wave momentum fluxes is ~ 25%. This difference is likely partly explained by the rapid decrease of HF-wave momentum fluxes with the distance to the convective source, which was emphasized in the previous section. But it may also result from differences in the range of source mechanisms contributing to different parts of the gravity wave spectrum.

In general, bins with the largest momentum fluxes are also those with the highest intermittency. This likely reflects the transient nature of the convective wave source and its modulation at a broad range of timescales: the life cycle of convection itself, diurnal cycle, equatorial Kelvin or Rossby waves, longer-period MJO

Journal of Geophysical Research: Atmospheres 10.1029/2021JD035165

events. Yet some interesting discrepancies between maps of momentum fluxes and those of intermittency are worth highlighting. The wave intermittency is, for instance, larger around 120°W than it is nearby. Similarly, it is larger over the eastern Indian Ocean than over its western part. We have no clear interpretation for these "outliers," but note that they may result from a combination of causes, including a more transient nature of convection in these bins or the result of a limited sampling by the 2019 balloon flights. Last, we note that the intermittency values reported in this study agree fairly well with those obtained by Wright et al. (2013) and Ern et al. (2014) in the tropical lower stratosphere with satellite observations. Hertzog et al. (2012) and Wright et al. (2013) reported on much larger figures at higher latitudes, where orographic waves represent a significant fraction of the gravity-wave momentum flux. There, the top 10% waves may contribute to more than 60% of the mean momentum flux. Our study therefore confirms that the intermittency associated with convective waves, while obviously present in the balloon data set, is rather moderate.

5.3. Gravity-Wave Contribution to the Driving of the QBO

In this following discussion, we intend to provide a rough assessment of the contribution of the gravity waves observed during the balloon campaign to the overall driving of the QBO. For this, we start from a simplified version of the Transformed Eulerian Mean equation for zonal momentum (Andrews et al., 1987):

$$\rho\left(\frac{\partial\overline{u}}{\partial t}+\overline{w}^{\star}\frac{\partial\overline{u}}{\partial z}\right)=-\frac{\partial\rho\overline{u'w'}}{\partial z} \tag{6}$$

where $\overline{u}$ is the zonal-mean zonal wind, and $\overline{w}^{\star}$ is the residual vertical velocity. In Equation 6, we have followed Alexander and Ortland (2010) and have neglected the meridional advection term. This primarily stems from the fact that the QBO is essentially symmetric about the equator, and that the Coriolis force is small at low latitudes: more than 80% of the balloon observations have actually been recorded within 10° of the equator. Ern et al. (2014) and Pahlavan et al. (2021) have further examined the tropical stratosphere momentum budget in the European Center for Medium-range Weather Forecasts (ECMWF) reanalyzes ERA-Interim and ERA-5 reanalyzes, respectively. They both suggest that the meridional advection term is indeed very weak during westerly to-easterly QBO transitions, which was the configuration during the balloon campaign.

Integrating (6) from the balloon flight level (z_{bal}) to the QBO top altitude (z_{top}) yields:

$$\rho\overline{u'w'}(z_{\mathrm{bal}})-\rho\overline{u'w'}(z_{\mathrm{top}})=\int_{z_{\mathrm{bal}}}^{z_{\mathrm{top}}}\rho\left(\frac{\partial\overline{u}}{\partial t}+\overline{w}^{\star}\frac{\partial\overline{u}}{\partial z}\right)dz \tag{7}$$

Noting $\frac{d\overline{u}}{dt}$ the total zonal-wind acceleration (i.e., the term within parentheses under the integral in Equation 7, and assuming that most momentum flux has been dissipated at the QBO top altitude, one can use the mean value theorem for definite integrals to obtain:

$$\begin{aligned}\overline{u'w'}(z_{\mathrm{bal}}) &= \frac{d\overline{u}}{dt}(z^{*})\int_{z_{\mathrm{bal}}}^{z_{\mathrm{top}}}\rho dz\\ &= \frac{d\overline{u}}{dt}(z^{*})\left[1-\exp\left(-\frac{z_{\mathrm{top}}-z_{\mathrm{bal}}}{H}\right)\right]H\end{aligned} \tag{8}$$

where $H\approx 6$ km is the density scale height for a background temperature of 210 K typical of the tropical lower stratosphere, and z^{*} is an altitude such that $z_{\mathrm{bal}}<z^{*}<z_{\mathrm{top}}$. In the tropical lower stratosphere, the absolute value of the total zonal wind acceleration reaches up to to 0.5 m/s/day in QBO easterly shear zones (Alexander et al., 2010; Ern et al., 2014; Pahlavan et al., 2021). Such accelerations are preferentially found above ~25 km, and generally occupy less than half of the QBO altitude range (Pahlavan et al., 2021). We thus use $\frac{d\overline{u}}{dt}(z^{*})=0.5$ m/s/day as a maximum value for the density-weighted total acceleration, and half of this as a more probable estimate, yet likely still an upper bound.

By conveniently choosing $z_{\mathrm{top}}=z_{\mathrm{bal}}+10$ km, one gets an estimate of the needed flux to drive the QBO:

$$\rho\overline{u'w'}(z_{\mathrm{bal}})\approx 2.8-5.6\mathrm{mPa} \tag{9}$$

Journal of Geophysical Research: Atmospheres 10.1029/2021JD035165

Now, the 15 min–1 day absolute gravity-wave momentum flux estimated from the balloon observations is ∼5 mPa (see Table 2). Of this total, 1.4 mPa correspond to westward fluxes, so that 15 min–1 day waves are responsible for at least 25%, and more probably over 50%, of the required flux to drive the QBO above 20 km of altitude during the balloon campaign. This estimate is in agreement with for example, Kawatani et al. (2010) who stressed the primary role of gravity waves in driving the descent of QBO easterlies.

6. Summary and Conclusion

Tropical gravity waves have been studied from the observations collected during the eight balloon flights of the first Strateole-2 campaign, which took place from November 2019 to February 2020. The quasi-Lagrangian nature of the superpressure balloons provides direct access to the intrinsic frequencies of the waves observed, and allows an accurate estimation of the associated momentum fluxes. The main focus of the study was on the relation between gravity wave momentum fluxes and the presence of deep convection nearby. Deep convection was diagnosed from geostationary satellite images of brightness temperature, and the observations were sorted using a simple criterion: the distance from the balloon to the nearest convective system, identified as brightness temperatures lower than 235 K.

The spectrum of gravity waves considered in the analysis consisted of motions with intrinsic periods ranging from 15 min, about three times the buoyancy period, to one day. Periods shorter than 15 min were not considered so as to avoid effects due to the balloon natural oscillations (Podglajen et al., 2016). The campaign-averaged gravity-wave momentum flux is 5 mPa, and the observed maximum value reaches 120 mPa, on a timescale of a couple of hours. In complement to this broad frequency range, a subrange of high frequencies (intrinsic periods from 15 to 60 min) was considered. The campaign-average momentum flux for these high frequencies is 1.61 mPa, about 32% that of the broad frequency range, emphasizing their importance.

When momentum fluxes are sorted according to the distance to convection, a very clear dependence is found. Gravity-wave momentum fluxes show both larger values and greater variability close to convection: 90% of the momentum fluxes larger than the mean are typically found at distances closer than 400 km from convection (see Figure 7). Conversely, momentum fluxes recorded at distances further away than 600 km from convection have more than 90% of chance of being lower than the mean (see Figure 6). These results clearly confirm that convection is the main source of gravity waves in the tropics.

The relation between momentum fluxes and convection is more pronounced for the highest frequency waves. The decay of the momentum fluxes at larger distances from convection is faster for HF waves than it is for WF waves, and far away from convection, the HF-wave momentum fluxes tend to a very small value (∼0.6 mPa). This contrasts with WF waves, for which momentum fluxes tend to a "background" value of about 3 mPa far away from convection. The larger spatial scales and more horizontal propagation of WF waves leads to looser relation to the convective sources. The greater contrast for HF waves between the vicinity of convection and regions remotely distant from all convection also translates in a large intermittency for these HF waves: their 10% highest values contribute to 40% of their momentum fluxes. This intermittency is weaker nonetheless than for mountain waves at higher latitudes. Convective sources are numerous and the observed samples were most often close to convection: more than 50% of time closer than 200 km. The intermittency and the relative contributions of HF to WF are consistent with the −1 slope in intrinsic frequency found for gravity wave momentum fluxes (Podglajen et al., 2016). Whereas the notion of a universal spectrum is valid for the average over all flights, or for long enough portions of flights, its relevance for shorter portions of flights should be more nuanced. This was illustrated by quantifying the ratio of the HF and WF contributions depending on distance to convection. A clear dependence was found, consistently showing greater weight of HF waves near convection (up to 40% of the momentum fluxes), and weaker weight far from convection (HF waves only account for about 22% of fluxes at ~ 1000 km or more).

In contrast to momentum fluxes, temperature fluctuations show much less intermittency. Their spectrum has a −2 slope in intrinsic frequency, implying a much greater weight of low frequency waves. The overall

Journal of Geophysical Research: Atmospheres 10.1029/2021JD035165

average of temperature variances was 1.48 K^2 for the whole spectrum of waves, with the average for HF waves only reaching 0.05 K^2. This is 29.6 times less than the total variance, consistent with the 31.7 ratio expected for a −2 spectrum. Temperature variances nonetheless also show a clear sensitivity to distance to convection, but with a less pronounced decay, and relatively larger background values found at large distances from convection (see Figure 9).

The data set from this first Strateole-2 campaign has allowed a first exploration of gravity wave momentum fluxes in the lower stratosphere and of their relation to the surrounding flow. Directions to pursue include consideration of a more integrative diagnostic for convection nearby, accounting for the time development of convection and for the direction of the shear between the convection and the balloons. Upcoming Strateole-2 campaigns, with 20 balloons each planned for 2021–2022 and 2024–2025, will allow us to investigate and quantify convectively generated gravity waves over an even wider sample of events and configurations.

Conflict of Interest

The authors declare no conflicts of interest relevant to this study.

Data Availability Statement

The balloon-borne TSEN data were collected as part of Strateole-2, which is sponsored by CNES, CNRS/INSU, NSF, and ESA. The Strateole-2 TSEN data set is available at https://data.ipsl.fr/catalog/strateole2/. The merged IR satellite images were collected from the NOAA/NCEP GPM_MERGIR product, available at https://disc.gsfc.nasa.gov/datasets/GPM_MERGIR_1/summary.

Acknowledgments
Martina Bramberger and Joan Alexander are warmly thanked for thoughtful discussions and suggestions during the final stage of the paper. This study was supported by ANR Booster. Milena Corcos is funded through a Sorbonne-Universite and CNES doctoral fellowship.

References

Alcala, C. M., & Dessler, A. E. (2002). Observations of deep convection in the tropics using the Tropical Rainfall Measuring Mission (TRMM) precipitation radar. *Journal of Geophysical Research*, *107*, 17-1-17-7. https://doi.org/10.1029/2002JD002457

Alexander, M. J., Geller, M., McLandress, C., Polavarapu, S., Preusse, P., Sassi, F., et al. (2010). Recent developments in gravity-wave effects in climate models and the global distribution of gravity-wave momentum flux from observations and models. *The Quarterly Journal of the Royal Meteorological Society*, *136*, 1103–1124. https://doi.org/10.1002/qj.637

Alexander, M. J., Gille, J., Cavanaugh, C., Coffey, M., Craig, C., Eden, T., et al. (2008). Global estimates of gravity wave momentum flux from High Resolution Dynamics Limb Sounder observations. *Journal of Geophysical Research*, *113*, D15S18. https://doi.org/10.1029/2007jd008807

Alexander, M. J., Holton, J. R., & Durran, D. R. (1995). The gravity wave response above deep convection in a squall line simulation. *Journal of the Atmospheric Sciences*, *52*, 2212–2226. https://doi.org/10.1175/1520-0469(1995)052<2212:tgwrad>2.0.co;2

Alexander, M. J., & Ortland, D. A. (2010). Equatorial waves in High Resolution Dynamics Limb Sounder (HIRDLS) data. *Journal of Geophysical Research*, *115*(D24), D15S18. https://doi.org/10.1029/2010jd014782

Alexander, M. J., & Pfister, L. (1995). Gravity wave momentum flux in the lower stratosphere over convection. *Geophysical Research Letters*, *22*, 2029–2032. https://doi.org/10.1029/95GL01984

Andrews, D. G., Holton, J. R., & Leovy, C. B. (1987). *Middle atmosphere dynamics*. Academic Press.

Baldwin, M. P., Gray, L. J., Dunkerton, T. J., Hamilton, K., Haynes, P. H., Randel, W. J., et al. (2001). The quasi-biennial oscillation. *Reviews Of Geophysics*, *39*, 179–229. https://doi.org/10.1029/1999RG000073

Boccara, G., Hertzog, A., Vincent, R. A., & Vial, F. (2008). Estimation of Gravity wave momentum flux and phase speeds from quasi-lagrangian stratospheric balloon flights. Part I: Theory and simulations. *Journal of the Atmospheric Sciences*, *65*, 3042–3055. https://doi.org/10.1175/2008JAS2709.1

Butchart, N., Anstey, J. A., Hamilton, K., Osprey, S., McLandress, C., Bushell, A. C., et al. (2018). Overview of experiment design and comparison of models participating in phase 1 of the SPARC Quasi-Biennial Oscillation initiative (QBOi). *Geoscientific Model Development*, *11*, 1009–1032. https://doi.org/10.5194/gmd-11-1009-2018

Dhaka, S. K., Bhatnagar, R., Shibagaki, Y., Hashiguchi, H., Fukao, S., Kozu, T., & Panwar, V. (2011). Characteristics of gravity waves generated in a convective and a non-convective environment revealed from hourly radiosonde observation under CPEA-II campaign. *Annales Geophysicae*, *29*(12), 2259–2276. https://doi.org/10.5194/angeo-29-2259-2011

Dinh, T., Podglajen, A., Hertzog, A., Legras, B., & Plougonven, R. (2016). Effect of gravity wave temperature fluctuations on homogeneous ice nucleation in the tropical tropopause layer. *Atmospheric Chemistry and Physics*, *16*, 35–46. https://doi.org/10.5194/acp-16-35-2016

Dunkerton, T. J., & Dunkerton, T. J. (1997). The role of gravity waves in the quasi-biennial oscillation. *Journal of Geophysical Research*, *102*, 26053–26076. https://doi.org/10.1029/96JD02999

Ern, M., Ploeger, F., Preusse, P., Gille, J. C., Gray, L. J., Kalisch, S., et al. (2014). Interaction of gravity waves with the QBO: A satellite perspective. *Journal of Geophysical Research: Atmospheres*, *119*, 2329–2355. https://doi.org/10.1002/2013jd020731

Ern, M., & Preusse, P. (2012). Gravity wave momentum flux spectra observed from satellite in the summertime subtropics: Implications for global modeling. *Geophysical Research Letters*, *39*(15). https://doi.org/10.1029/2012gl052659

Ern, M., Preusse, P., Alexander, M. J., & Warner, C. D. (2004). Absolute values of gravity wave momentum flux derived from satellite data. *Journal of Geophysical Research*, *109*. https://doi.org/10.1029/2004jd004752

Journal of Geophysical Research: Atmospheres 10.1029/2021JD035165

Ern, M., Preusse, P., Gille, J. C., Hepplewhite, C. L., Mlynczak, M. G., Russell, J. M., & Riese, M. (2011). Implications for atmospheric dynamics derived from global observations of gravity wave momentum flux in stratosphere and mesosphere. *Journal of Geophysical Research*, *116*. https://doi.org/10.1029/2011jd015821

Ern, M., Preusse, P., Krebsbach, M., Mlynczak, M. G., & Russell, J. M. (2008). Equatorial wave analysis from SABER and ECMWF temperatures. *Atmospheric Chemistry and Physics*, *8*, 845–869. https://doi.org/10.5194/acp-8-845-2008

Fritts, D. C. (1993). Gravity wave sources, source variability and lower and middle atmosphere effects. In E. V. Thrane, T. A. Blix, & D. C. Fritts (Eds.), *Coupling processes in the lower and middle atmosphere* (pp. 191–208). Springer Netherland. https://doi.org/10.1007/978-94-011-1594-0_13

Fritts, D. C., & Alexander, M. J. (2003). Gravity wave dynamics and effects in the middle atmosphere. *Reviews of Geophysics*, *41*(1), 1003. https://doi.org/10.1029/2001RG000106

Fueglistaler, S., & Baker, M. B. (2006). A modeling study of the impact of cirrus clouds on the moisture budget of the upper troposphere. *Atmospheric Chemistry and Physics*, *6*, 1425–1434. https://doi.org/10.5194/acp-6-1425-2006

Haase, J., Alexander, M. J., Hertzog, A., Kalnajs, L., Deshler, T., Davis, S., et al. (2018). Around the world in 84 days. *Eos*, *99*. https://doi.org/10.1029/2018eo091907

Hertzog, A., Alexander, M. J., & Plougonven, R. (2012). On the intermittency of gravity wave momentum flux in the stratosphere. *Journal of the Atmospheric Sciences*, *69*, 3433–3448. https://doi.org/10.1175/JAS-D-12-09.1

Hertzog, A., Basdevant, C., Vial, F., & Mechoso, C. R. (2004). The accuracy of stratospheric analyses in the northern hemisphere inferred from long-duration balloon flights. *The Quarterly Journal of the Royal Meteorological Society*, *130*, 607–626. https://doi.org/10.1256/qj.03.76

Hertzog, A., Boccara, G., Vincent, R. A., Vial, F., & Cocquerez, P. (2008). Estimation of Gravity wave momentum flux and phase speeds from quasi-lagrangian stratospheric balloon flights. Part II: Results from the Vorcore campaign in Antarctica. *Journal of the Atmospheric Sciences*, *65*(10), 3056–3070. https://doi.org/10.1175/2008JAS2710.1

Hertzog, A., Cocquerez, P., Guilbon, R., Valdivia, J.-N., Venel, S., Basdevant, C., et al. (2007). Stratéole/Vorcore—Long-duration, superpressure balloons to study the Antarctic lower stratosphere during the 2005 winter. *Journal of Atmospheric and Oceanic Technology*, *24*, 2048–2061. https://doi.org/10.1175/2007JTECHA948.1

Hertzog, A., & Vial, F. (2001). A study of the dynamics of the equatorial lower stratosphere by use of ultra-long-duration balloons: 2. Gravity waves. *Journal of Geophysical Research*, *106*, 22745–22761. https://doi.org/10.1029/2000JD000242

Holt, L. A., Lott, F., Garcia, R. R., Kiladis, G. N., Cheng, Y., Anstey, J. A., et al. (2020). An evaluation of tropical waves and wave forcing of the QBO in the QBOi models. *Quarterly Journal of the Royal Meteorological Society*, 1–27. https://doi.org/10.1002/qj.3827

Holton, J. R., Haynes, P. H., McIntyre, M. E., Douglass, A. R., Rood, R. B., & Pfister, L. (1995). Stratosphere-troposphere exchange. *Reviews of Geophysics*, *33*, 403–439. https://doi.org/10.1029/95RG02097

Janowiak, J., Joyce, B., & Xie, P. (2017). NCEP/CPC L3 half hourly 4km global (60S - 60N) merged IR V1. In A. Savtchenko, & M. D. Greenbelt (Eds.), *Goddard Earth sciences data and information services center (GES DISC)*. (Accessed 2020).

Jensen, E. J., Pfister, L., Bui, T.-P., Lawson, P., & Baumgardner, D. (2010). Ice nucleation and cloud microphysical properties in tropical tropopause layer cirrus. *Atmospheric Chemistry and Physics*, *10*, 1369–1384. https://doi.org/10.5194/acp-10-1369-2010

Jensen, E. J., Pfister, L., Jordan, D. E., Fahey, D. W., Newman, P. A., Thornberry, T., et al. (2013). The NASA Airborne Tropical TRopopause EXperiment (ATTREX). *SPARC Newsletter*, *41*, 15–24.

Jensen, E. J., Ueyama, R., Pfister, L., Bui, T. V., Alexander, M. J., Podglajen, A., et al. (2016). High-frequency gravity waves and homogeneous ice nucleation in tropical tropopause layer cirrus. *Geophysical Research Letters*, *43*, 6629–6635. https://doi.org/10.1002/2016GL069426

Jewtoukoff, V., Plougonven, R., & Hertzog, A. (2013). Gravity waves generated by deep tropical convection: Estimates from balloon observations and mesoscale simulations. *Journal of Geophysical Research*, *118*, 9690–9707. https://doi.org/10.1002/jgrd.50781

Karoly, D. J., Roff, G. L., & Reeder, M. J. (1996). Gravity wave activity associated with tropical convection detected in TOGA COARE Sounding data. *Geophysical Research Letters*, *23*, 261–264. https://doi.org/10.1029/96gl00023

Kawatani, Y., Watanabe, S., Sato, K., Dunkerton, T. J., Miyahara, S., & Takahashi, M. (2010). The roles of equatorial trapped waves and internal inertia–gravity waves in driving the quasi-biennial oscillation. Part I: Zonal mean wave forcing. *Journal of the Atmospheric Sciences*, *67*, 963–980. https://doi.org/10.1175/2009JAS3222.1

Kim, J.-E., & Alexander, M. J. (2015). Direct impacts of waves on tropical cold point tropopause temperature. *Geophysical Research Letters*, *42*, 1584–1592. https://doi.org/10.1002/2014GL062737

Lane, T. P., & Moncrieff, M. W. (2008). Stratospheric gravity waves generated by multiscale tropical convection. *Journal of the Atmospheric Sciences*, *65*, 2598–2614. https://doi.org/10.1175/2007JAS2601.1

Lane, T. P., Reeder, M. J., & Clark, T. L. (2001). Numerical Modeling of Gravity Wave Generation by Deep Tropical Convection. *Journal of the Atmospheric Sciences*, *58*, 1249–1274. https://doi.org/10.1175/1520-0469(2001)058<1249:nmogwg>2.0.co;2

Lane, T. P., & Sharman, R. D. (2006). Gravity wave breaking, secondary wave generation, and mixing above deep convection in a three-dimensional cloud model. *Geophysical Research Letters*, *33*. https://doi.org/10.1029/2006GL027988

Lane, T. P., & Zhang, F. (2011). Coupling between gravity waves and tropical convection at mesoscales. *Journal of the Atmospheric Sciences*, *68*, 2582–2598. https://doi.org/10.1175/2011JAS3577.1

Larsen, M. F., Swartz, W. E., & Woodman, R. F. (1982). Gravity-wave generation by thunderstorms observed with a vertically-pointing 430 MHz radar. *Geophysical Research Letters*, *9*, 571–574. https://doi.org/10.1029/GL009i005p00571

Liu, C., & Zipser, E. J. (2005). Global distribution of convection penetrating the tropical tropopause. *Journal of Geophysical Research*, *110*. https://doi.org/10.1029/2005JD006063

Lu, B., & Ren, H.-L. (2020). What caused the extreme indian ocean dipole event in 2019? *Geophysical Research Letters*, *47*(11). https://doi.org/10.1029/2020gl087768

Madden, R. A., & Julian, P. R. (1971). Detection of a 40–50 Day Oscillation in the Zonal Wind in the Tropical Pacific. *Journal of the Atmospheric Sciences*, *28*, 702–708. https://doi.org/10.1175/1520-0469(1971)028<0702:doadoi>2.0.co;2

Madden, R. A., & Julian, P. R. (1972). Description of global-scale circulation cells in the Tropics with a 40–50 day period. *Journal of the Atmospheric Sciences*, *29*, 1109–1123. https://doi.org/10.1175/1520-0469(1972)029<1109:dogscc>2.0.co;2

Matsuno, T. (1966). Quasi-geostrophic motions in the equatorial area. *Journal of the Meteorological Society of Japan Ser II*, *44*, 25–43. https://doi.org/10.2151/jmsj1965.44.1_25

Pahlavan, H. A., Wallace, J. M., Fu, Q., & Kiladis, G. N. (2021). Revisiting the Quasi-biennial oscillation as seen in ERA5. Part II: Evaluation of waves and wave forcing. *Journal of the Atmospheric Sciences*, *78*, 693–707. https://doi.org/10.1175/jas-d-20-0249.1

Pfister, L., Scott, S., Loewenstein, M., Bowen, S., & Legg, M. (1993). Mesoscale disturbances in the tropical stratosphere excited by convection: observations and effects on the stratospheric momentum budget. *Journal of the Atmospheric Sciences*, *50*, 1058–1075. https://doi.org/10.1175/1520-0469(1993)050<1058:mditts>2.0.co;2

AGU ADVANCING EARTH AND SPACE SCIENCE

Journal of Geophysical Research: Atmospheres 10.1029/2021JD035165

Piani, C., Durran, D., Alexander, M. J., & Holton, J. R. (2000). A numerical study of three-dimensional gravity waves triggered by deep tropical convection and their role in the dynamics of the QBO. *Journal of the Atmospheric Sciences*, *57*, 3689–3702. https://doi.org/10.1175/1520-0469(2000)057<3689:ansotd>2.0.co;2

Plougonven, R., Hertzog, A., & Guez, L. (2013). Gravity waves over Antarctica and the Southern Ocean: Consistent momentum fluxes in mesoscale simulations and stratospheric balloon observations. *Quarterly Journal of the Royal Meteorological Society*, *139*, 101–118. https://doi.org/10.1002/qj.1965

Podglajen, A., Hertzog, A., Plougonven, R., & Legras, B. (2016). Lagrangian temperature and vertical velocity fluctuations due to gravity waves in the lower stratosphere. *Geophysical Research Letters*, *43*, 3543–3553. https://doi.org/10.1002/2016GL068148

Podglajen, A., Hertzog, A., Plougonven, R., & Legras, B. (2020). Lagrangian gravity wave spectra in the lower stratosphere of current (re) analyses. *Atmospheric Chemistry and Physics*, *20*, 9331–9350. https://doi.org/10.5194/acp-20-9331-2020

Podglajen, A., Hertzog, A., Plougonven, R., & Žagar, N. (2014). Assessment of the accuracy of (re)analyses in the equatorial lower stratosphere. *Journal of Geophysical Research*, *119*, 11166–11188. https://doi.org/10.1002/2014JD021849

Podglajen, A., Plougonven, R., Hertzog, A., & Jensen, E. (2018). Impact of gravity waves on the motion and distribution of atmospheric ice particles. *Atmospheric Chemistry and Physics*, *18*, 10799–10823. https://doi.org/10.5194/acp-18-10799-2018

Preusse, P., Eckermann, S. D., & Ern, M. (2008). Transparency of the atmosphere to short horizontal wavelength gravity waves. *Journal of Geophysical Research*, *113*, D24104. https://doi.org/10.1029/2007JD009682

Randel, W. J., Wu, F., & Podglajen, A. (2021). Equatorial Waves, diurnal tides and small-scale thermal variability in the tropical lower stratosphere from COSMIC-2 radio occultation. *Journal of Geophysical Research*, *126*. https://doi.org/10.1029/2020jd033969

Richter, J. H., Butchart, N., Kawatani, Y., Bushell, A. C., Holt, L., Serva, F., et al. (2020). Response of the Quasi-Biennial Oscillation to a warming climate in global climate models. *The Quarterly Journal of the Royal Meteorological Society*, 1–29. https://doi.org/10.1002/qj.3749

Saji, N. H., Goswami, B. N., Vinayachandran, P. N., & Yamagata, T. (1999). A dipole mode in the tropical Indian Ocean. *Nature*, *401*, 360–363. https://doi.org/10.1038/43854

Schirber, S., Manzini, E., Krismer, T., & Giorgetta, M. (2015). The quasi-biennial oscillation in a warmer climate: Sensitivity to different gravity wave parameterizations. *Climate Dynamics*, *45*, 825–836. https://doi.org/10.1007/s00382-014-2314-2

Solomon, S., Rosenlof, K. H., Portmann, R. W., Daniel, J. S., Davis, S. M., Sanford, T. J., & Plattner, G.-K. (2010). Contributions of stratospheric water vapor to decadal changes in the rate of global warming. *Science*, *327*, 1219–1223. https://doi.org/10.1126/science.1182488

Stephan, C., & Alexander, M. J. (2015). Realistic simulations of atmospheric gravity waves over the continental U.S. using precipitation radar data. *Journal of Advances in Modeling Earth Systems*, *7*(2), 823–835. https://doi.org/10.1002/2014ms000396

Torrence, C., & Compo, G. P. (1998). A practical guide to wavelet analysis. *Bulletin of the American Meteorological Society*, *79*, 61–78. https://doi.org/10.1175/1520-0477(1998)079<0061:apgtwa>2.0.co;2

Vial, F., Hertzog, A., Mechoso, C. R., Basdevant, C., Cocquerez, P., Dubourg, V., & Nouel, F. (2001). A study of the dynamics of the equatorial lower stratosphere by use of ultra-long-duration balloons: 1. Planetary scales. *Journal of Geophysical Research*, *106*, 22725–22743. https://doi.org/10.1029/2000JD000241

Vincent, R. A., & Alexander, M. J. (2020). Observational studies of short vertical wavelength gravity waves and interaction with QBO winds. *Journal of Geophysical Research*, *27*. https://doi.org/10.1029/2020JD032779

Vincent, R. A., & Hertzog, A. (2014). The response of superpressure balloons to gravity wave motions. *Atmospheric Measurement Techniques*, *7*, 1043–1055. https://doi.org/10.5194/amt-7-1043-2014

Vincent, R. A., Hertzog, A., Boccara, G., & Vial, F. (2007). Quasi-Lagrangian superpressure balloon measurements of gravity-wave momentum fluxes in the polar stratosphere of both hemispheres. *Geophysical Research Letters*, *34*. https://doi.org/10.1029/2007GL031072

Webster, P. J., Moore, A. M., Loschnigg, J. P., & Leben, R. R. (1999). Coupled ocean–atmosphere dynamics in the indian ocean during 1997–98. *Nature*, *401*, 356–360. https://doi.org/10.1038/43848

Wright, C. J., Osprey, S. M., & Gille, J. C. (2013). Global observations of gravity wave intermittency and its impact on the observed momentum flux morphology. *Journal of Geophysical Research*, *118*(10), 10980–10993. https://doi.org/10.1002/jgrd.50869

Zhang, G. J., & Mu, M. (2005). Simulation of the madden–julian oscillation in the ncar ccm3 using a revised zhang–mcfarlane convection parameterization scheme. *Journal of Climate*, *18*, 4046–4064. https://doi.org/10.1175/JCLI3508.1

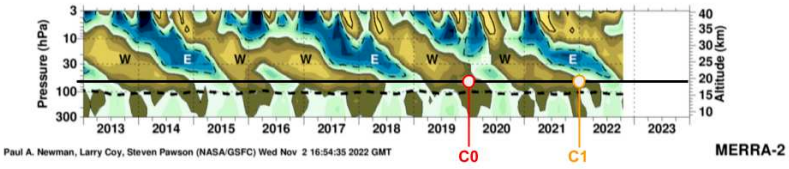

Figure 2.7: Zonal winds in the lower Stratosphere, representing the phases of the QBO. The wind conditions during the campaigns are spotted with a red circle for C0 and orange for C1.

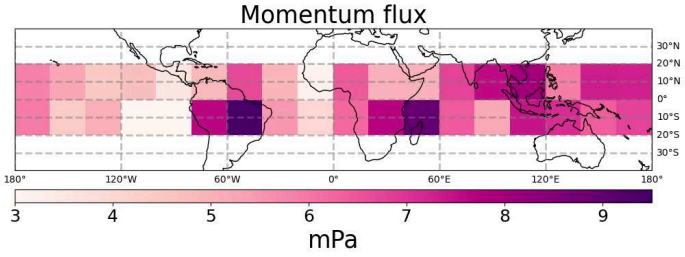

(a) 2019 : Campaign C0.

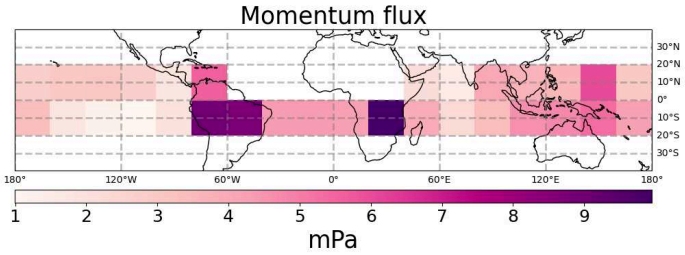

(b) 2021 : Campaign C1.

Figure 2.8: Map of the momentum fluxes for gravity waves with periods between [15min-1day].

2.4 Change in the momentum fluxes distribution between C0 and C1.

We now investigate the interannual variability of the measured momentum fluxes, between both Stratéole-2 first campaigns. The stratospheric dynamics variability in the tropics is mainly driven by the QBO. C0 and C1 campaigns were in the Eastern phase of the Quasi Biennial Oscillation, but closer to the transition to the western phase in winter 2021, as shown in Figure 2.7. The balloons all drifted eastward, but the zonal wind was weaker in 2021 ($\sim$ 5 m/s) than in 2019 ($\sim$ 5.5 m/s). It is expected that this slight phase change of the QBO will have a minor impact on the momentum flux measurements, a slight decrease in winds having a small impact on wave propagation. On the other hand, TTL conditions are also impacted by the tropospheric circulation which changes might explain differences in the measurements, as we highlighted the link between convection and gravity waves in this chapter.

Figure 2.8 displays the measured momentum fluxes averaged in bins of 20° of longitude, for the two Stratéole-2 campaigns C0 and C1. We have decided to distinguish the positive and

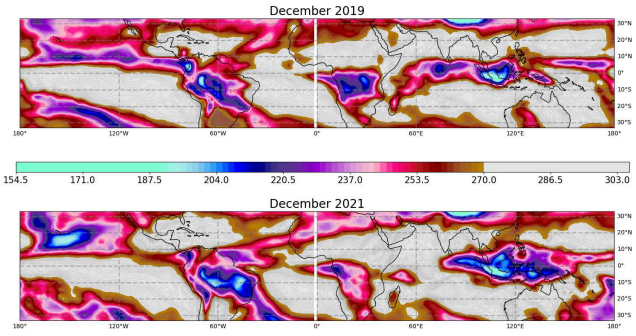

(a) Monthly averaged maps of brightness temperature in the long wave radiation at the top of atmosphere.

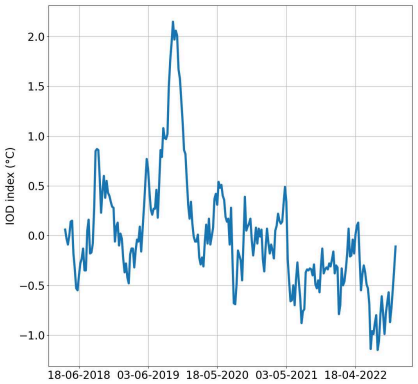

(b) Indian Ocean Dipole (IOD) index.

Figure 2.9: Evolution of convection between 2019 and 2021.

negative latitudes as C1 did not have balloons crossing the Atlantic ocean in the Northern hemisphere. The difference of sampling between the two campaigns can explain some discrepancy between the observations. Overall, the momentum fluxes are weaker during the second campaign, which can be linked to a filtering of the waves from the campaign closer to the QBO transition with weaker winds. C0 measures a mean momentum flux of $\sim$ 6 mPa, C1 $\sim$ 3.6 mPa, which gives a mean inter-annual variability of 2.4 mPa. Both maps show a clear distinction between momentum fluxes over the continents/oceans. Momentum fluxes around Africa and southern America have the same value of $\sim$ 9 mPa. The maritime continent also has relatively higher momentum flux, but with values lower for the second campaign. Differences stand out more over the oceans. First, during C0 they were varying over the Indian Ocean whereas C1 conversely displays a more stable behavior. The same difference is found for the eastern Pacific, as well as the Atlantic (note here that only one balloon flew there during C1, this difference thus can be mainly due to the sampling). Note that the momentum fluxes are very intermittent and the mean can be influenced by relatively few, very large values.

To provide hints that could explain the differences, we investigate how convection has changed between the two campaigns. We use brightness temperature monthly maps as a proxy for convective activity. December maps (Figure 2.9a) display a clear difference between 2019 and 2021 in the Indian Ocean, with a positive IOD phase in 2019, resulting in an increased convection west of India caused by weakening easterly winds along the equator, and migration of warm waters to Africa. This observation can be confirmed by the evolution of the IOD index (figure 2.9b), provided by the Australian Bureau of Meteorology. A particularly positive IOD index was recorded in 2019, and slightly negative in 2021. On the other hand, the negative phase of the IOD is associated with the increase of deep convection towards the maritime continent, which can be seen on the brightness temperature maps. For both campaigns, a small meridional gradient is found with stronger values in the Southern hemisphere ($\sim$ +12% C0, $\sim$ +30% C1). This is clearly correlated with the meridional gradient of convection, for example above the continents. Last, the similarities tend to show the robustness of our measurements and calculations.

Chapter 3

Impact of gravity waves on ice crystals at the Tropical Tropopause Layer

Sommaire

3.1 Theory of ice nucleation and growth

Phase change Nucleation is the first step in the the formation of a new phase, here from a metastable supersaturated vapor phase. The degree of supersaturation of a solute is measured by the saturation ratio S, written here as S_i as we are interested in the phase change between water vapor and ice:

$$S_i = \frac{p_v}{p_{sat}(T)} = \frac{N}{N_{sat}(T)} \tag{3.1}$$

with p_v the partial pressure of water vapor, p_{sat} the saturation vapor pressure with respect to a flat surface of ice, in equilibrium with the solid phase at temperature T. N and N_{sat} are the corresponding number of molecules of water vapor. Nucleation of a stable phase does not occur at $Si = 1$. A snapshot of the physical situation would show molecules of the solute co-existing independently, whereas in a supersaturated environment ($S_i > 1$), the increase of molecules clusters might be large enough to start a new phase. In terms of chemical potential, the saturation is linked to the difference of chemical potential μ between the two phases (vapor $_v$ and solid $_s$) as:

$$\mu_v - \mu_s = k_b T \ln(S_i) \tag{3.2}$$

with k_b the Boltzmann constant. For $S_i < 1$, $\mu_v - \mu_s < 0$. The vapor is stable and will not freeze. For $S_i > 1$, $\mu_v > \mu_s$, and the new phase will grow at the vapor's expense as a system tends to its lowest chemical potential. To understand how this phase change occurs in terms of energy, the principle of nucleation is that the phase change of a body involves the creation of a surface between its two phases. Therefore, the Gibbs free energy of formation must be greater than the surface free energy (thus also called free energy barrier) to allow the new phase to be created. The creation of a new interface between gas and solid leads to a free energy change, proportional to the surface tension of the solution and the surface of the new phase molecules cluster. For any nucleus of the new phase, the free energy linked to the transfer of molecules from the vapor to nuclei is the sum of a bulk term that is proportional to the volume of the nucleus (from the formation of the condensed phase), and a positive term from the formation of a new interface, that is proportional to its surface area:

$$\Delta G = 4\pi\sigma r^2 - \frac{4\pi}{3}\frac{k_b T \ln(S_i)}{v_s} r^3 \tag{3.3}$$

with v_s the molar volume of solid phase. As r^3 changes faster than r^2, the surface term will be dominant for smaller radius and r^3 for larger radius. Therefore ΔG will go through a local maximum for some intermediate value of r. In a supersaturated environment, the free energy will increase with r until the bulk free energy decrease exceeds the surface free energy increase. Thus, there is a critical ΔG from which the embryo will grow spontaneously, whereas smaller size nuclei will dissolve. In other words, nuclei must reach a critical radius to create a new stable phase:

$$\begin{aligned} \frac{\mathrm{d}\Delta G}{\mathrm{d}r} &= 0 \\ r_{crit} &= \frac{2\sigma v_s}{k_b T \ln(S_i)} \end{aligned} \tag{3.4}$$

The critical radius is inversely proportional to the evolution of S_i. An increase of the saturation ratio lowers the critical radius. The free energy barrier height that needs to be reached to create a stable new phase is calculated by combining the critical radius and the Gibbs free energy to create a new interface. It comes:

$$\begin{aligned} \Delta G_{crit} &= \frac{4\pi}{3}\sigma r_{crit}^2 \\ &= \frac{16\pi}{3}\frac{v_s^2\sigma^3}{(k_b T \ln S_i)^2} \end{aligned} \tag{3.5}$$

This equation shows that an increase of S_i also decreases the free energy barrier. This makes it easier for a new phase to be created.

There are two different types of nucleation, respectively called homogeneous and heterogeneous. The first is homogeneous throughout the system, while the latter corresponds to the process where the probability of nucleating is much higher around some foreign bodies than in other parts of the system. Indeed, the latter includes solid cores from the beginning (e.g ice coming from the plumes, or transported aerosol dust), the solid surfaces of which decrease the free barrier energy necessary for the formation of the new phase. This process lowers the activation threshold of the phase change and makes nucleation possible at lower supersaturation. It explains why crystals can be formed at relative humidity with respect to ice only slightly over 100%.

Nucleation rate The classical theory of nucleation describes with statistics and thermodynamics the evolution of clusters of monomers from a kinetic viewpoint. Molecules are followed as they collide, forming or leaving bigger clusters. In this representation, nucleation is a kinetic non equilibrium process dependent on the characteristics of the solution (i.e aerosol) such as the molecular diameter and therefore the chemical composition of the aerosols. Koop et al. (2000) described the theory of homogeneous nucleation as dependent only on the water activity (a_w) of the solution and not on the nature of the solute, which usually affects the properties of water. It is based on the assumption of thermodynamical equilibrium between the condensed phase and gas. Water activity is the ratio between the water vapour pressure in equilibrium with the solution and with a pure water liquid solution under the same conditions. It is thus equal to 1 for pure liquid bulk water. Most of atmospheric aerosols are in equilibrium with water vapour below saturation, in which case a_w is equivalent to the relative humidity, RH. In this case, the activity of a solution in equilibrium with ice is not dependant on the solute nature, it is only a function of pressure and temperature:

$$\begin{aligned} a_w^i(T,p) &= \exp\left(\frac{\mu_w^i(T,p) - \mu_w^0(T,p)}{RT}\right) \\ \mu_w^i(T,p) - \mu_w^0(T,p) &= 210368 + 131.438\ T - 3.32373 \times 10^6\ T^{-1} - 41729.1 \ln(T) \end{aligned} \tag{3.6}$$

With $\mu_w^i(T,p)$ and $\mu_w^0(T,p)$ the temperature and pressure dependent chemical potentials of water in pure ice and pure liquid water, respectively, in J/mol. Koop et al. (2000) find that ice nucleation is entirely driven by the difference of activity between the solution in equilibrium

with ice and pure water (water activity criterion). As a result the activation energy ΔG_{crit} and the interface energy depends only on water activity but not on the nature of solute. This contrasts with classical nucleation theory, in which the nucleation process is driven only in part by activity (in the saturation ratio) but is also determined by how the solute nature affects the ice/solution interface energy, as well as the diffusion activation energy for a water molecule to cross the solution/ice interface. This discrepancy is fixed when the latter only depends on water activity and not the nature of the solute. This means finding plausible dependencies of ΔG and interface energy with the water activity. It gives the homogeneous nucleation rate ω, which is the amount of new nuclei created and is only dependent on water activity and pressure for a given volume (stochastic process):

$$\begin{aligned} \omega &= JV(/s) \\ log(J) &= -906.7 + 8502\Delta a_w - 26924(\Delta a_w)^2 + 29180(\Delta a_w)^3 \end{aligned} \tag{3.7}$$

with J the nucleation rate coefficient and $\Delta a_w = a_w - a_w^i$ the difference of activity in water solution and activity of water in equilibrium with ice. Koop (2015) found this relation proper for most atmospheric situations, in the limit of very strong updrafts or violent atmospheric wave activity. Note that this equilibrium hypothesis, in which RH_w is equivalent to $a_{w,eq}$ is not established at cold temperatures, nonetheless the representation of homogeneous nucleation as dependant on water activity can describe some non equilibrium cases (Knopf et al., 2018; Murata and Tanaka, 2013). Another limitation of the theory is brought by the lack of knowledge of water vapor saturation pressure at low temperatures ($<$ 230 K). Properties of supercooled water are not fully understood (Koop, 2004) and parameterizations as well as experiments to determine p_{sat} deviate significantly (Murphy and Koop, 2005; Nachbar et al., 2019).
Koop et al. (2000) representation of homogeneous ice nucleation is today implemented in most models simulating cirrus clouds. It is relying on p_{sat} and $a_{w,eq}$ which both have several descriptions in literature. Baumgartner et al. (2022) showed that the difference in computation of these parameters do not have a strong effect on the number of ice crystals nucleated. However, the ice onset humidities, influenced by the volume of solution particles, are sensitive to the choices for $a_{w,eq}$ and p_{sat}, especially at cold temperatures. This is important for the representation of tropical cirrus clouds, as ice onset humidity determines the appearance of cirrus clouds but also the amount of water vapor transported into the stratosphere.

Growth of ice crystals The growth of ice crystals occurs by two processes, deposition of H_2O molecules and aggregation of ice crystals by collision. Our model neglects the ice crystal aggregation, therefore diffusional growth and sedimentation are the only microphysical processes active and described here. Vapor deposition can be depicted into 3 steps, the first being the adsorption of a vapor molecule. The molecule is "sticking" to the surface by a weak bonding. This is followed by the surface diffusion, in which the adsorbed molecule is randomly displaced. Last, the molecule is incorporated into the lattice. The efficiency of incorporation into the lattice is embodied by the deposition coefficient α, which represents the fraction of particles colliding with the ice surface that effectively get incorporated into the ice crystal

lattice.

$$\alpha = \frac{\text{actual growth rate}}{\text{maximum growth rate}} \tag{3.8}$$

Its value is not well known, and usually varies between 0.001 and 1. Experimental studies were not able to constrain it well so far (Magee et al., 2006; Skrotzki et al., 2013). However, Kärcher and Lohmann (2002), Kay and Wood (2008) showed that observations are hard to reconcile with $\alpha \leq 0.5$. We use here $\alpha = 1$.

For crystals with a spherical shape, the growth rate of the radius r is given by Pruppacher and Klett (1978). It is assumed molecule by molecule, and does not take into account collisions of clusters of molecules

$$\frac{\mathrm{d}r}{\mathrm{d}t} = \frac{\gamma'(r,T,\alpha)}{r}(S_i - 1) \tag{3.9}$$

With γ' the growth factor, dependant on the crystal radius, the temperature and α as:

$$\gamma' = \frac{1}{\rho_{ice}\left(\frac{R_v T}{p_{sat}(T) D'_v(r,T,\alpha)} + \frac{L_s}{T k'_a(r,T)}\left(\frac{L_s}{T R_v} - 1\right)\right)} \tag{3.10}$$

where $\rho_{ice} = 918$ kg/m^3 is the density of ice, D'_v is the modified diffusivity of water vapor in air, k'_a is the modified thermal conductivity of air, p_{sat} is the saturation water vapor pressure, $R_v = 462$ J/K/kg is the gas constant for water vapor, $L_s = 2.844 \times 10^6$ J/kg is the latent heat of sublimation of ice. The modified diffusivity D'_v is the product of the diffusivity and the ventilation coefficient for mass transfer $f_{d,v}(r,T)$ for large ice crystals, and ventilation coefficient for thermal diffusion for small ice crystals $f_{d,k}(r,T)$. Similarly, the modified thermal conductivity is the product of thermal conductivity and $f_{k,v}(r,T)$ and $f_{k,k}(r,T)$ such as:

$$D'_v = D_v(T) f_{d,v}(r,T) f_{d,v}(r,T)$$
$$k'_a = k_a(T) f_{k,v}(r,T) f_{k,v}(r,T)$$

with the coefficients derived from Hall and Pruppacher (1976), eq. 16 and 17. For intermediate crystal sizes ($r \approx 5$ to 50 μm) and large deposition coefficients ($\alpha \geq 0.5$), $D'_v \approx D_v$ and $k'_a \approx k_a$. The growth coefficients can be then simply a function of temperature. We assume here that the temperature of these clusters of molecules are equal to the one of the background air; but there is actually an evolution of heat during the phase change (here from vapor to ice). This assumption is true if the time scale of phase change is longer than the one required for an equilibrium between new phase and background gas by particles collisions.

3.1.1 Example of the slow ascent of an air parcel

Let's take the example of an ascending air parcel. A first key parameter to understand its evolution is the cooling rate for an adiabatic transformation, connecting the temperature of the air parcel to its vertical speed:

$$\frac{\mathrm{d}T}{\mathrm{d}t} = -\frac{g}{c_p} w\,, \tag{3.11}$$

with w the vertical speed, g the gravitational acceleration, c_p the specific heat capacity of air. The second and most important parameter to understand when nucleation occurs is the

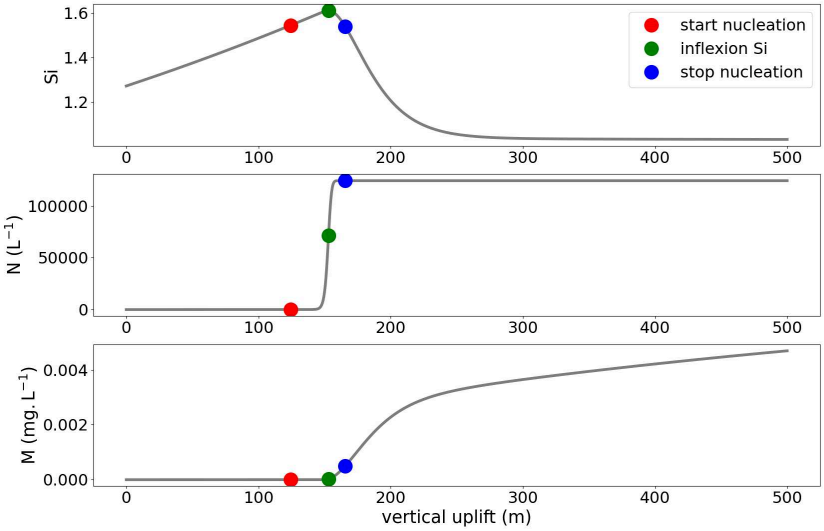

Figure 3.1: Evolution of relative humidity with respect to ice /100% (upper panel), ice crystals concentration (middle panel) and ice mass (lower panel) for one air parcel lifted adiabatically.

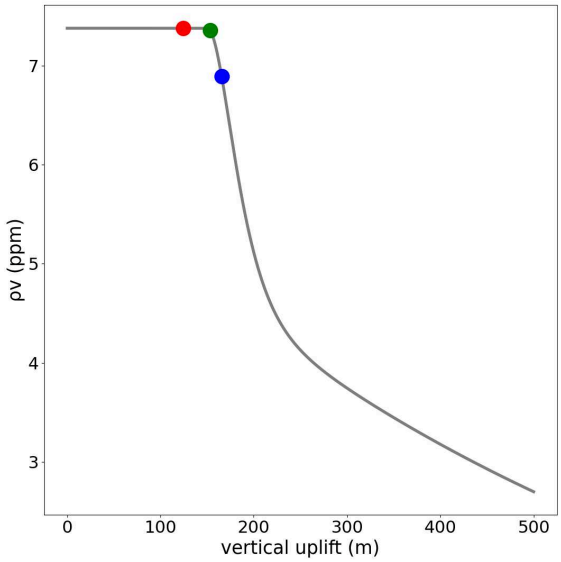

Figure 3.2: Evolution of the water vapor mass mixing ratio of an air parcel lifted adiabatically.

relative humidity with respect to ice RH_i ($=S_i \times 100\%$), which depends on the pressure, temperature as well as water vapor mixing ratio of the air parcel:

$$\frac{\mathrm{d}RH_i}{\mathrm{d}t} = -\frac{RH_i}{T}\left(\frac{L}{R_v T} - \frac{c_p}{R}\right)\frac{\mathrm{d}T}{\mathrm{d}t} + \partial_{\rho_v} RH_i \partial_t \rho_v \,. \tag{3.12}$$

With L the latent heat, R_v and R respectively the gas constant for water vapor and dry air. As described previously, without a preexisting nucleus, the gas phase keeps cooling while the air parcel is lifted, without nucleation. Using the Clausius Clapeyron formula for p_{sat} and

differentiating with respect to time, it yields:

$$\begin{aligned} \frac{\mathrm{d}\ln(p_{sat})}{\mathrm{d}\ln(T)} &= \frac{L_s M_w}{RT} \\ \frac{\mathrm{d}S_i}{\mathrm{d}t} &= \left(\frac{L_s M_w g}{c_p R T^2} - \frac{Mg}{RT}\right) S_i w \end{aligned} \tag{3.13}$$

with M the molecular mass of air 29.10^{-3} kg/mol, M_w the molecular mass of water, L_s the latent heat of sublimation, R the universal gas constant. p_{sat} is calculated from Goff Gratch's equation in Smithsonian Tables (1984):

$$P_{sat}(T) = 6.1071.10^2 \times (T/273.16)^{3.56654}.10^{(-9.09718\times(\frac{273.16}{T}-1)+0.876793(1-T/273.16))} \tag{3.14}$$

The dependency of ice saturation ratio S_i (or RH_i) with temperature is expressed by the two terms in parenthesis. The positive one is dominant, showing that the relative humidity with respect to ice will increase with a cooling of the air parcel (figure 3.1 upper panel). As the air parcel keeps cooling, it reaches a metastable state called supercooled. Its temperature is lower than the equilibrium temperature at which a flat surface of ice can coexist in equilibrium with the water vapor pressure. As S_i increases, we have seen that the critical radius of nucleation of a new stable solid phase shrinks. Homogeneous nucleation is stochastic, proportional to the volume of the air parcel. There, the probability to nucleate during a time t is relative to the volume and temperature (Koop et al., 2000):

$$P_{nucle} = 1 - \exp(-JVt) \tag{3.15}$$

There is therefore a threshold value of RH_i from which the probability to nucleate will be high enough for ice crystals to be created (figure 3.1, red dot). The formation and growth of the crystals captures the humidity from the air parcel (figure 3.2) and adds a new term in the variation of S_i. It comes (Pruppacher et al., 1998):

$$\frac{dS_i}{dt} = \left(\frac{L_s M_w g}{c_p R T^2} - \frac{Mg}{RT}\right) S_i w - \left(\frac{1}{n_{sat}} + \frac{L_s^2 M_w m_w}{C_p P T M} S_i\right) R_i \tag{3.16}$$

with R_i the freezing/growth term that descries the depletion of water vapor by growing ice crystals (Kärcher and Lohmann, 2002):

$$R_i = \frac{\rho_i}{m_w} \int_{-\infty}^{t} \mathrm{d}t_0 \dot{n}_i(t_0) 4\pi r_i^2(t_0, t) \frac{\mathrm{d}r_i}{\mathrm{d}t}(t_0, t) \tag{3.17}$$

with ρ_i the ice particle mass density, $\dot{n}_i(t_0)\mathrm{d}t_0$ the number density of aerosol particles that freeze for a time $\mathrm{d}t_0$, $r_i(t_0, t)$ the radius of the ice particle that froze and started to grow at time $t{>}t_0$ and $\mathrm{d}r_i/\mathrm{d}t$ its the growth rate. The change of sign of S_i, happens when the deposition is large enough to balance the temperature dependency. It happens when the water vapor mixing ratio term in equation 3.12 is larger than the two first terms of the sum. This inflexion point in the evolution of S_i is indicated by the green dot on figure 3.1. From this moment, S_i decreases, until it becomes lower than a critical value, below which the nucleation stops. The number of ice crystals remains constant thereafter if sedimentation is not taken into account (figure 3.1 middle panel) and the environment is not subsaturated. Crystal growth on the other hand continues as long as the environment is supersaturated. It captures the available

humidity until the air parcel is back to an equilibrium state (figure 3.2, note the change of slope after an ascent of 200m, showing a steady state growth regime). At equilibrium, close to RH_i=1, the evolution in time of ice mass and conversely available water vapor then changes slope and follows a limited growth regime, correlated to the stalling of RH_i (from $\approx$ 250 to 500 m on the figure).
First, one can note the narrow interval of RH_i that allows nucleation on figure 3.1. Nucleation is very sensitive to the activity of the air parcel, with terms involving power 2 and 3 (equation 3.7). As the activity is equivalent to the ice saturation ratio (Koop et al., 2000), a small change in RH_i has a very strong impact on nucleation.
Second, the evolution of ice crystals and RH_i would be different for a mixed phase cloud, with a mix of liquid, solid and gaseous phase of water, as the difference of activity in (3.7) would be different of RH_i. In this case, the nucleation sensitivity to that parameter would be lowered, and RH_i could decrease more without stopping the nucleation. In this configuration, solution droplets could even evaporate before freezing.

In the TTL, the large scale updrafts are generated by two main sources: an ascent that compensates the mean diabatic heating (Fueglistaler et al., 2009) and large scale equatorial waves such as Kelvin waves (Webster, 1972; Thompson et al., 2011) which are usually triggered by convective systems. The first one is responsible for very slow updrafts, around 1 mm/s. For Kelvin waves with periods up to a few days, updrafts are generally around 2 mm/s to 1 cm/s. At large scales, measurements have shown the correlation between cirrus clouds and cold anomalies in this region (Bramberger et al., 2022).
The relative importance of homogeneous and heterogeneous nucleation in the TTL is still debated. Homogeneous nucleation occurs for RH_i>160% whereas heterogeneous nucleation can be found at lower supersaturation values (120-130%) and therefore in warmer environment. In situ and remote measurements inside and outside the clouds have shown that there remains a supersaturation with respect to the ice within cirrus clouds (Krämer et al., 2020). However Krämer et al. (2009), have shown that these a priori paradoxical observations were in fact explained by the very low number of ice crystals observed in the clouds compared to the expected number. Studies showed that the contamination of aqueous aerosols with organics might be a reason explaining the low ice crystal concentration in the TTL (Murray et al., 2010). Note that the precise composition of the particle is less important as long as it contains anorganic material (Koop et al., 2000; Koop, 2004), but measurements (Murphy et al., 1998; Froyd et al., 2009) showed the significant fraction of organic components of tropical aerosols, with organic rich particles being harder to freeze (Cziczo et al., 2004), yet the fraction of organics actually measured is pretty low. So based on measurements, it is unlikely that organics can totally suppress homogeneous nucleation.

3.2 Our 1.5D representation: impact of the sedimentation on ice crystal population

A number of processes, with a wide range of scales, affect the formation and evolution of cirrus clouds. Lagrangian box models have naturally been used (Hoyle et al., 2005), with an

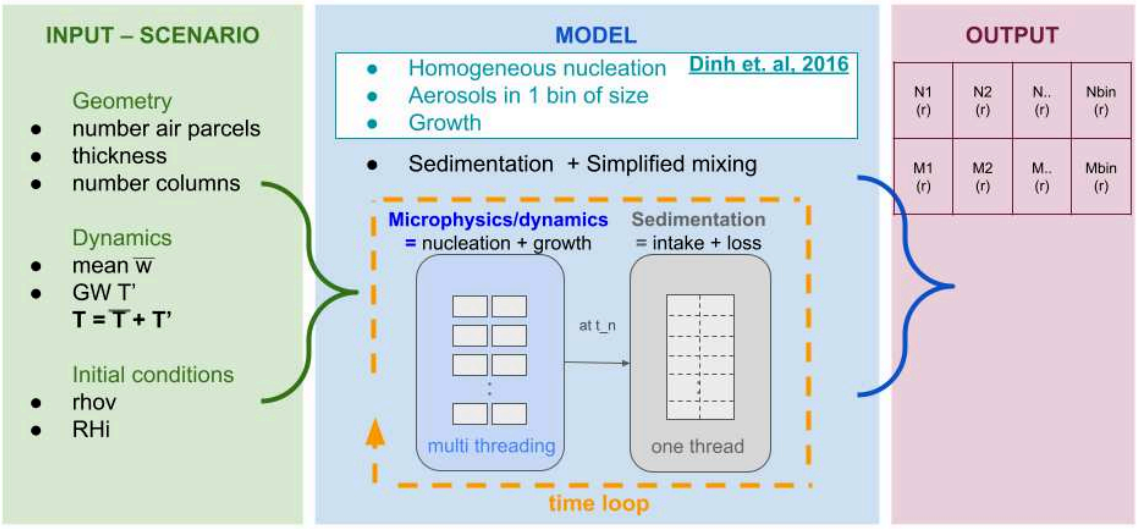

Figure 3.3: Schematics of our model.

advantage being the possibility to resolve the size distribution of ice crystals and compare with in-situ measurements. Microphysical box model simulations with various complexity (Gettelman et al., 2002; Ren et al., 2007) are convenient to indicate a maximum potential ice concentration, but the reduced dimensionality sets a critical limitation when such models are used to infer the drying of air parcels and evolution of cirrus clouds on a longer time scale than nucleation. Other models track the size and height of ice crystals in a curtain model approach (Jensen and Pfister, 2004), giving good results for air parcel dehydration but omitting the effects of shear and mixing. At larger scale, 3D simulations representing crystals formation, growth, sedimentation, aggregation, such as CARMA (Community Aerosol and Radiation Model for Atmospheres) (Toon et al., 1988; Bardeen et al., 2008) can also include the possibility to be combined with global circulation models.

Our approach here is to use a higher resolution model, taking into account simple settings in order to assess the importance and interactions of the different processes involved in determining the population of ice crystals, which sets the cirrus cloud radiative properties and life cycle, as well as the dehydration of air parcels entering the stratosphere. Our model follows the evolution of ice with the number of crystals and ice mass in 36 bins of size, along Lagrangian trajectories. It is represented in figure 3.3. It simulates in-situ cirrus cloud formation from homogeneous ice nucleation in a 1.5D representation, taking into account sedimentation (vertical dimension), as number of studies have shown its leading role in determining cirrus ice concentrations (Spichtinger and Gierens, 2009; Jensen et al., 2012, 2013; Murphy, 2014), as well as a simplified mixing associated with wind shear (horizontal dimension). These allow longer simulations to understand the impact of dynamics at a longer time scale than Dinh et al. (2016).

In more details, our model simulates the microphysical evolution of a grid of air parcels, which geometry is set at the beginning of the simulation. Two numerical blocks interact at each

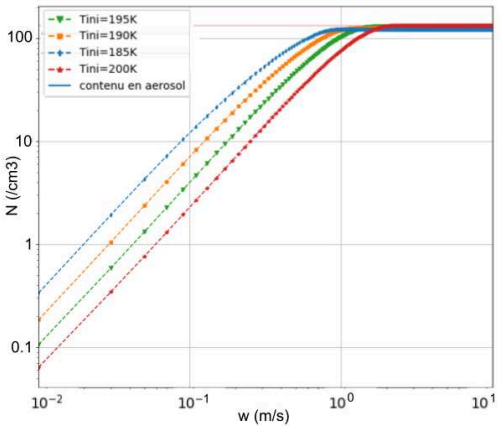

(a) Our simulation of ice crystals production as a function of vertical speed

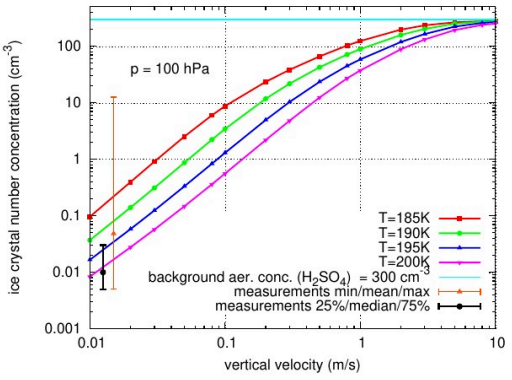

(b) Similar figure from Spichtinger and Krämer (2013) box model.

Figure 3.4: Homogeneously nucleated ice crystals concentration as a function of the updraft speed and initial temperature in our microphysical model and in the box model of Spichtinger and Krämer (2013). Our simulation (left panel) slightly overestimates the ice crystals production, but follows the same power law evolution, limited by the amount of aerosols for the largest vertical speed.

time step: a first one (in blue on the figure) quantifies ice formation, it follows the theory explained in section 3.1 and computes the ice crystals nucleation and growth in each one of the air parcels of the initial grid, using the bin scheme designed by Dinh and Durran (2012). The results of this microphysical scheme were checked by comparison to those of the box model of Spichtinger and Krämer (2013), for sensitivity of ice crystals number nucleated versus vertical speed (figure 3.4). Then the second block, in grey, is in charge of computing ice crystals sedimentation and their redistribution into the different air parcels, following the horizontal wind shear represented. We focus in this section on this sedimentation part which will have a major role in the computed dehydration. The point is to understand how sedimentation affects the ice crystals population generated in a simple large scale ascent.

3.2.1 Sedimentation of ice crystals: theory

The number of ice crystals falling out of the air parcels is computed for spherical crystals. This is a simple first step, before the modelling of non spherical shapes, actually present in cirrus clouds, which would span a range of different flow regimes. The number of falling crystals depends on their size, and is calculated by assuming that the crystals are homogeneously dispersed in the air parcels. As this calculation is made at each time step, the crystals are therefore virtually redistributed in the whole air parcel each time. This reproduces the effect of mixing that occurs within air parcels. Namely, the fraction of crystals that fall out the air mass is calculated as:

$$N_t(r) = N_{t-\mathrm{d}t}(r)\frac{w(r)}{h}\mathrm{d}t \tag{3.18}$$

with N_t the number of ice crystals of radius r, $\mathrm{d}t$ the time step and h the air parcel thickness and $w(r)$ the fall speed of particles with radius r. The sedimentation half-life time is therefore

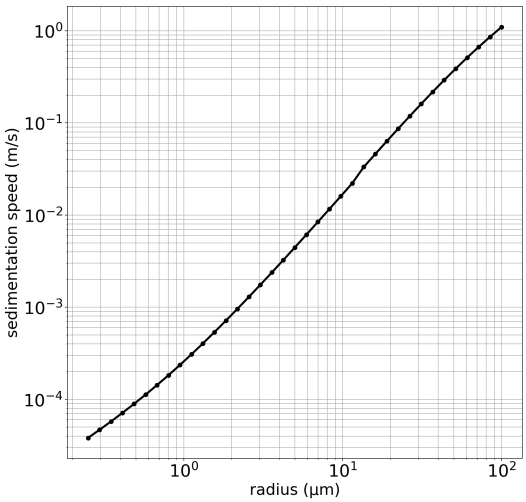

Figure 3.5: Mean sedimentation speed for the different bins of size, over 50 h of simulation following a temperature profile typical of the TTL.

computed as $\tau_{sed}(r) \approx \frac{h}{w(r)} \ln(2)$. Figure 3.5 displays the computed ice crystals fall speed for different sizes of spherical ice crystals.

The terminal velocity depends on the crystal Reynolds Number (Re) that represents the ratio between inertial and viscous forces, and is dependent on the crystal size and background temperature. The differentiation of the flow regimes is that suggested by Kärcher (2003), who calculates the Best number in order to assess Re following Pruppacher et al. (1998), page 417. For spheres, the Best number is the same as the unified Davis Number for columnar, planar, and other ice particles defined by Böhm (1989) and computed as $X = C_D Re^2 = \frac{8mg\rho_a}{\pi\eta^2}\left(\frac{A}{A_e}\right)^{1/4}$, with A and A_e respectively the cross sectional area and projected cross sectional area in the flow. The fraction is equal to unity for spherical particles. η is the dynamic viscosity, m the mass of ice and ρ_a the mass density of air, and C_D the drag coefficient. Different regimes are found:

1. $Re < 0.01$: Stokes Cunningham regime, for particles with radii between 0.5 and 10 microns, that will experience a stable fall with an equilibrium between the gravitational and drag forces in a fraction of seconds. Their terminal fall speed is therefore governed by Re of the flow around the falling ice crystal.

2. $0.01 < Re < 30$ for larger particles, with radius between 10 and 500 microns, that no longer undergo a stable fall. They follow an Osen-Best regime, here derived from Böhm (1989) formulation. At high enough Re, the crystal moving in the flow can be treated according to the boundary layer theory which assumes the boundary flow to stick to the particle, forming a new moving body that passes through an inviscid fluid with a constant velocity.

3.2.2 Simulation, impact of fall streaks on cloud cover and air parcels dehydration

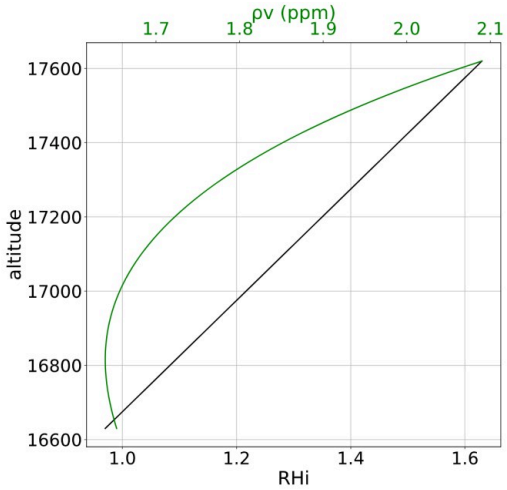

(a) (Green) Initial profile of volume mixing ratio (ppmv) and (black) S_i for the S1 and S0 experiment

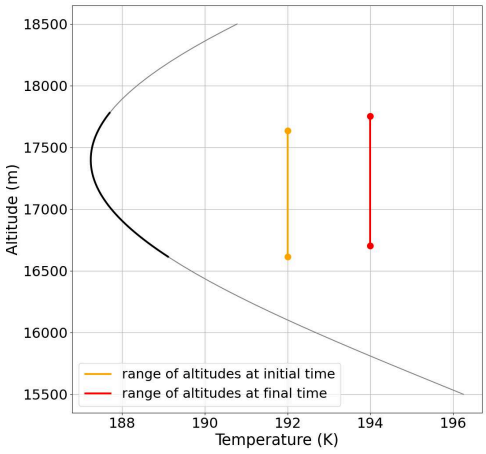

(b) Profile of temperature extrapolated from Kärcher and Podglajen (2019). Highlighted in black the range of altitudes covered during 50 h of simulation at w=0.5 mm/s for S0 and S1. The corresponding cooling rates are typically of 4 mK/h.

Figure 3.6: Environmental conditions for S0 and S1.

Initial conditions We run two experiments with the same initial conditions: 210 air parcels, distributed among 3 identical columns (the impact of the horizontal mixing is therefore minimised here, the sensitivity to this parameter will be further described in the article, section 3.3). Each parcel is 15 m thick and 150 m wide, and the whole simulated domain is centered around the cold point, with altitudes from 16 600 to 17 650 m. The initial profile of RH_i is set depending on the altitude, in order to have nucleation at the top of the domain. The corresponding water vapor mixing ratio $\rho_v(ppmv)$ is described in figure 3.6a, and follows:

$$S_i = \frac{\rho_v}{\rho_v^{sat}(T)} = \frac{p_{H_2O}}{p_{H_2O}^{sat}(T)} \tag{3.19}$$

with p_{H_2O} the partial pressure of water vapor. The domain is initially almost completely supersaturated. Both simulations represent the uplift of the 210 air parcels at a vertical speed of 0.5 mm/s (typical value for an uplift balancing the radiative heating (Fueglistaler et al., 2009)) during $\approx$ 50 h. Their temperature follows a typical TTL profile, extrapolated from radiosonde measurements (figure 3.6b) .

Cloud evolution The S1 simulation represents the sedimentation as described in the lines above, whereas in the S0 simulation the sedimented ice crystals are removed from the simulation as soon as they sediment from the air parcel: thus allowing the drying of the air mass,

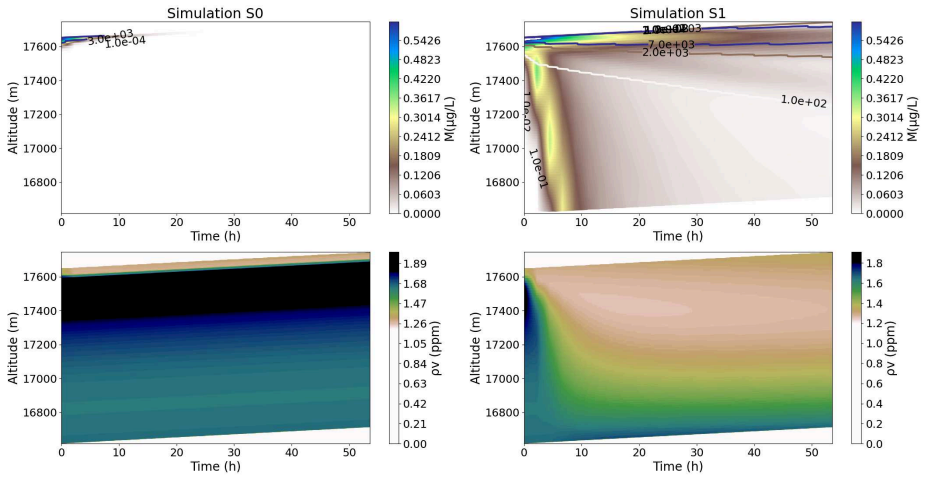

Figure 3.7: Evolution in time and altitude of ice mass (color) and ice crystals number (contours) (upper panel) and water vapor mixing ratios (bottom panel) for the S0 (left) and S1 (right) experiments

but not the transmission of ice from one air mass to another. It is an oversimplified sedimentation slightly closer to reality than the idealized models which suppose an instantaneous drying of the air masses with an infinite speed of the ice crystals as soon as they nucleate (Dinh and Fueglistaler, 2014): here, as long as crystals stay in the air parcel in which they have nucleated, they can continue to grow and capture moisture in excess of saturation. Note that these simplified models have still given satisfactory results for estimating the annual and interannual variability of water vapour entering the stratosphere (Fueglistaler, 2005; James et al., 2008). Here, the comparison between the two simulations will differentiate the "native" crystals, nucleated within the air parcels, and the sedimented ones.

First, the comparison of the evolution profiles in time and altitude of the ice mass and mixing ratio (figures 3.7), indicates that ice nucleation occurs as expected at the highest levels. Part of the ice crystals is advected with the air masses and moves gradually upwards for S0 and S1. The evolution of this nucleating layer is better seen in S0, with a thinning in time as some crystals sediment out of it and the temperature increases once this layer has been advected above the cold point. After 35 h, all the ice has been removed from it.

An opposite crystals behavior is spotted from the beginning of S1: some crystals are large enough to fall out very quickly. They fall off a distance of $\sim$ 1 km in $\sim$ 8 h, which corresponds from figure 3.5 to an approximate radius of 10.5 microns. This fall streak is generated slightly below the layers nucleating the biggest amount of crystals, as in Murphy (2014). It dehydrates efficiently the domain, captures between 2 to 4 ppm of water vapor to the initial mixing ratio profile (figures 3.7 lower panels). It is thus disproportionately important compared to the advected crystals as it reaches a wide altitude range. This dehydration event is associated with a low ice-crystal concentration (contours), compared to the top levels of the cloud (Heymsfield, 2005).

We can conclude that first in the S0 case all air parcels that experience nucleation will dehydrate, when there is neither dehydration or hydration for air parcels that do not experience nucleation. Conversely, in the S1 case, the majority of the cloud did not experience direct nucleation, and is only created by the sedimentation of upper levels ice crystals (Dinh and Fueglistaler, 2014).
Second, as S1 shows ice in the whole domain after the initial fall streak, the cloud lifetime also depends on the represented sedimentation. Last, crystals falling after the fall streak are more spread in altitude: the fall streak has dehydrated most of the domain. Consequently the following ice crystals nucleated cannot grow as large nor sediment as fast. Their size is limited by the amount of water vapor available. Thus the importance of the fall streak will depend on the initial temperature profile as well as humidity (Murphy (2014)).

The evolution of the domain's humidity in S1 exhibits a minimum reached around the cold point after 20 h of simulation. It is re hydrated after a few hours from falling ice crystals. The dehydration from S0 is very underestimated compared to S1. This result would have changed for heterogeneous nucleation, in which the nucleation threshold is lower.

Ice crystals populations The evolution of ice crystals population is described respectively for S0 and S1 in figures 3.8b, 3.8a. S0 population shows that the 15 m thickness of the air parcels allows a maximum growth of the ice crystals within the air parcel to $r \approx 11$ μm for homogeneous nucleation with small cooling rates of around 4 mK/h. Larger sizes fall out rapidly, so the average size of crystals in the air parcel is divided by two after a couple of hours only. In these nucleating layers, the crystals population evolution depends on the cooling rates that lead to nucleation as well as to the initial supersaturation.

S1 exhibits the importance of the fall streak, during which the maximum size of the whole simulation is reached (≈ 22 μm at ≈ 6 h): at the bottom of the domain, crystals became twice larger than in their nucleating layer, dehydrating efficiently the air masses.
After the fall streak, the maximum size that can be reached by ice crystals is decreased (figure 3.8a left panel): it therefore takes longer for ice crystals to fall out, which creates wider "steps" in the stair case pattern of the figure. This is again showing that the final size of the crystals and therefore the life time of the cloud depends on the humidity available as well as the initial number of ice crystals nucleated.

Two different behaviors can be distinguished in the size evolution: crystals with a radius bigger than 3 microns nucleated below the cold point and can grow (see the dark green contours positive slope), when smaller ones are nucleated above the cold point and will be advected with the warming air parcels above the cold point.

Crystal population is function of the altitude. Figure 3.8a exhibits the growth of ice crystals in a supersaturated environment during sedimentation: the maximum size is increased by 10 times between the first 100 highest and 100 lowest meters, and a wider range of ice

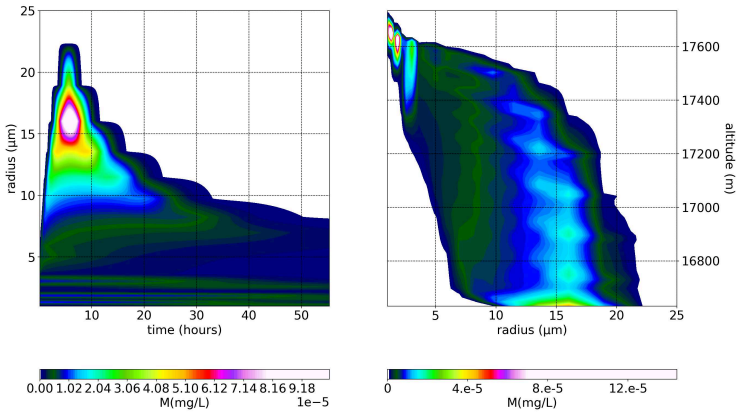

(a) S1 experiment

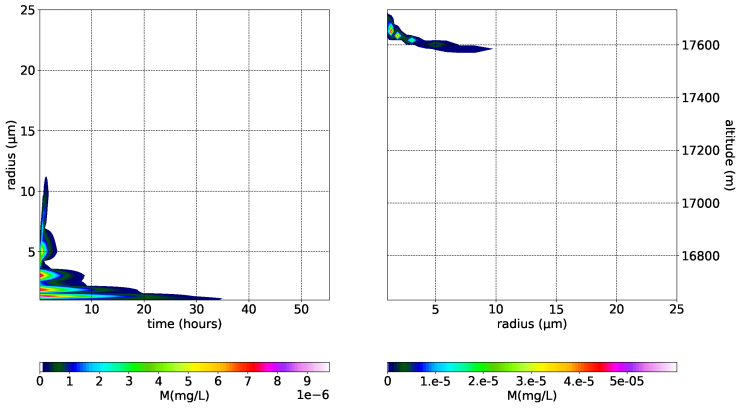

(b) S0 experiment

Figure 3.8: Ice crystals population evolution in time (left) and altitude (right) for S0 and S1 experiments

crystal sizes is observed in the lowest levels. There, the whole population is generated by sedimentation from upper levels, the final size depends only on the available humidity (note the absence of crystals smaller than 3 microns outside of the nucleating layers, as explained above).

The overall populations comparison are displayed figure 3.9. We distinguish the size of crystals nucleated within the layer (native) or coming from air parcels above (non native). For radius larger than 0.5 μm, more than half of the crystals present in the air parcels come from upper levels, when its the whole population above 3 microns. This supports that the number of ice crystals and the population are not determined by the nucleation at that location. Table 3.1 displays also the drastic increase of cloud fraction when sedimentation is taken into account.

We therefore showed first that the two parameters shaping the ice crystals population were the available humidity and, in the nucleating layer, the type of nucleation (here the cooling rates for homogeneous nucleation). This modulates the cloud ice crystal population with respect to altitudes as well as its life span. Sedimentation tends to increase the small vertical differences in the number of crystals into bigger fall streaks, the impact of which will be substantially larger than the one from small scale crystals.

The following article, submitted to Atmospheric Chemistry and Physics and still under revision, presents the impact of gravity waves on ice production, in terms of ice crystals population, cloud fraction, and air parcel dehydration. It uses the model described in the sections above.

3.3 Article: Impact of gravity waves on ice crystals populations

A simple model to assess the impact of gravity waves on ice crystal populations in the Tropical Tropopause Layer

Milena Corcos[1], Albert Hertzog[1], Riwal Plougonven[2], and Aurélien Podglajen[3]

[1]Laboratoire de Météorologie Dynamique/IPSL, Sorbonne Université, Paris, France
[2]Laboratoire de Météorologie Dynamique/IPSL, Ecole Polytechnique, Institut Polytechnique de Paris, Palaiseau, France
[3]Laboratoire de Météorologie Dynamique/IPSL, CNRS, Ecole Polytechnique, Institut Polytechnique de Paris, Palaiseau, France

Correspondence: Milena Corcos (milena.corcos@lmd.ipsl.fr)

Abstract. The role of gravity waves on microphysics of tropical cirrus clouds and air parcel dehydration was studied using the combination of Lagrangian observations of temperature fluctuations and a 1.5 dimension model. High frequency measurements during isopycnal balloon flights were used to resolve the gravity wave signals with periods ranging from a few days to 15min. The detailed microphysical simulations with homogeneous freezing, sedimentation and a crude horizontal mixing represent the slow ascent of air parcels in the Tropical Tropopause Layer. A reference simulation describes the slow ascent of air parcels in the tropical tropopause layer, with nucleation occurring only below the cold point tropopause with a small ice crystals density. The inclusion of the gravity waves modifies drastically the low ice concentration vertical profile and weak dehydration found during the ascent alone, with the increased ice crystal number and size distribution agreeing better with observations. Numerous events of nucleation occur below and above the cold point tropopause, efficiently restoring the relative humidity over ice to equilibrium with respect to the background temperature, as well as increase the cloud fraction in the vicinity of the cold-point tropopause. The corresponding decrease in water vapor is estimated at 2 ppmv around the cold point tropopause.

1 Introduction

Cirrus clouds are frequent and stand out as an important component in the Earth climate system (Winker and Trepte, 1998; McFarquhar et al., 2000). In the Tropical Tropopause Layer (TTL), they notably regulate the amount of water vapor that enters the stratosphere via the freeze-drying mechanism, i.e. ice particles forming near the cold point and sedimenting out of the ascending air masses (Jensen et al., 1996; Holton and Gettelman, 2001; Gettelman et al., 2002; Fueglistaler et al., 2009; Randel and Jensen, 2013). Stratospheric water vapor affects the Earth's radiative budget (Solomon et al., 2010), but also ozone destruction, surface climate and polar stratospheric clouds (Solomon et al., 1986; Toon et al., 1989). Microphysical characteristics of TTL cirrus, like ice crystal number density, size, and shape, have a strong influence on their radiative properties (Smith et al., 1998). The size of ice crystals furthermore determines their sedimentation velocity, and therefore impacts TTL cirrus lifetimes as well as the upper-troposhere and stratospheric humidity (Jensen et al., 2001).

Cirrus clouds can form in-situ within the TTL (Pfister et al., 2001). The relative importance of homogeneous and heterogeneous nucleation in the TTL is still debated (Jensen et al., 2018), but in-situ measurements of ice saturation ratios are ranging

from 1.1 to 1.7 in this region (Jensen et al., 2001; Krämer et al., 2009), suggesting that the majority of aerosols are hard to freeze. Measurements of tropical aerosols showed a significant fraction of organic components (Cziczo et al., 2004), and a small number of effective ice nuclei might also be present. These are nevertheless unlikely to fully suppress homogeneous nucleation, which is likely prevalent in the TTL (Kärcher, 2004; Krämer et al., 2009; Spichtinger and Krämer, 2013). Homogeneous freezing of aqueous aerosols is strongly sensitive to cooling rates (Jensen and Toon, 1994; Kärcher and Lohmann, 2002), so that TTL cirrus life cycle and microphysical properties are sensitive to temperature perturbations induced by gravity waves (Jensen and Pfister, 2004). Several idealized model studies explored the effects of wave-induced temperature variability on cirrus properties (Kärcher, 2003; Jensen and Pfister, 2004; Haag and Kärcher, 2004; Hoyle et al., 2005). The associated impact on dehydration in the TTL is still only partially understood though, as it notably depends on the amplitude and intrinsic frequency of the wave driven perturbations (Pfister et al., 2001; Jensen and Pfister, 2004; Kim and Alexander, 2015; Schoeberl et al., 2015), as well as on whether TTL cirrus form in-situ or are anvils of convective clouds (Kärcher et al., 2006; Corti et al., 2008; Schiller et al., 2009; Spichtinger and Krämer, 2013; Schoeberl et al., 2014). A number of processes, with a wide range of scales, affect the formation and evolution of cirrus clouds. Thus any modeling effort will induce important simplifications or even ommissions on parts of the processes involved.

Detailed microphysical simulations of TTL cirrus have naturally used Lagrangian box models (Hoyle et al., 2005), which are able to resolve the size distribution of ice crystals. Such models can notably estimate ice concentration maxima, yet a critical limitation is their difficulty to infer the dehydration of air parcels and the evolution of cirrus clouds on timescales significantly longer than that associated with nucleation. Other models track the size and heights of ice crystals in a curtain approach (Jensen and Pfister, 2004). At larger scales, the Community Aerosol and Radiation Model for Atmospheres (CARMA) model (Toon et al., 1988; Bardeen et al., 2008), which represents crystal formation, growth, aggregation and sedimentation, can be combined with global circulation models. Ultimately though, detailed information about the temperature variability experienced by air parcels is crucial to address the issue of small-scale dynamics impacts on cirrus clouds (Jensen et al., 2016). In that regard, superpressure balloon observations providing in-situ measurements of wave driven temperature variability in a quasi-Lagrangian framework were also used in idealized box-model simulations (Dinh et al., 2016; Jensen et al., 2016). These studies were nevertheless limited by the absence of sedimentation, which has a prominent role in determining ice concentration in cirrus clouds (Jensen et al., 2012, 2013b; Murphy, 2014).

This paper further addresses the question of gravity-wave impacts on in-situ tropical cirrus clouds. Our approach is to combine Lagrangian observations of temperature fluctuations to a simplified representation of microphysics to assess both TTL cirrus ice-crystal densities and dehydration efficiency. Our observation dataset is that collected during 8 superpressure balloon flights in the deep tropics, realized in the frame of the first Stratéole-2 campaign. This campaign took place in the 2019 boreal winter, and the balloon flights recorded timeseries of temperature fluctuations at ~ 19 km of altitude for 3 months typically. Our microphysical model is able to resolve ice crystal homegeneous nucleation and growth, as well as sedimentation. It also includes a simplified representation of horizontal mixing, which has been found important in the life cycle and evolution of long-lived TTL cirrus clouds (Dinh et al., 2010).

The plan of the article is as follows: the first Section provides details on our method and simulations. In the second Section, TTL cirrus found in simulations with and without gravity waves are described. The following Section discusses in more details the impacts of gravity waves on cirrus microphysical properties and dehydration efficiency. Our simulations are also compared to in-situ observations of TTL cirrus clouds. Main conclusions are provided in the last Section.

2 Method

2.1 Balloon-derived Lagrangian temperature timeseries

The wave-resolving temperature timeseries used in this study are derived from superpressure balloons measurements collected during the 2019 Strateole-2 campaign. During this campaign, eight balloons were launched by the "Centre National d'Etudes Spatiales" (CNES) in November and December, from Mahé Island (55,52°E, 4.67°S) in the Indian Ocean. The balloons drifted for two to three months at altitudes between ~ 18.5 km and ~ 20.5 km of altitude within the whole tropical belt. More information about the balloon trajectories and their environment during the flights can be found in Corcos et al. (2021).

Superpressure balloons directly record the instrinsic periods of wave motions, i.e. the period of disturbances felt by air parcels advected by the atmospheric flow (Nastrom, 1980; Hertzog and Vial, 2001). During the Strateole-2 campaign, each balloon was carrying a TSEN instrument that records pressure and temperature every 30 s, hence resolving the whole gravity-wave spectrum. In this study, we have chosen not to use the direct temperature measurements recorded onboard the balloons, since they tend to be influenced by the flight chain wake during day. Instead, we have reconstructed temperature disturbances from pressure measurements. This reconstruction is based on three assumptions: (i) wave perturbations are hydrostatic, which enables us to relate the pressure disturbance to the balloon vertical displacement (ζ'_b), (ii) superpressure balloons drift on constant-density surfaces (Vincent and Hertzog, 2014), and (iii) wave perturbations are fast enough so that they can be considered as adiabatic transformations. These assumptions are valid for waves with intrinsic periods significantly longer than the Brunt-Väisälä period (~ 5 minutes in the lower stratosphere), but shorter than the radiative damping time in the TTL ($20-30$ days Gettelman et al., 2004).

The isentropic air parcel displacements (ζ') then relate to those of the balloons according to (e.g., Boccara et al., 2008; Podglajen et al., 2016):

$$\zeta' = \frac{1}{\alpha}\zeta'_b \tag{1}$$

where

$$\alpha = \frac{g/c_p + \partial\overline{T}/\partial z}{g/R_a + \partial\overline{T}/\partial z} \tag{2}$$

with g is the gravitational acceleration, c_p and R_a the specific heat at constant pressure and perfect gas constant per unit mass for dry air respectively, and $\partial\overline{T}/\partial z$ the vertical gradient of the background temperature, estimated from ERA5. Then, following

adiabaticity, the Lagrangian temperature fluctuations may be deduced (e.g., Podglajen et al., 2016):

$$T' = -\frac{g}{c_p}\zeta' \tag{3}$$

and are checked to be very close to the temperature measurements. To be consistent with the above assumptions and to specifically study the role of gravity waves in cirrus cloud microphysics, we have applied a Bessel band-pass filter to the balloon timeseries, with cutoff periods at 15 min and 1 day. We have checked that our results are qualitatively not sensitive to the filtering method.

It should be noted that the balloon data from Corcos et al. (2021) were obtained at altitudes slightly above that of interest (the upper TTL, 17 km). Contrary to Schoeberl et al. (2018), we did not reduce the amplitude of the stratospheric balloon fluctuations, since Lagrangian temperature fluctuations are expected to be roughly constant over that altitude range, contrary to Eulerian ones (Podglajen et al., 2016; Kärcher and Podglajen, 2019).

2.2 Microphysics model and experiment setup

2.2.1 1.5 dimensional representation of microphysics

Our microphysical model aims at studying the in-situ formation and evolution of cirrus clouds at high altitude. It is based on the model developed in Dinh and Durran (2012) and Dinh et al. (2016), which simulates the homogeneous nucleation and growth of ice crystals in a single box under varying temperature and pressure conditions. The evolution of ice crystals number and mass is detailed in 36 bins of size, with radius ranging from 0.25 μm to 0.1 mm. Nucleation occurs by freezing on particles of ammonium sulfate, as argued by Jensen et al. (2010) to be a good candidate for homogeneous nucleation in the TTL. This aerosol is described with one bin of size, since previous studies have shown that ice formation generated by homogeneous freezing is not very sensitive to the aerosol size distribution (Jensen and Toon, 1994). The aerosol concentration is chosen as 230/L, guided by observations of aerosols in the upper troposphere (Hermann et al., 2003). The nucleation rate is computed according to the formulae of Koop et al. (2000), which assume that the nucleation rate coefficients solely depend on the difference of activity between the liquid aerosol solution and ice. Nucleation therefore occurs for relative humidity with respect to ice (RHi) of 157-158%.

Dinh's box model did not allow a description of sedimentation. The size distribution makes it possible to estimate a terminal velocity for each size bin, and hence with an assumption on the box thickness an outgoing mass flux rate. In this zero dimension model however no ice can sediment into the box, so sedimentation effects are at best half described. We therefore extended the box model into a vertical dimension. A one dimensional model (Jensen et al., 2013a, 2016; Kärcher, 2002) has the disadvantage of artificially constraining all fluid parcels to remain vertically aligned, we thus add a crude representation of vertical wind shear to also allow horizontal mixing of ice crystals. Thus, our representation is of 1.5 dimensions. The geometrical setup of air parcels is displayed in Figure 1 (left panel).

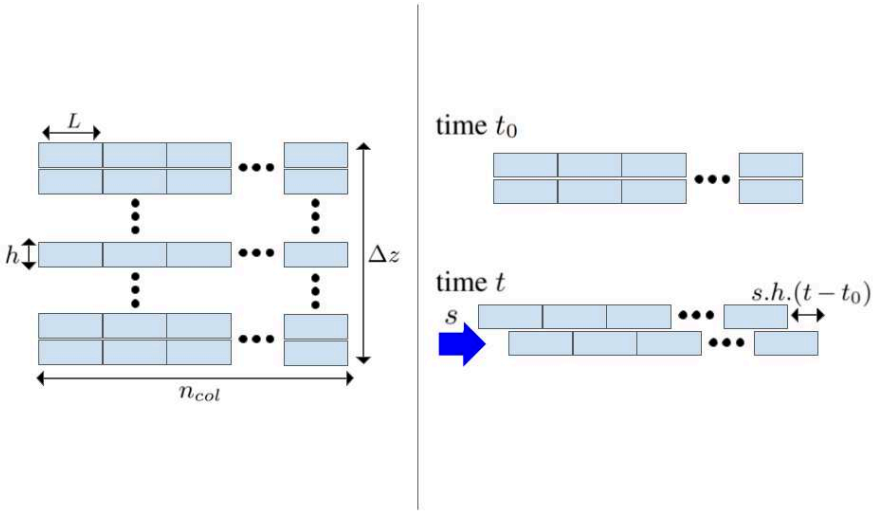

Figure 1. (Left) Representation of the modelled air parcels distributed among columns. (Right) Representation of the wind shear impact on two consecutive layers of air parcels. All letters are listed in table 1.

The sedimentation fall speed is calculated assuming spherical shaped crystals, and is based on the Reynolds number (Re) of the flow around the crystals (Böhm, 1989, eq. 11). It uses an Oseen-Best regime for $0.01 < \mathrm{Re} < 300$, and a Stokes-Cunningham regime at smaller Re (Kärcher, 2003). The fraction of ice crystal number that sediments from one air parcel to that directly below ($f_s(r)$) is inferred assuming an uniform distribution of crystals in air parcels. It comes:

$$f_s(r) = w(r)\,dt/h \tag{4}$$

with r the radius of the ice crystal, h the thickness of the airmass, and dt the time step of the model. The vertical shear of horizontal wind (s) furthermore contributes to advecting horizontally ice crystals during their sedimentation. Our implementation of sedimenting ice crystals includes a module aimed at a rough representation of wind shear (figure 1 right panel). Namely, during a time δt, a given row of air parcels (at a given altitude) has moved to that immediately above or below by $sh\,\delta t$. When this displacement becomes larger than half of the air parcel length (L), we randomly shuffle the air parcels. This thus happens every $l/(2sh)$. Unless otherwise noted, we assume a vertical shear typical of the tropical UTLS: $s = 10$ m/s/km.

The nucleation and growth of ice crystals simulated by our model is validated by comparison to Spichtinger and Krämer (2013). We find the same relationship between constant vertical updraught speeds and ice crystals number concentration: a power-law variation for the slower vertical speeds and a saturation in ice crystal number associated with the pre-existing background aerosol reservoir for the highest speeds (Spichtinger and Gierens (2009)). The simulated amount of ice crystals is furthermore found to be of the same order of magnitude.

2.2.2 Model dynamics

The temperature evolution of individual air parcels in the model includes two different processes. First, diabatic heating forces air parcels to slowly ascend through the TTL (Fueglistaler et al., 2009). This mean vertical motion is represented in the model by a constant vertical speed $\bar{w} = 0.5$ mm/s, typical of the TTL (e.g., Jensen et al., 2001; Boehm and Lee, 2003; Salby and Callaghan, 2004). As air parcels ascend diabatically, their temperature adjusts on a background temperature profile ($\overline{T}$, see Figure 2) representative of the TTL (Kärcher and Podglajen, 2019). Second, air parcels optionally undergo adiabatic temperature disturbances generated by gravity waves. To represent these fluctuations, a time sample with the same duration than that of simulation is randomly chosen in the balloon-borne temperature-disturbance timeseries for each model air parcel independently. While these wave-driven Lagrangian temperature disturbances are associated with air-parcel vertical displacements in the real atmosphere, we do not track those vertical motions in the model. Doing this, we assume that the wave-driven disturbances are associated with linear waves, inducing on average zero net vertical displacement. The altitudes of air parcels in the model therefore only evolve due to the slow diabatic ascent.

Two obvious limitations of the model need to be highlighted: first, we did not attempt to represent the correlation of wave-driven temperature fluctuations between nearby air parcels. In a sense, our simulations thus maximize the random effect of gravity waves in microphysical processes. Second, our microphysical model does not represent the dynamics induced by the cloud itself, such as turbulence or radiatively-driven effects. Our simulations therefore apply to situations where those effect can be neglected at first order, i.e. optically thin cirrus associated with weak heating rates (Jensen et al., 2016).

2.2.3 Model configurations

The simulation geometry (number of rows and columns) and that of individual air parcels (vertical thickness and horizontal length) are free parameters of the model. In the simulations displayed in this study yet, we have always used the same geometry: 6 columns of 70 rows with 15-m thick, 150-m long air parcels. In particular, the air-parcel thickness was set as in Jensen et al. (2010), i.e. allowing the growth of ice crystals within the air parcel while maintaining a fine vertical resolution. Sensitivity tests have shown that our results do not depend on this specific choice.

Four simulations are performed in this study to assess the impact of gravity waves on ice crystals populations. First, a no-wave control simulation (NW) aims at representing TTL cirrus clouds generated by the slow radiative ascent only. The three other simulations all include wave-induced temperature perturbations. A preliminary simulation (wave first test, "WFT") starts with the same (large) initial relative humidity (RHi_0) than the no-wave simulation. We argue in the following that this is not the optimal choice for a wave simulation. Hence, we will discuss in more details the third simulation (W), in which $\mathrm{RHi}_0 = 1$. Last, in the no-mixing experiment ("NM"), we toggle off the mixing module in order to test the sensitivity of our results to this effect. The input parameters of all simulations are summarized in Table 1.

The relative humidity at the start of the simulation (RHi_0) is constant along the whole column. RHi_0 varies between our simulations and the choice of this parameter is further discussed below, but we will see that longer simulations remove the sensitivity to the initial relative humidity.

Parameters	Symbol	No Wave NW	Waves (first test) "WFT"	Waves W	Waves (no mixing) "WNM"
Number of air parcels	n	420	420	420	420
Number of columns	n_{col}	6	6	6	6
Thickness of air parcels	h	15 m	15 m	15 m	15 m
Length of air parcels	L	150 m	150 m	150 m	150 m
Altitude span of setup	$\Delta z = h\frac{n}{ncol}$	1050 m	1050 m	1050 m	1050 m
Mean vertical speed	$\bar{w}$	0.5 mm/s	0.5 mm/s	0.5 mm/s	0.5 mm/s
Standard deviation of wave-induced temperature perturbations	$\sigma(T')$	0	1.5 K	1.5 K	1.5 K
Wind shear	s	10 m/s/km	10 m/s/km	10 m/s/km	0
Duration of simulation	Δt	72.2 h	h	51.5 h	37 h
Initial RHi	RHi_0	1.5	1.57	1	1

Table 1. Table of simulation definitions

3 Results

3.1 The slow-ascent simulation

The NW simulation corresponds to a 72-h ascent of air parcels encompassing the cold-point tropopause. During that time frame, air parcels have ascended for ~ 130 m. Due to the slow vertical speed, the associated cooling rates are very low, typically ± 4 mK/h (Figure 2). The initial relative humidity ($\mathrm{RHi}_0 = 1.57$) is chosen close enough to the nucleation threshold, so that nucleation occurs during the simulation. We will first qualitatively describe the ice formation, its evolution in time and altitude, and then focus on the population of ice crystals.

Figure 3 displays the evolution of the ice mass and ice crystal number as a function of time and altitude for the lower-altitude air parcels only. Indeed, the three main nucleation events that occurred during the simulation were all located below the cold point, as the air parcels above will only warm up in time.

These nucleation events start first in the lowest layers of the setup. This can be understood since these layers are those where the temperature gradient is the most negative (see Fig 2). Hence, air parcels located in the lower part of the setup experience the largest cooling rates, and nucleate first. Below an initial altitude of ~ 17.1 km, all air parcels undergo at least one nucleation event, which occurs later and later as altitude increases (and the absolute temperature gradient decreases). In contrast, the RHi of air parcels located closer (or even above) the cold point never crosses the nucleation threshold.

This dependence of the cooling rates with altitude also explains that the largest numbers of nucleated ice crystals are found in the lowest layers of the simulated domain (e.g., Spichtinger and Krämer, 2013). The second and third nucleation events produce less ice crystal number and less ice mass, partly because they occur higher up and are thus associated with lower cooling rates and partly because air masses have already been depleted in water vapor by ice crystals that have sedimented out

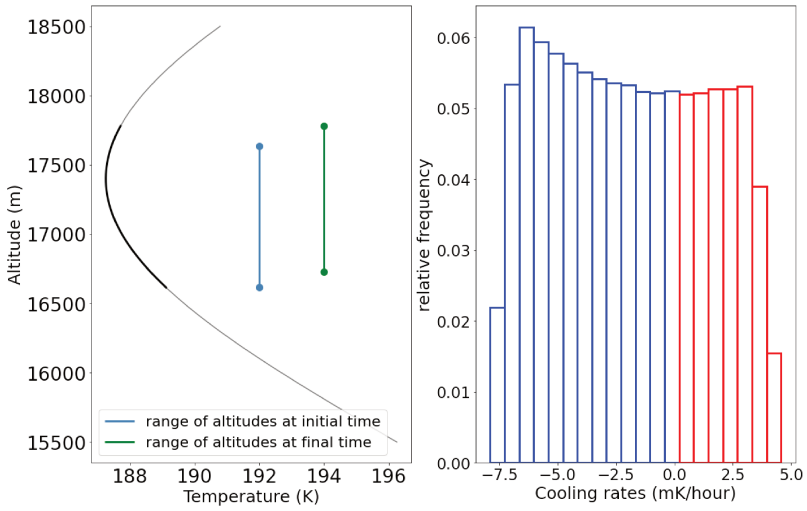

Figure 2. (Left) Temperature profile based on Kärcher and Podglajen (2019) radiosonde measurements in the tropics (171° E, 7° N), averaged over a year. The range of temperatures seen by air parcels in the NW simulation is highlighted in black. The initial and final altitude ranges of air parcels are indicated by the blue and green vertical bars respectively. (Right) Corresponding cooling rates with an ascent speed of 0.5 mm/s.

before. Last, growth and sedimentation of the crystals account for the time shift of a few hours between the maximum of ice crystals number and the maximum of ice mass, which is especially observed during the first two nucleation events.

The evolution in time and altitude of the crystal size distribution during the NW simulation is displayed in Figure 4. The time evolution (left panel) and altitude evolution (right panel) are respectively a vertical average and a time average over the whole domain. The time evolution clearly exhibits the three nucleation events: at $t < 10$ h, $t \sim 20-30$ h, and $t \sim 40$ h. During those, ice crystals reach $5\ \mu$m within less than 1 h, while it takes ~ 5 h for them to grow beyond $15\ \mu$m. This timescale, which is associated with the very low temperatures of the tropical tropopause, is prone to include modulation of the crystal growth by gravity waves, as suggested in Dinh et al. (2016) and Podglajen et al. (2018). Beyond $15\ \mu$m, the ice crystals tend to sediment quickly out of the model domain, so that the size distribution in this NW simulation is fairly narrow and peaks at $\sim 14\ \mu$m, in agreement with previous results (e.g. Jensen et al., 2010).

This is further illustrated in Figure 5, which shows typical timescales for sedimentation and growth of ice crystals depending on their size. Regarding sedimentation, the timescale shown corresponds to the time needed for half of the ice crystals to leave an air parcel of height $h = 15$ m. The timescale associated with crystal growth depends on supersaturation ($\mathrm{RH_i} - 1$), and is displayed for a supersaturation typical of the NW simulation (0.6) as well as for a lower value (0.25), which will be used later on. In the NW simulation, the two timescales are of similar value for ice particles with $r = 7\,\mu$m. Indeed, it can be observed on the right panel of Figure 4 that particles with larger radii are not observed in the upper layers where nucleation occurs. Hence, particles with $r > 7\,\mu$m typically grow while they sediment, and are thus not encountered in the layers where they

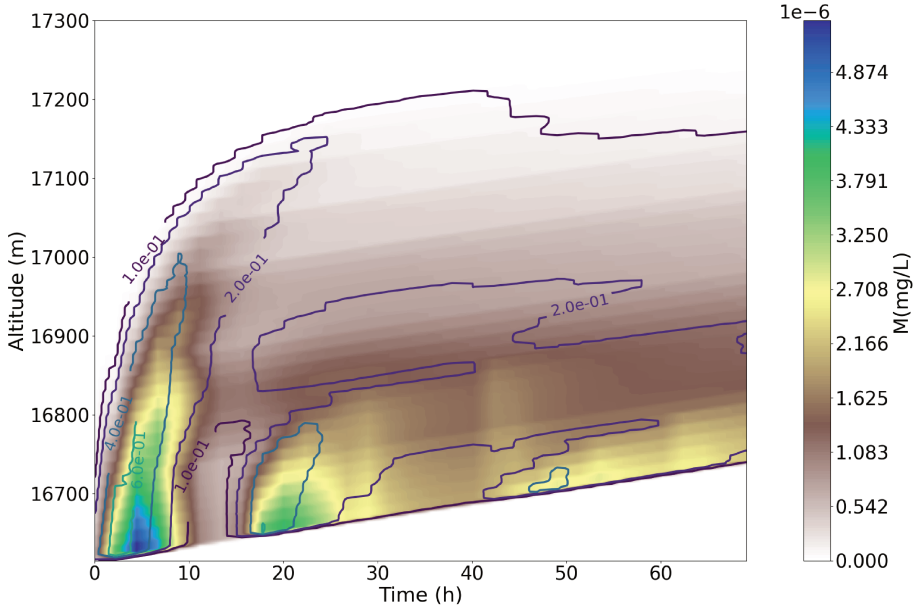

Figure 3. Evolution of ice mass (in $\mathrm{mg\,L^{-1}}$, color) and ice crystal number (in $\mathrm{L^{-1}}$, contours) in time and altitude for a simple slow ascent of 420 air parcels. Note that the altitude range is restricted to the lower part of the simulation domain.

have nucleated. The sedimentation timescale for the bulk of the largest particles ($r \sim 15\,\mu$m) in the NW simulation is $1/10$ hr. Since those particles are observed 5 hr after the start of the simulation, they have typically fallen over $50\,h = 450$ m, which corresponds to the height difference between the model base and the uppermost layer where nucleation occurs (Fig. 4). On the other hand, the sedimentation timescale for ice crystals with $r < 3 - 4\,\mu$m is one order of magnitude larger than their growth timescale, and those particles are then mostly observed in the layer where they have nucleated.

3.2 The gravity-wave simulations

3.2.1 A preliminary experiment

A first test simulation that includes wave-induced temperature perturbations ("WFT") is performed with an initial relative humidity close to the nucleation threshold ($\mathrm{RHi}_0 = 1.57$), as in the NW simulation. The evolution of the mean relative humidity in the simulated domain is displayed in Figure 6. The wave-driven temperature perturbations trigger multiple events of nucleation, and the stronger cooling rates encountered by air parcels hugely increase the ice crystal production in comparison with the NW simulation, as already highlighted in previous studies (Dinh et al., 2016; Jensen et al., 2016; Kärcher et al., 2019). The ice crystal growth in the supersaturated environment efficiently depletes the water vapor, and the mean relative humidity consequently decreases within a few hours toward a value close to equilibrium (0.95). This behavior is in stark contrast with the NW simulation, where the low number of ice crystals produced did not succeed to significantly reduce the relative humidity. It is a strong indication that waves likely allow a faster dehydration of air parcels more efficient, than the slow large-scale ascent.

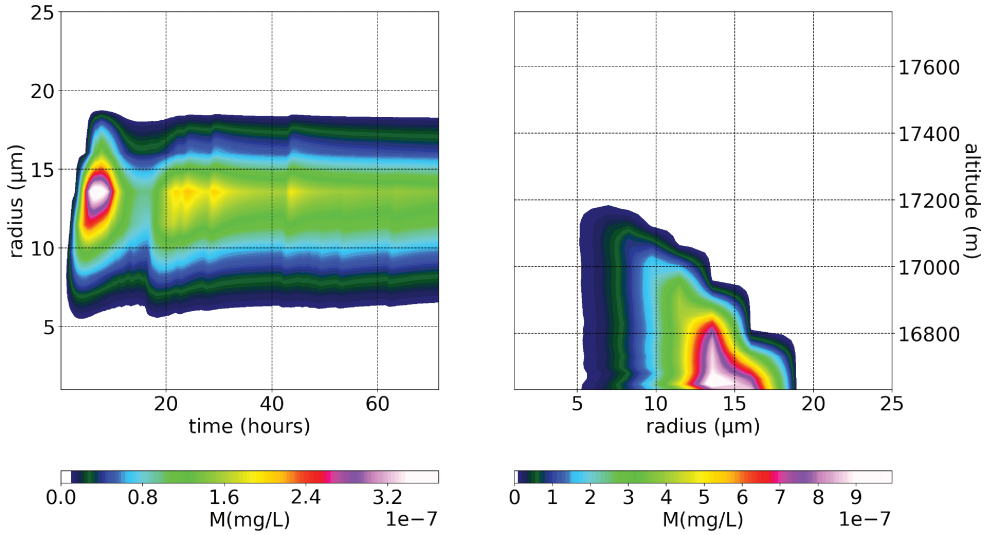

Figure 4. Evolution of ice mass in time (left) and altitude (right) for the NW simulation. Bins filled with more than one ice crystal per cubic meter are colored.

Yet, the initial decrease in relative humidity seen in the "WFT" simulation is unlikely to occur in the real atmosphere and rather indicates a flaw in the initial relative humidity which is inconsistent with the ubiquitous presence of gravity waves. We therefore designed a more realistic wave experiment (W) that starts with an initial relative humidity of 1, and is described in more details in the following section. During this simulation, the domain-averaged RHi varies in a very limited range.

3.2.2 A more realistic wave simulation

As already mentioned, one major effect of gravity waves is to widen the distribution of heating/cooling rates experienced by air parcels. This is illustrated in Figure 7, which shows the temperature timeseries for two air parcels respectively located below and above the cold point tropopause, as well as the probability distribution function of heating/cooling rates in the whole domain. Recall that the temperature fluctuations are random samples of balloon observations in the tropical lower stratosphere. The short-period wave-driven perturbations obviously dominate the either negative or positive temperature trend associated with the large-scale ascent. The standard deviation of heating/cooling rates in the wave simulations is 5 K/h, i.e. a thousand time larger than in the NW simulation, which drastically modifies ice production.

Figure 8 displays the evolution of the mean ice mass in the simulated domain in the W simulation. In contrast with the NW simulation, nucleation occurs almost constantly during the whole duration of the simulation. Furthermore, as the wave-

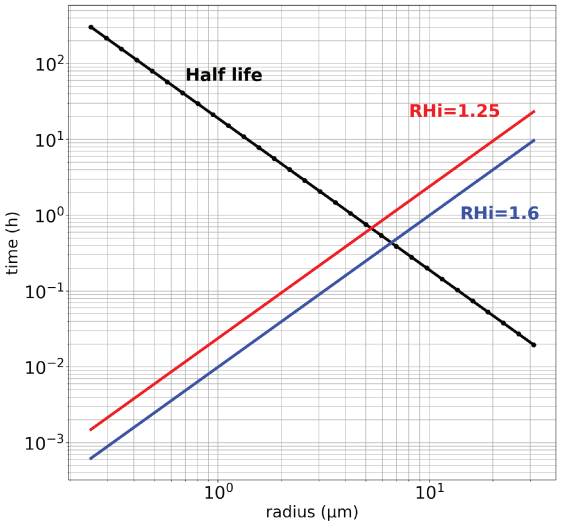

Figure 5. Half time (black), growth rate for RHi=1.25 (red) and RHi=1.6 (blue) depending on ice crystals size.

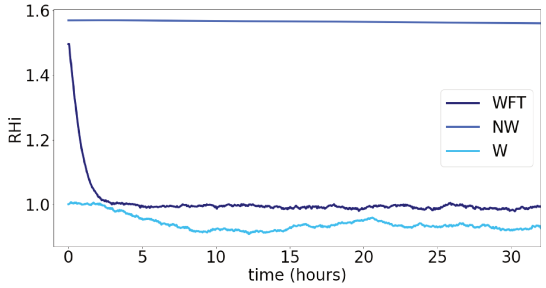

Figure 6. Evolution of relative humidity with respect to ice for the simulations "WFT", NW and W.

induced temperature fluctuations are dominating air parcels temperature evolution, ice crystals are produced at all altitudes, even above the mean cold point tropopause (~ 17.4 km). Two distinct behaviors can be observed in the figure: first, some of the ice crystals are slowly advected upward at the same speed than air masses. They stay in the nucleating layer. This corresponds to small-size crystals, which typically need several tens of hours to sediment out of the air mass in which they have nucleated (cf. Figure 5). These crystals may eventually re-sublimate when air parcels experience a warm temperature disturbance, and will therefore have little (if any) effect on the dehydration of air parcels. On the other hand, the largest ice crystals sediment out efficiently, widen the cloud layer and dilute the initial amount of ice. They contribute to dehydrate air parcels. Several fall streaks associated with sedimenting crystals are observed in Figure 8. Some fall speeds are superimposed on the figure to illustrate that those larger crystals have typical sizes between 3 and 8.5 μm. Note that the fall streaks are

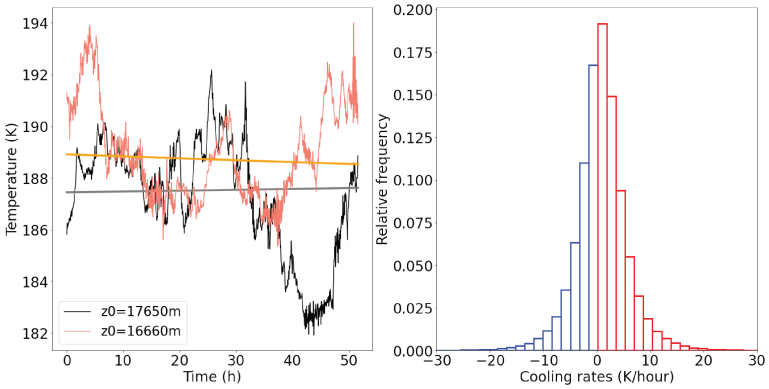

Figure 7. (Left) Timeseries of temperature for two air parcels at different altitudes. Background temperature interpolated from Kärcher and Podglajen (2019) radiosonde is superposed. (Right) Corresponding cooling rates with an ascent speed of 0.5 mm/s.

well fitted assuming ice crystals with constant radii, in an environment close to equilibrium (RHi ≈ 1). Larger crystals may be created by a comparatively small temperature perturbation, a quenched nucleation (Dinh et al., 2016), or even ice crystals that have nucleated in response to a previous temperature fluctuation and which damp the wave-driven evolution of RHi (Jensen et al., 2010; Spichtinger and Krämer, 2013). This stresses that bigger crystals can be found at all altitudes and not only at the lower levels after sedimentation.

Overall, the ice mass field in this W simulation is much more heterogeneous than in the NW simulation. This heterogeneity certainly results from the uncorrelated timeseries of wave-induced temperature disturbances between air parcels, even though Figure 8 shows the mean ice mass field and therefore somewhat damps out a part of the inter-parcel differences. Yet, we note that this heterogeneity is also reminiscent of high resolution profiles of cloud properties, like those obtained during the ATTREX experiment (Jensen et al., 2013a).

Figure 9 displays the evolution in time and altitude of the crystal-size distribution during the W simulation. The time evolution exhibits some striking differences with the corresponding figure for the NW simulation. First, ice crystals hardly grow larger than $8\,\mu$m when wave effects are included, i.e. half the maximum size reached in the NW simulation. The ice mass is mostly associated with ice-crystal radii of $3-6\ \mu$m, i.e. a factor 3 to 4 smaller than in the NW simulation. The typical growth timescale of the largest crystals (~ 10 h) is also much slower. This can be first understood since the larger cooling rates induced by wave perturbations contribute to nucleate a larger number of ice crystals than when only the slow ascent is responsible for nucleation. These numerous ice crystals then deplete water vapor more efficiently from the gas phase, and therefore grow more slowly than in the NW simulation. This first effect is illustrated in Figure 5, which shows in red the characteristic growth time of ice crystals at a lower supersaturation (0.25) than that of the NW simulation (0.6). The 0.25 supersaturation value corresponds to one standard deviation of supersaturation in the W simulation. The ice crystal growth times are twice as large at this overall lower supersaturation than in the W simulation, but still remain somewhat shorter than those inferred from Figure 9. A second

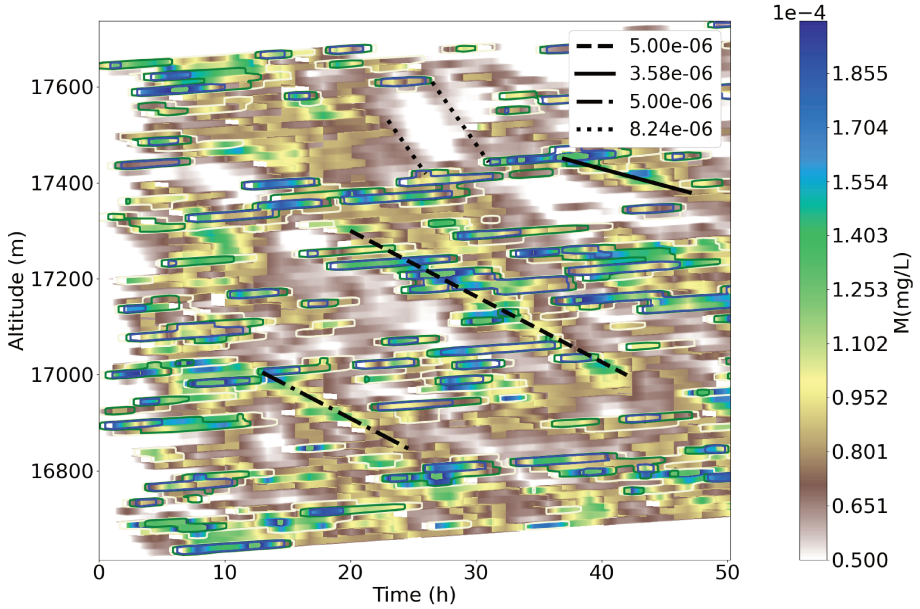

Figure 8. Evolution of ice mass in time and altitude for W simulation. Contours are representing the number of ice crystals /L, light brown N=1000, green N=2500, blue N=5000

wave effect that furthermore contributes to slowing the ice crystal growth timescale is the encounter of warm temperature disturbances by air parcels. Indeed, ice crystals larger than $\sim 5\,\mu$m have typical growth timescale larger than 1 hr, allowing wave-induced temperature fluctuations to potentially reduce the supersaturation over that timescale.

The altitude evolution once again illustrates the distinct behavior of small ice crystals with radius $r < 2-3\,\mu$m, which tend to essentially remain and grow in the air mass in which they have nucleated, and that of larger ice crystals that tend to essentially sediment out of it. In the W simulation, the sedimentation is observed as soon as the crystals reach radii larger than $5\,\mu$m, in agreement with the lower overall supersaturation of this simulation (see Fig. 5). The altitude evolution also highlights the correlation between crystal sizes and their sensitivity to high-frequency temperature fluctuations: the larger the radius, the less the sensitivity. Smaller crystals respond quickly to their environment and are therefore easier to sublimate if a warm wave-induced temperature fluctuation creates subsaturation.

Interestingly, ice crystals with radii larger than $5\,\mu$m are observed throughout the simulated domain in the W simulation, and even above the cold point tropopause. A possible nucleation mechanism for those high-altitude large crystals may be quenched nucleation events, as suggested in Dinh et al. (2016): as the background temperature increases in the stratosphere, waves will progressively create shorter and shorter nucleation events, which will limit the number of produced ice crystals and allow them to grow more efficiently. Sedimentation hence occurs at all altitudes in the W simulation, which furthermore highlights that waves likely contribute to the dehydration of air parcels in the TTL.

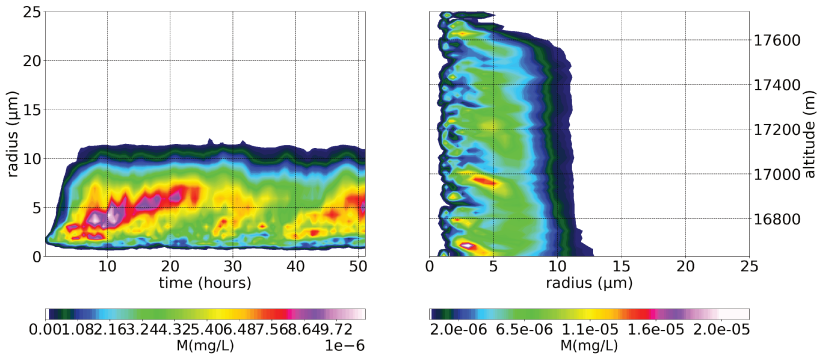

Figure 9. Evolution of ice mass in time (left) and altitude (right) for a simple slow ascent of 420 air parcels. Bins filled with more than 1 crystal per cubic meter are filled.

4 Discussion

4.1 Ice production with and without waves and comparison with measurements

The main characteristics of ice production in the no-wave and wave simulations are summarized in Table 2. The most striking feature is the difference of four orders of magnitude between the overall mean ice crystal concentrations (N_{ice}) in the simulations with and without gravity waves, which results from waves triggering more nucleation events and generating larger cooling rates than the mere slow ascent in the TTL. The condensed mass in the W simulation is decreased by a factor ~ 100 only with respect to that in the NW simulation, since ice crystals are of smaller sizes when wave perturbations are included. The overall cloud fraction, defined here as the fraction of time where $N_{ice} > 10\,L^{-1}$ in at least one parcel per column, is null in the NW simulation and almost 100% in the W simulation.

Figure 10 furthermore presents the ice-crystal size distributions in the W and NW simulations. As mentioned previously, the size distributions of ice crystals differ significantly when wave perturbations are included or not. The small cooling rates associated with the slow ascent enable ice crystals to efficiently grow until they sediment out of the air mass, leading to a relatively narrow size distribution centered around $r \sim 10\,\mu$m. On the other hand, both the competition between the numerous ice crystals produced by large wave-induced cooling rates and the potential quenching of crystal nucleation or growth by wave-induced warm anomalies result in a wider size distribution and a smaller mean size ($r \sim 2\,\mu$m). The inclusion of horizontal mixing further reduces the size of ice crystals, but this is clearly a second-order effect in our simulations. This effect might nevertheless be more pronounced in a more realistic (less random) wave-perturbation field.

Our simulations of ice-crystal population are now compared to observations of ice particles performed during the NASA Airborne Tropical Tropopause EXperiment (ATTREX) campaign in 2014 (Jensen et al., 2013c, 2017). ATTREX collected high-resolution in-situ observations of cloud microphysics in the TTL during several flights of the Global Hawk unmanned

	Min size (μm)	Max size (μm)	Mean size (μm)	Mean concentration (/L)	Mean mass (μg)	Cloud fraction (%)
no wave (NW)	2.5	18	9.3	0.1	58	0
waves (W)	0.3	13	1.6	1385	0.5	98

Table 2. Characteristics of ice crystals produced in the simulations with or without gravity waves. The cloud fraction is defined as the fraction of time where $N_{ice} > 10\,L^{-1}$.

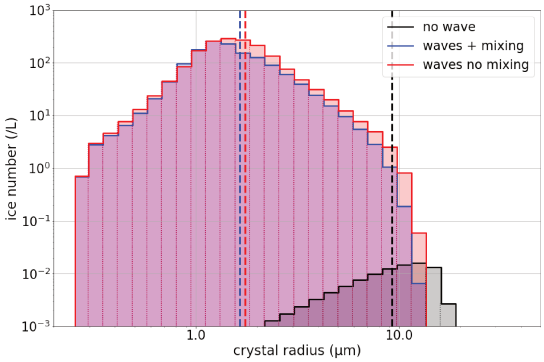

Figure 10. Ice-crystal size distributions in the (black) no-wave, (red) wave, and (blue) wave and mixing simulations. The mean size of each distribution is shown by vertical bars of the corresponding color.

aerial vehicle. The flights were performed out of Guam (13°N, 144°E), in the western Pacific, and lasted for $13-19$ hr at a maximum altitude of ~ 18 km. In this study, we will compare our simulation results with the tropical part of the transit flight from California to Guam on January 16^{th}, as well as flights on February 12^{th}, March 4^{th} and 6^{th} that sample various types of TTL cirrus. On March 4^{th}, the TTL was perturbed by the nearby presence of tropical cyclone Faxai, even though the Global Hawk did not sample the direct outflow of the cyclone (Jensen et al., 2017). In ATTREX flights, cloud properties were first measured with the Fast Cloud Droplet Probe (FCDP) spectrometer. The FCDP measures the forward scattered laser light from each cloud particle present in the sampling volume and deduces the size of the cloud particles from 1 to 50 μm diameter (Lance et al., 2010). We also compare our simulations with observations obtained by the 2D-S stereo probe (Lawson et al., 2006) during the first flight of the ATTREX deployment. 2D-S measures particles with radii between 2.5 and 1,500 μm, but we have limited the comparison to the first two 2D-S bins, respectively associated with a mean radius of 5 and 10 μm. Only the 10 last hours of simulation are used for the comparisons, so as to avoid any effect of the initial conditions.

Ice-crystal concentrations in our simulations and in ATTREX observations are displayed in Figure 11. Note that the minimum detectable concentrations respectively are $\sim 10 L^{-1}$ and $\sim 0.1 L^{-1}$ for the FCDP and 2D-S instruments. In agreement with previous findings (e.g., Schoeberl et al., 2015), the NW simulation produces unrealistically low crystal concentrations. On the other hand, ice-crystal concentrations obtained with the W simulation shows a fair agreement with observations. The main difference lies in the overestimation of ice-crystal concentrations larger than 1,000 L^{-1} in the simulation. These large

concentrations are associated with fresh nucleation events for the largest cooling rates, which might not be easy to capture with observations. We nevertheless note that ice crystal numbers as large as $15,000\,\mathrm{L}^{-1}$ have been reported in ATTREX observations (Jensen et al., 2013a). On the other hand, the similarity of the distributions for the lower concentrations ($\mathrm{N_{ice}} < 100\,\mathrm{L}^{-1}$), which are the most frequent, is relatively surprising. It has indeed been proposed that those low concentrations could result from heterogeneous nucleation on solid ice nuclei (e.g., Jensen et al., 2013a). Our simulations seem to indicate that homogeneous nucleation may also produce such low ice-crystal concentrations with reasonable probability of occurrence, in accordance with Spichtinger and Krämer (2013).

Figure 12 displays the comparisons of ice-crystal size distribution between our simulations and FCDP observations. The results associated with the simulation without wave-induced fluctuations are not shown here because of its low crystal concentrations. In agreement with the measurable concentrations by the FCDP instrument, we have only retained air parcels with $\mathrm{N_{ice}} > 10\,\mathrm{L}^{-1}$ in the W simulation for this comparison. We note that the comparison of ice crystal size distribution should be taken cautiously as FCDP was designed for measurements of water droplets. The size retrieval actually assumes Mie scattering in spherical particles (Lance, 2012; Lance et al., 2010), and therefore bears uncertainties associated with the sizing of non-spherical ice crystals. Woods et al. (2018) nevertheless showed a tendency toward quasi-spheroid particles when particle sizes (and temperature) decrease. The simulated crystal sizes in the W simulation fall in the range of ATTREX observations, i.e. radii between 1 and 15 μm, and the distribution shapes are fairly consistent. The increased occurrence of smaller particles in the simulation might be associated with limitations of the FCDP instrument at sizes near $1\,\mu$m. On the other hand, one possible reason for the lower occurrence of $\sim 10\mu$m particles in the W simulation is the limited altitude range of this simulation, which contribute to preclude the growth of sedimenting particles.

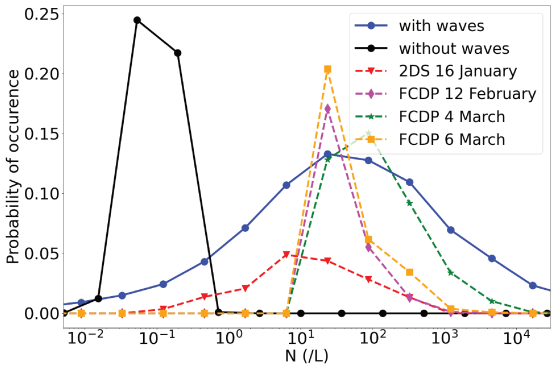

Figure 11. Comparison of ice crystal concentrations in (solid black) the NW and (solid blue) the W simulations, and (dashed) 2014 ATTREX measurements. In ATTREX measurements, the minimum detectable concentration by the FCDP and 2D-S instruments respectively are $\sim 10\,\mathrm{L}^{-1}$ and $0.1\,\mathrm{L}^{-1}$

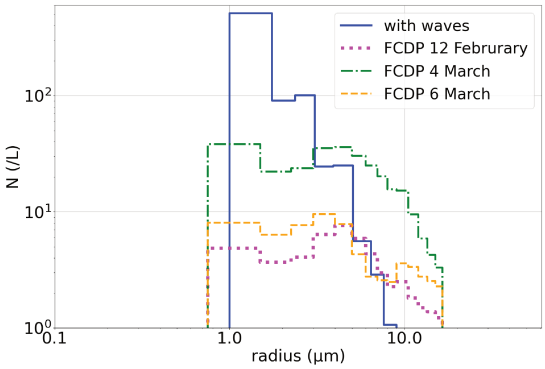

Figure 12. Comparison of ice crystal size distribution in the W simulation and in 2014 ATTREX FCDP measurements. Distributions are shown in cloud fraction only, i.e. $N_{ice} > 10\,L^{-1}$.

4.2 Air parcel dehydration

It is now commonly accepted that gravity waves likely play a role in dehydration processes in the TTL, and therefore in setting the stratospheric water vapor content (e.g., Kim and Alexander, 2015; Schoeberl et al., 2015). The primary effect of gravity waves is to lower the temperature experienced by air parcels as they ascend through the TTL. Yet, dehydration only occurs when produced ice crystals are able to sediment out of the air parcel in which they have nucleated. At low temperatures characteristic of the tropical cold point tropopause, the typical timescales of crystal nucleation, growth and sedimentation are of the same order of magnitude as gravity-wave periods. Hence, TTL dehydration results from the complex coupling of wave-induced temperature perturbations and microphysical processes, which for instance include nucleation or growth quenching (Spichtinger and Krämer, 2013; Dinh et al., 2016; Jensen et al., 2016; Schoeberl et al., 2015) and sedimentation-wave phasing (Podglajen et al., 2018). The dehydration efficiency is notably controlled by the crystal-size distribution, which critically depends on gravity-wave perturbations, as our simulations have shown.

Figure 13 displays the relative evolution of water vapor mixing ratio as a function of the final altitude of air parcels in the W simulation, i.e.:

$$\delta^{\text{rel}}_{\text{H}_2\text{O}} = \frac{X^{\text{final}}_{\text{H}_2\text{O}} - X^{\text{initial}}_{\text{H}_2\text{O}}}{X^{\text{initial}}_{\text{H}_2\text{O}}} \times 100 \tag{5}$$

where $X_{\text{H}_2\text{O}}$ stands for the water vapor mixing ratio. The mean net effect of gravity waves is to dehydrate air parcels by $\sim 5\%$ throughout the simulated altitudes, in agreement with Fig. 6. Yet, Figure 13 exhibits a large variability in dehydration at a given altitude, which results from different water vapor redistribution through nucleation and sedimentation in the different model columns. In particular, air parcels can be rehydrated as ice crystals sedimenting from above sublimate in them (Dinh et al., 2010; Murphy, 2014). In the uppermost layers of the domain though, i.e. above the mean cold-point tropopause located at

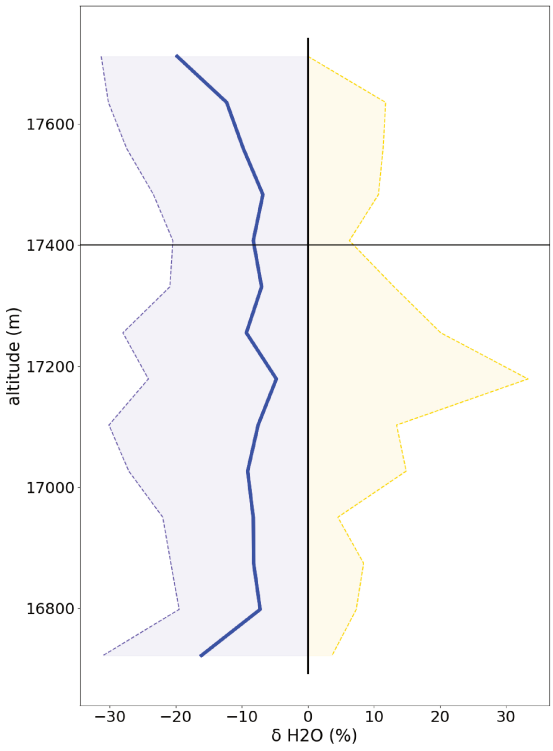

Figure 13. Relative dehydration ($\delta^{\text{rel}}_{\text{H}_2\text{O}}$) of air parcels in the W simulation: (thick) Mean dehydration, (thin) 25^{th} and 75^{th} quantiles. The altitudes shown correspond to the final altitudes of air parcels. The mean cold point is indicated by the thin horizontal line at 17.4 km. The relative dehydration in the NW simulation is hardly discernible from the 0% vertical line.

17.4 km, dehydration becomes more systematic, and the net wave-induced dehydration is increased to $\sim 20\%$. This suggests that final wave-induced dehydration events may actually occur above the climatological cold point tropopause.

Table 3 shows the observed water vapor mixing ratios in both the NW and W simulations for those of the air parcels that are above the mean cold-point tropopause at the end of the simulations, as well as mixing ratios associated with relative humidities over ice of 1 and 1.6 at the mean cold-point temperature. In the NW simulation, the mean cold-point temperature is that shown in Figure 2, i.e. $\overline{T}(17.4\,\text{km})$. In the W simulation, the mean cold-point temperature is computed as the mean of the minimum temperature experienced by each air parcel that has crossed 17.4 km (Kim and Alexander, 2015). First, no dehydration is observed in the NW simulation: the very small number of ice crystals created in this simulation were very inefficient in depleting water vapor (see Fig. 6). In this run, the stratospheric water-vapor mixing ratio (3.9 ppmv) thus corresponds to that of the air parcels initially, which was set at RHi$= 1.57$ over the whole altitude range. Because of this initial constant relative humidity, the stratospheric mixing ratio is slightly higher than that at the cold point. One may note that none of the air parcels

Simulation	$\overline{T_{\mathrm{CP}}}$ (K)	$X_{\mathrm{H_2O}}(\mathrm{RHi}=1)$ (ppmv)	$X_{\mathrm{H_2O}}(\mathrm{RHi}=1.6)$ (ppmv)	Stratospheric $X_{\mathrm{H_2O}}$ (ppmv)
NW	187.2	2.3	3.7	3.9
W	184.1	1.3	2.2	1.8

Table 3. Water vapor mixing ratios in the W and NW simulations. The stratospheric $X_{\mathrm{H_2O}}$ corresponds to the mean water vapor mixing ratio of those air parcels that are above the mean cold-point tropopause at the end of the simulation.

in which nucleation occurred have crossed the tropopause during the NW simulation, so that the real stratospheric mixing ratio would have been (very) slightly reduced in a longer run.

On the other hand when gravity waves are included, the stratospheric water-vapor mixing ratio is 1.8 ppmv . This value lies in between the extreme mixing ratios obtained with RHi=1 and RHi=1.6 at the cold point. Hence, as expected, gravity waves are not fully efficient in restoring RHi=1 at the minimum temperature experienced by the air parcels (Schoeberl et al., 2015). Yet, this water vapor mixing ratio is slightly lower than the mixing ratio corresponding to RHi=1 at the background temperature (2.3 ppmv), in agreement with the 20% increased dehydration observed in the uppermost layers of the W simulation (cf. Fig. 6). When compared to the NW case, the stratospheric water vapor mixing ratio is thus decreased by ~ 2 ppmv when gravity-wave perturbations are included. The magnitude of this systematic wave-induced dehydration is very significant, since it is for instance comparable to the seasonal variation of water vapor at the tropical tropopause (e.g. Mote et al., 1996; Davis et al., 2016).

5 Conclusions

This study aimed at investigating the effects of gravity waves on the microphysics of cirrus clouds and air parcel dehydration at the tropical tropopause layer in idealized simulations. Detailed microphysical simulations, which consider homogeneous nucleation as the sole mechanism for ice production, sedimentation and a crude treatment of horizontal mixing, have been carried out with and without gravity-wave temperature perturbations. Excerpts from quasi-Lagrangian balloon-borne observations in the lower tropical stratosphere are used to add gravity-wave disturbances in otherwise slowly ascending air parcels in the TTL. Two main simulations are carried out and contrasted to highlight the profoundly different outcomes in terms of microphysics, depending on the inclusion of gravity waves effects. A reference simulation represents the ascension of air parcels in the tropical tropopause layer, initially close to nucleating conditions ("NW" simulation), the second one also represents the impact of gravity wave-driven temperature variability in a non saturated environment ("W" simulation).

The "NW" simulation indicates that without wave perturbations, i.e. when only the slow ascent of air parcels in the TTL is responsible for nucleation events, ice crystal concentrations are unrealistically low. Similarly, the ice-crystal size distribution is too narrow, and peaks at a radius of 9 μm, which is too large when compared to observations. Lastly, the "NW" simulation is associated with almost zero dehydration in the vicinity of the cold-point tropopause, despite initial conditions close to the homogeneous nucleation threshold.

The inclusion of gravity waves significantly modifies the production of ice crystals in the simulation. This is notably due to the much larger cooling/heating rates produced by gravity waves. The more numerous nucleation events in the wave simulation contribute to efficiently restoring the relative humidity over ice to equilibrium with respect to the background temperature profile throughout the simulated domain. A further 20% decrease in water vapor mixing ratio is observed in air parcels that have penetrated in the stratosphere. The wave-induced dehydration effect is thus estimated to ~ 2 ppmv in the vicinity of the cold-point tropopause.

Ice crystal number concentration and size distribution compare furthermore better with observations in the gravity-wave simulation, even though no cloud condensation nuclei are included in the simulations. This supports that heterogeneous nucleation might not be the only process responsible for lower ice crystals concentrations. Furthermore, this accordance highlights the importance of a realistic representation of waves to reproduce observations.

Our results bring further evidence that gravity waves may significantly increase the cloud fraction in the vicinity of the cold-point tropopause, as also suggested in, e.g., Ueyama et al. (2015) and Schoeberl et al. (2018). A precise assessment of this increase would require less idealized simulations than those carried out here. Similarly, the radiative impact of the wave-induced enhanced cloudiness is left for future work. Our results nonetheless call for a coupled treatment of TTL wave and microphysics in parameterizations used in climate models.

Data availability. The balloon-born TSEN data is part of Strateole-2 and available at https://data.ipsl.fr/catalog/strateole2/. Stratéole-2 is sponsored by CNES, CNRS/INSU, ESA and NSF. ATTREX data are available at https://espoarchive.nasa.gov/archive/browse/attrex/id4/GHawk

Author contributions. The authors confirm contribution to the paper as follows:
Formal analysis and methodology : Milena Corcos, Albert Hertzog, Aurélien Podglajen and Riwal Plougouven
Draft manuscript preparation: Milena Corcos
Writing of the original draft : Milena Corcos and Albert Hertzog
All authors reviewed the results and approved the final version of the manuscript.

Competing interests. The authors declare that they have no conflict of interest.

Acknowledgements. The authors would like to thank warmly Eric Jensen and Bernd Kärcher for thoughful discussions and suggestions during the final stage of this study, as well as Martina Bramberger, Joan Alexander and Sean Davis.

References

Bardeen, C. G., Toon, O. B., Jensen, E. J., Marsh, D. R., and Harvey, V. L.: Numerical simulations of the three-dimensional distribution of meteoric dust in the mesosphere and upper stratosphere, J. Geophys. Res., 113, https://doi.org/10.1029/2007jd009515, 2008.

Boccara, G., Hertzog, A., Vincent, R. A., and Vial, F.: Estimation of Gravity Wave Momentum Flux and Phase Speeds from Quasi-Lagrangian Stratospheric Balloon Flights. Part I: Theory and Simulations, J. Atmos. Sci., 65, 3042–3055, https://doi.org/10.1175/2008JAS2709.1, 2008.

Boehm, M. T. and Lee, S.: The Implications of Tropical Rossby Waves for Tropical Tropopause Cirrus Formation and for the Equatorial Upwelling of the Brewer–Dobson Circulation, J. Atmos. Sci., 60, 247–261, https://doi.org/10.1175/1520-0469(2003)060<0247:tiotrw>2.0.co;2, 2003.

Böhm, H. P.: A General Equation for the Terminal Fall Speed of Solid Hydrometeors, J. Atmos. Sci., pp. 2419–2427, https://doi.org/10.1175/1520-0469(1989)046<2419:ageftt>2.0.co;2, 1989.

Corcos, M., Hertzog, A., Plougonven, R., and Podglajen, A.: Observation of Gravity Waves at the Tropical Tropopause Using Superpressure Balloons, J. Geophys. Res., 126, https://doi.org/10.1029/2021jd035165, 2021.

Corti, T., Luo, B. P., de Reus, M., Brunner, D., Cairo, F., Mahoney, M. J., Martucci, G., Matthey, R., Mitev, V., dos Santos, F. H., Schiller, C., Shur, G., Sitnikov, N. M., Spelten, N., Vössing, H. J., Borrmann, S., and Peter, T.: Unprecedented evidence for deep convection hydrating the tropical stratosphere, Geophys. Res. Lett., 35, https://doi.org/10.1029/2008gl033641, 2008.

Cziczo, D. J., DeMott, P. J., Brooks, S. D., Prenni, A. J., Thomson, D. S., Baumgardner, D., Wilson, J. C., Kreidenweis, S. M., and Murphy, D. M.: Observations of organic species and atmospheric ice formation, Geophys. Res. Lett., 31, https://doi.org/10.1029/2004gl019822, 2004.

Davis, S. M., Rosenlof, K. H., Hassler, B., Hurst, D. F., Read, W. G., Vömel, H., Selkirk, H., Fujiwara, M., and Damadeo, R.: The Stratospheric Water and Ozone Satellite Homogenized (SWOOSH) database: a long-term database for climate studies, Earth Syst. Sci. Data, 8, 461–490, https://doi.org/10.5194/essd-8-461-2016, 2016.

Dinh, T. and Durran, D. R.: A hybrid bin scheme to solve the condensation/evaporation equation using a cubic distribution function, Atmos. Chem. Phys., 12, 1003–1011, https://doi.org/10.5194/acp-12-1003-2012, 2012.

Dinh, T., Podglajen, A., Hertzog, A., Legras, B., and Plougonven, R.: Effect of gravity wave temperature fluctuations on homogeneous ice nucleation in the tropical tropopause layer., Atmos. Chem. Phys., 16, 35–46, https://doi.org/10.5194/acp-16-35-2016, 2016.

Dinh, T. P., Durran, D. R., and Ackerman, T. P.: Maintenance of tropical tropopause layer cirrus, J. Geophys. Res., 115, https://doi.org/10.1029/2009jd012735, 2010.

Fueglistaler, S., Dessler, A. E., Dunkerton, T. J., Folkins, I., Fu, Q., and Mote, P. W.: Tropical tropopause layer, Rev. Geophys., 47, https://doi.org/10.1029/2008RG000267, 2009.

Gettelman, A., Salby, M. L., and Sassi, F.: Distribution and influence of convection in the tropical tropopause region, J. Geophys. Res., 107, ACL 6–1–ACL 6–12, https://doi.org/10.1029/2001jd001048, 2002.

Gettelman, A., de F. Forster, P. M., Fujiwara, M., Fu, Q., Vömel, H., Gohar, L. K., Johanson, C., and Ammerman, M.: Radiation balance of the tropical tropopause layer, J. Geophys. Res., 109, https://doi.org/https://doi.org/10.1029/2003JD004190, 2004.

Haag, W. and Kärcher, B.: The impact of aerosols and gravity waves on cirrus clouds at midlatitudes, J. Geophys. Res., 109, https://doi.org/10.1029/2004jd004579, 2004.

Hermann, M., Heintzenberg, J., Wiedensohler, A., Zahn, A., Heinrich, G., and Brenninkmeijer, C. A. M.: Meridional distributions of aerosol particle number concentrations in the upper troposphere and lower stratosphere obtained by Civil Aircraft for Regular Investigation of the Atmosphere Based on an Instrument Container (CARIBIC) flights, J. Geophys. Res., 108, n/a–n/a, https://doi.org/10.1029/2001jd001077, 2003.

Hertzog, A. and Vial, F.: A study of the dynamics of the equatorial lower stratosphere by use of ultra-long-duration balloons: 2. Gravity waves, J. Geophys. Res., 106, 22 745–22 761, https://doi.org/10.1029/2000JD000242, 2001.

Holton, J. R. and Gettelman, A.: Horizontal transport and the dehydration of the stratosphere, Geophys. Res. Lett., 28, 2799–2802, https://doi.org/10.1029/2001gl013148, 2001.

Hoyle, C. R., Luo, B. P., and Peter, T.: The Origin of High Ice Crystal Number Densities in Cirrus Clouds, J. Atmos. Sci., 62, 2568–2579, https://doi.org/10.1175/jas3487.1, 2005.

Jensen, E. J. and Pfister, L.: Transport and freeze-drying in the tropical tropopause layer, J. Geophys. Res., 109, https://doi.org/10.1029/2003jd004022, 2004.

Jensen, E. J. and Toon, O. B.: Ice nucleation in the upper troposphere: Sensitivity to aerosol number density, temperature, and cooling rate, Geophys. Res. Lett., 21, 2019–2022, https://doi.org/10.1029/94gl01287, 1994.

Jensen, E. J., Toon, O. B., Pfister, L., and Selkirk, H. B.: Dehydration of the upper troposphere and lower stratosphere by subvisible cirrus clouds near the tropical tropopause, Geophys. Res. Lett., 23, 825–828, https://doi.org/10.1029/96gl00722, 1996.

Jensen, E. J., Pfister, L., Ackerman, A. S., Tabazadeh, A., and Toon, O. B.: A conceptual model of the dehydration of air due to freeze-drying by optically thin, laminar cirrus rising slowly across the tropical tropopause, J. Geophys. Res., 106, 17 237–17 252, https://doi.org/10.1029/2000jd900649, 2001.

Jensen, E. J., Pfister, L., Bui, T.-P., Lawson, P., and Baumgardner, D.: Ice nucleation and cloud microphysical properties in tropical tropopause layer cirrus, Atmos. Chem. Phys., 10, 1369–1384, https://doi.org/10.5194/acp-10-1369-2010, 2010.

Jensen, E. J., Pfister, L., and Bui, T. P.: Physical processes controlling ice concentrations in cold cirrus near the tropical tropopause, J. Geophys. Res., 117, https://doi.org/https://doi.org/10.1029/2011JD017319, 2012.

Jensen, E. J., Diskin, G., Lawson, R. P., Lance, S., Bui, T. P., Hlavka, D., McGill, M., Pfister, L., Toon, O. B., and Gao, R.: Ice nucleation and dehydration in the Tropical Tropopause Layer, Proc. National Academy of Sci., 110, 2041–2046, 2013a.

Jensen, E. J., Lawson, R. P., Bergman, J. W., Pfister, L., Bui, T. P., and Schmitt, C. G.: Physical processes controlling ice concentrations in synoptically forced, midlatitude cirrus, J. Geophys. Res., 118, 5348–5360, https://doi.org/10.1002/jgrd.50421, 2013b.

Jensen, E. J., Pfister, L., Jordan, D. E., Fahey, D. W., Newman, P. A., Thornberry, T., Rollins, A., Diskin, G., Bui, T. P., McGill, M., et al.: The NASA Airborne Tropical TRopopause EXperiment (ATTREX), SPARC Newsletter, 41, 15–24, 2013c.

Jensen, E. J., Ueyama, R., Pfister, L., Bui, T. V., Alexander, M. J., Podglajen, A., Hertzog, A., Woods, S., Lawson, R. P., Kim, J.-E., and Schoeberl, M. R.: High-frequency gravity waves and homogeneous ice nucleation in tropical tropopause layer cirrus, Geophys. Res. Lett., 43, 6629–6635, https://doi.org/10.1002/2016GL069426, 2016.

Jensen, E. J., Pfister, L., Jordan, D. E., Bui, T. V., Ueyama, R., Singh, H. B., Thornberry, T. D., Rollins, A. W., Gao, R.-S., Fahey, D. W., Rosenlof, K. H., Elkins, J. W., Diskin, G. S., DiGangi, J. P., Lawson, R. P., Woods, S., Atlas, E. L., Rodriguez, M. A. N., Wofsy, S. C., Pittman, J., Bardeen, C. G., Toon, O. B., Kindel, B. C., Newman, P. A., McGill, M. J., Hlavka, D. L., Lait, L. R., Schoeberl, M. R., Bergman, J. W., Selkirk, H. B., Alexander, M. J., Kim, J.-E., Lim, B. H., Stutz, J., and Pfeilsticker, K.: The NASA Airborne Tropical Tropopause Experiment: High-Altitude Aircraft Measurements in the Tropical Western Pacific, Bull. Am. Meteorol. Soc., 98, 129–143, https://doi.org/10.1175/BAMS-D-14-00263.1, 2017.

Jensen, E. J., Kärcher, B., Ueyama, R., Pfister, L., Bui, T. V., Diskin, G. S., DiGangi, J. P., Woods, S., Lawson, R. P., Froyd, K. D., and Murphy, D. M.: Heterogeneous Ice Nucleation in the Tropical Tropopause Layer, J. Geophys. Res., 123, https://doi.org/10.1029/2018jd028949, 2018.

Kim, J.-E. and Alexander, M. J.: Direct impacts of waves on tropical cold point tropopause temperature, Geophys. Res. Lett., 42, 1584–1592, https://doi.org/https://doi.org/10.1002/2014GL062737, 2015.

Koop, T., Luo, B., Tsias, A., and Peter, T.: Water activity as the determinant for homogeneous ice nucleation in aqueous solutions, Nature, 406, 611–614, https://doi.org/10.1038/35020537, 2000.

Krämer, M., Schiller, C., Afchine, A., Bauer, R., Gensch, I., Mangold, A., Schlicht, S., Spelten, N., Sitnikov, N., Borrmann, S., de Reus, M., and Spichtinger, P.: Ice supersaturations and cirrus cloud crystal numbers, Atmos. Chem. Phys., 9, 3505–3522, https://doi.org/10.5194/acp-9-3505-2009, 2009.

Kärcher, B.: Properties of subvisible cirrus clouds formed by homogeneous freezing, Atmos. Chem. Phys., 2, 161–170, https://doi.org/10.5194/acp-2-161-2002, 2002.

Kärcher, B.: Simulating gas-aerosol-cirrus interactions: Process-oriented microphysical model and applications, Atmos. Chem. Phys., pp. 1645–1664, https://doi.org/10.5194/acp-3-1645-2003, 2003.

Kärcher, B.: Cirrus clouds in the tropical tropopause layer: Role of heterogeneous ice nuclei, Geophys. Res. Lett., 31, n/a–n/a, https://doi.org/10.1029/2004gl019774, 2004.

Kärcher, B. and Lohmann, U.: A parameterization of cirrus cloud formation: Homogeneous freezing of supercooled aerosols, J. Geophys. Res., 107, AAC 4–1–AAC 4–10, https://doi.org/10.1029/2001JD000470, 2002.

Kärcher, B. and Podglajen, A.: A Stochastic Representation of Temperature Fluctuations Induced by Mesoscale Gravity Waves, J. Geophys. Res., 124, 11 506–11 529, https://doi.org/10.1029/2019jd030680, 2019.

Kärcher, B., Hendricks, J., and Lohmann, U.: Physically based parameterization of cirrus cloud formation for use in global atmospheric models, J. Geophys. Res., 111, https://doi.org/10.1029/2005jd006219, 2006.

Kärcher, B., Jensen, E. J., and Lohmann, U.: The Impact of Mesoscale Gravity Waves on Homogeneous Ice Nucleation in Cirrus Clouds, Geophys. Res. Lett., 46, 5556–5565, https://doi.org/10.1029/2019GL082437, 2019.

Lance, S.: Coincidence Errors in a Cloud Droplet Probe (CDP) and a Cloud and Aerosol Spectrometer (CAS), and the Improved Performance of a Modified CDP, J. Atmos. Oceanic Technol., 29, 1532–1541, https://doi.org/10.1175/jtech-d-11-00208.1, 2012.

Lance, S., Brock, C. A., Rogers, D., and Gordon, J. A.: Water droplet calibration of the Cloud Droplet Probe (CDP) and in-flight performance in liquid, ice and mixed-phase clouds during ARCPAC, Atmos. Meas. Tech., 3, 1683–1706, https://doi.org/10.5194/amt-3-1683-2010, 2010.

Lawson, R. P., O'Connor, D., Zmarzly, P., Weaver, K., Baker, B., Mo, Q., and Jonsson, H.: The 2D-S (Stereo) Probe: Design and Preliminary Tests of a New Airborne, High-Speed, High-Resolution Particle Imaging Probe, J. Atmos. Oceanic Technol., 23, 1462–1477, https://doi.org/10.1175/JTECH1927.1, 2006.

McFarquhar, G. M., Heymsfield, A. J., Spinhirne, J., and Hart, B.: Thin and Subvisual Tropopause Tropical Cirrus: Observations and Radiative Impacts, J. Atmos. Sci., 57, 1841–1853, https://doi.org/10.1175/1520-0469(2000)057<1841:tasttc>2.0.co;2, 2000.

Mote, P. W., Rosenlof, K. H., McIntyre, M. E., Carr, S. E., Gille, J. C., Holton, J. R., Kinnersley, J. S., Pumphrey, H. C., Russell III, J. M., and Waters, J. W.: An atmospheric tape recorder: The imprint of tropical tropopause temperatures on stratospheric water vapor, J. Geophys. Res., 101, 3989–4006, https://doi.org/https://doi.org/10.1029/95JD03422, 1996.

Murphy, D. M.: Rare temperature histories and cirrus ice number density in a parcel and a one-dimensional model, Atmos. Chem. Phys., 14, 13 013–13 022, https://doi.org/10.5194/acp-14-13013-2014, 2014.

Nastrom, G. D.: The Response of Superpressure Balloons to Gravity Waves, J. Applied Meteo., pp. 1013–1019, https://doi.org/10.1175/1520-0450(1980)019<1013:trosbt>2.0.co;2, 1980.

Pfister, L., Selkirk, H. B., Jensen, E. J., Schoeberl, M. R., Toon, O. B., Browell, E. V., Grant, W. B., Gary, B., Mahoney, M. J., Bui, T. V., and Hintsa, E.: Aircraft observations of thin cirrus clouds near the tropical tropopause, J. Geophys. Res., 106, 9765–9786, https://doi.org/10.1029/2000jd900648, 2001.

Podglajen, A., Hertzog, A., Plougonven, R., and Legras, B.: Lagrangian temperature and vertical velocity fluctuations due to gravity waves in the lower stratosphere, Geophys. Res. Lett., 43, 3543–3553, https://doi.org/10.1002/2016GL068148, 2016.

Podglajen, A., Plougonven, R., Hertzog, A., and Jensen, E.: Impact of gravity waves on the motion and distribution of atmospheric ice particles, Atmos. Chem. Phys., pp. 10 799–10 823, https://doi.org/10.5194/acp-18-10799-2018, 2018.

Randel, W. J. and Jensen, E. J.: Physical processes in the tropical tropopause layer and their roles in a changing climate, Nature Geoscience, 6, 169–176, https://doi.org/10.1038/ngeo1733, 2013.

Salby, M. and Callaghan, P.: Control of the Tropical Tropopause and Vertical Transport across It, J. Climate, 17, 965–985, https://doi.org/10.1175/1520-0442(2004)017<0965:cottta>2.0.co;2, 2004.

Schiller, C., Grooß, J.-U., Konopka, P., Plöger, F., dos Santos, F. H. S., and Spelten, N.: Hydration and dehydration at the tropical tropopause, Atmos. Chem. Phys., 9, 9647–9660, https://doi.org/10.5194/acp-9-9647-2009, 2009.

Schoeberl, M. R., Dessler, A. E., Wang, T., Avery, M. A., and Jensen, E. J.: Cloud formation, convection, and stratospheric dehydration, Earth and Space Science, 1, 1–17, https://doi.org/10.1002/2014ea000014, 2014.

Schoeberl, M. R., Jensen, E. J., and Woods, S.: Gravity waves amplify upper tropospheric dehydration by clouds, Earth and Space Sci., 2, 485–500, https://doi.org/10.1002/2015ea000127, 2015.

Schoeberl, M. R., Jensen, E. J., Pfister, L., Ueyama, R., Avery, M., and Dessler, A. E.: Convective Hydration of the Upper Troposphere and Lower Stratosphere, Journal of Geophysical Research: Atmospheres, 123, 4583–4593, https://doi.org/https://doi.org/10.1029/2018JD028286, 2018.

Smith, W. L., Ackerman, S., Revercomb, H., Huang, H., DeSlover, D. H., Feltz, W., Gumley, L., and Collard, A.: Infrared spectral absorption of nearly invisible cirrus clouds, Geophys. Res. Lett., 25, 1137–1140, https://doi.org/10.1029/97gl03491, 1998.

Solomon, S., Garcia, R. R., Rowland, F. S., and Wuebbles, D. J.: On the depletion of Antarctic ozone, Nature, 321, 755–758, https://doi.org/10.1038/321755a0, 1986.

Solomon, S., Rosenlof, K. H., Portmann, R. W., Daniel, J. S., Davis, S. M., Sanford, T. J., and Plattner, G.-K.: Contributions of Stratospheric Water Vapor to Decadal Changes in the Rate of Global Warming, Science, 327, 1219–1223, https://doi.org/10.1126/science.1182488, 2010.

Spichtinger, P. and Gierens, K. M.: Modelling of cirrus clouds – Part 1b: Structuring cirrus clouds by dynamics, Atmos. Chem. Phys., 9, 707–719, https://doi.org/10.5194/acp-9-707-2009, 2009.

Spichtinger, P. and Krämer, M.: Tropical tropopause ice clouds: a dynamic approach to the mystery of low crystal numbers, Atmos. Chem. Phys., 13, 9801–9818, https://doi.org/10.5194/acp-13-9801-2013, 2013.

Toon, O. B., Turco, R. P., Westphal, D., Malone, R., and Liu, M.: A Multidimensional Model for Aerosols: Description of Computational Analogs, J. Atmos. Sci., 45, 2123–2144, https://doi.org/10.1175/1520-0469(1988)045<2123:ammfad>2.0.co;2, 1988.

Toon, O. B., Turco, R. P., Jordan, J., Goodman, J., and Ferry, G.: Physical processes in polar stratospheric ice clouds, J. Geophys. Res., 94, 11 359, https://doi.org/10.1029/jd094id09p11359, 1989.

Ueyama, R., Jensen, E. J., Pfister, L., and Kim, J.-E.: Dynamical, convective, and microphysical control on wintertime distributions of water vapor and clouds in the tropical tropopause layer, Journal of Geophysical Research: Atmospheres, 120, 10,483–10,500, https://doi.org/https://doi.org/10.1002/2015JD023318, 2015.

Vincent, R. A. and Hertzog, A.: The response of superpressure balloons to gravity wave motions, Atmos. Meas. Tech., 7, 1043–1055, https://doi.org/10.5194/amt-7-1043-2014, 2014.

Winker, D. M. and Trepte, C. R.: Laminar cirrus observed near the tropical tropopause by LITE, Geophys. Res. Lett., 25, 3351–3354, https://doi.org/10.1029/98gl01292, 1998.

Woods, S., Lawson, R. P., Jensen, E., Bui, T. P., Thornberry, T., Rollins, A., Pfister, L., and Avery, M.: Microphysical Properties of Tropical Tropopause Layer Cirrus, J. Geophys. Res., 123, 6053–6069, https://doi.org/10.1029/2017jd028068, 2018.

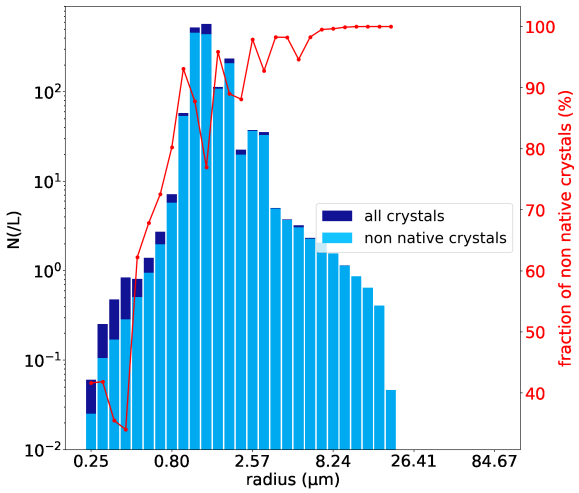

Figure 3.9: Mean ice crystals population for the S0 and S1 simulation

Table 3.1: Ice production for simulation "S0" and "S1".

	Min size (μm)	Max size (μm)	Mean size (μm)	Mean concentration (/L)	Mean mass (μg)	Cloud fraction (%)
S0	0.25	14	1.4	240	3.6	27
S1	0.25	24	1.6	1631	72	95

3.4 Comparison of the represented cirrus clouds to measurements.

In the last part of the paper, we compare statistical distributions of ice crystals densities and ice crystal populations represented by our model in the presence of gravity waves ("W" and "WSx" simulations) with ATTREX measurements. In this section, we compare the cirrus structure in space and its evolution. Figure 3.10 represents the evolution of ice mass in the simulated domain (420 air parcels, distributed among 6 columns, with a thickness of 15 m and a width of 150 m) every two hours for the "W" simulation. As a reminder, RH_i is set to 1 for the whole setup as initial condition. The beginning of the simulation (up to 4 hours) is characterised by scattered nucleating layers, located at the coldest anomalies, which thicken with the sedimentation of the largest ice crystals. These layers are typically of 20 to 50 m, and contain the largest amount of ice mass. They disappear at different times as the simulation moves forward, from complete sedimentation and/or sublimation of ice crystals in non saturated environment. Overall, as previously seen in the article, the cloud structure formed is complex and wide, with nucleation at various levels of altitude at different times.
We selected two vertical profiles that represent the vertical structure of the simulated cloud, to compare them with two ATTREX flights and BeCOOL measurements. The ATTREX flight chosen was from November 5 to 6, and November 9, 2011, in the eastern Pacific ($\approx$

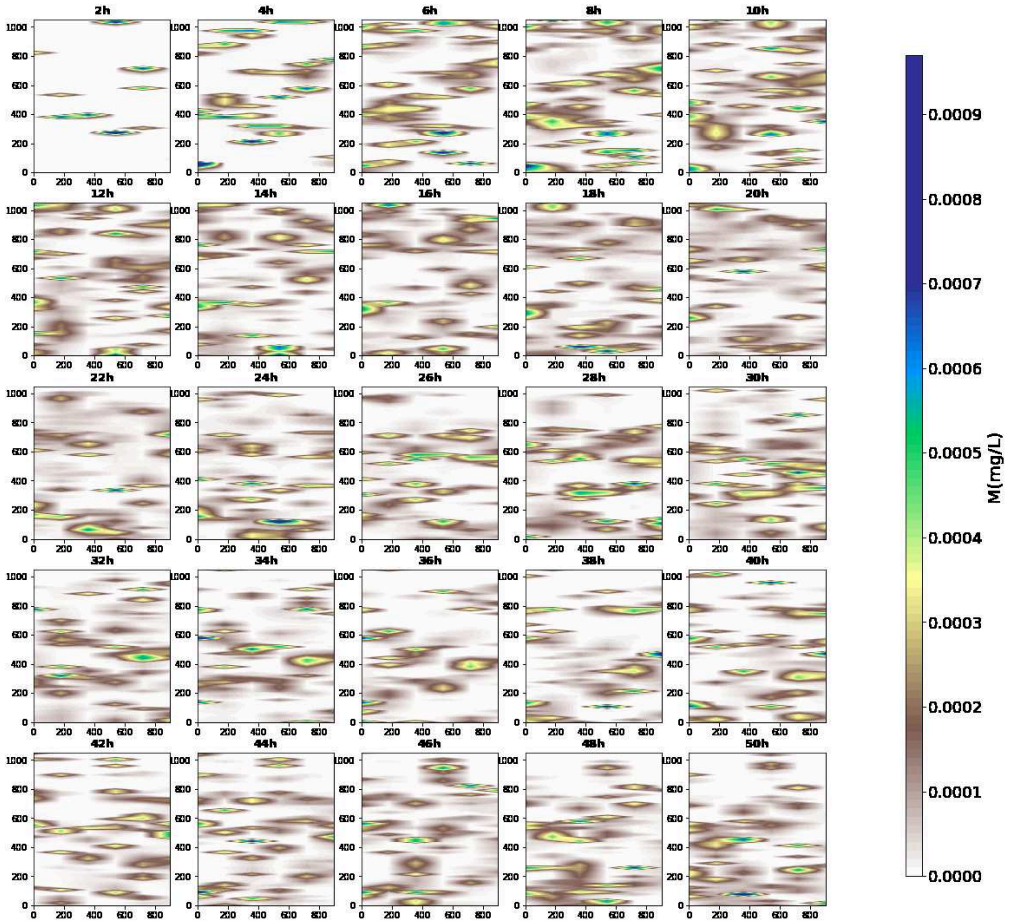

Figure 3.10: Time lapse of the ice mass contained in the setup every two hours of the "W" simulation.

125°W and 11°N). The Global Hawk flew between 15.5 and 17 km in a cold anomaly of the TTL with an intense wave activity (Jensen et al., 2013). The BeCOOL measurement is from the 1st Stratéole-2 campaign, in fall 2021. It is an embedded lidar carried by the balloon ST2_C1_13_STR1. It therefore gives Lagrangian measurements, with a 10 min ON 10 min OFF cycle. The measurements chosen were at -4N, 208E, the 30th of December 2021.

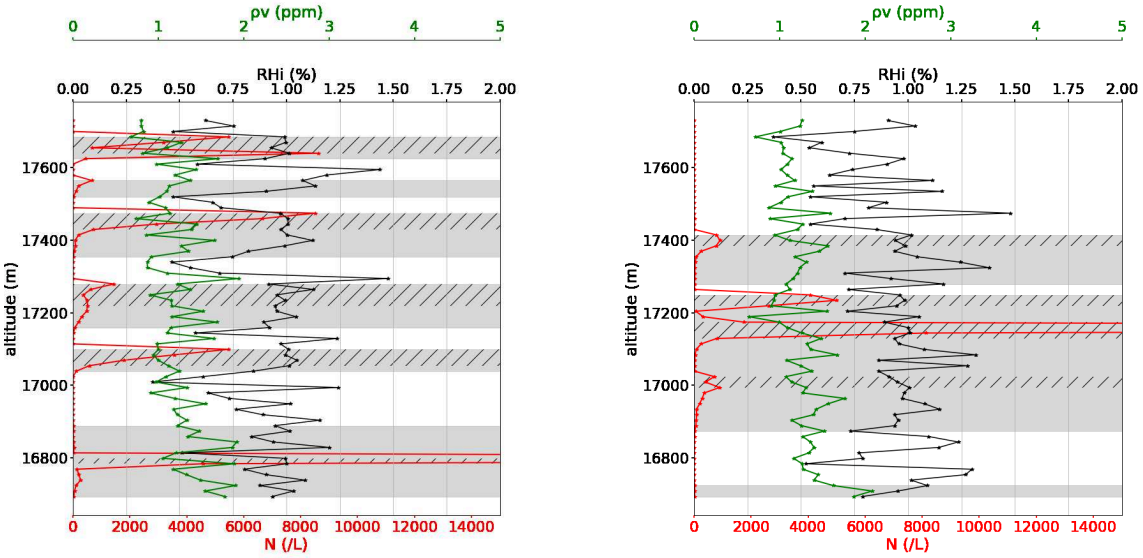

(a) Profile at 44 hours, from the 3rd column of the domain in the "W" simulation.

(b) Profile at 44 hours, from the 5th column of the domain in the "W" simulation.

Figure 3.11: Vertical profiles of RH_i (black) ρ_v (green) and ice number (red). Grey areas for $N \geq 15/L$, hatched for $N \geq 500/L$.

Figure 3.11a, 3.11b displays the vertical profile of RH_i, ρ_v and N the ice concentration at the end of the simulation ($\approx$ 44 h) for two different columns of the setup. Like ATTREX profiles in figure 3.13 lower panel, we find a supersaturation above the cloud (in grey), and a drop of RH_i to unity inside the cloud fraction, fluctuating from the temperature variations. Moreover, our profiles show a stabilisation of $RH_i \sim 1$ for high densities of ice crystals (>500/L). This can be explained with a timescale for water vapor removal by ice crystal growth in a supersaturated environment of around a few minutes for these high concentrations. Note that this ATTREX flight was in a supersaturated environment, whereas our simulations started with RH_i=1.

This ice crystals effect on RH_i is further described by figure 3.12 that displays the distribution of RH_i for various ice densities in the simulation with waves. It highlights a return

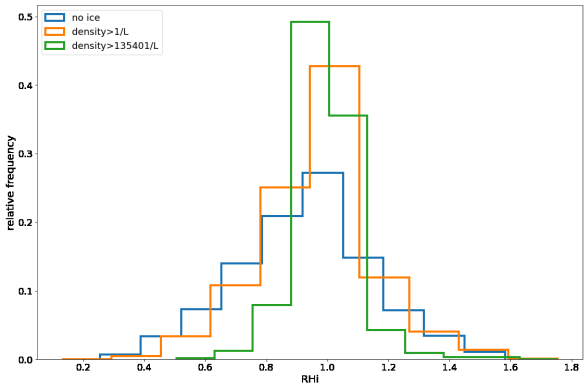

Figure 3.12: Distributions of RH_i in the simulation "W" for different ice crystals densities. The green curve represents the 75e quantile.

to equilibrium (RH_i=1) for higher ice densities, as well as the presence of ice in an under saturated environment (RH_i<1).

Regarding the dehydration of air parcels, the water vapor mixing ratio in ATTREX profiles is pretty stable (figure 3.13), dropping of around 2 ppm in the cloud fraction as ice crystals deplete humidity. Conversely, the simulated mixing ratio profile is very noisy and does not show a clear difference of behavior in and out of the cloud fraction. It is a limitation of our model that sets an initial profile already disrupted by the waves.

For the overall structure of the cloud, ATTREX profiles display varying thickness of cloud fractions measured with low ice concentration in altitude (from 1200 m in the upper panel to 50 m in the lower panel) and narrow layers with higher ice crystal number concentrations of around 1000/L. The simulated cloud structure has a wider vertical extension, embedding very localized ice pockets of ice concentrations of a few tens of meters (grey or dashed bands). One obvious limitation of our simulation is the random character of cirrus clouds occurrences in the vertical. Observations on the other hand are more structured in the TTL. This is illustrated in figure 3.14a and 3.14b, that both describe a thin cirrus (around 100 m thick) homogeneous in space, at two different levels of altitude, that contradicts the structure of our simulated clouds.

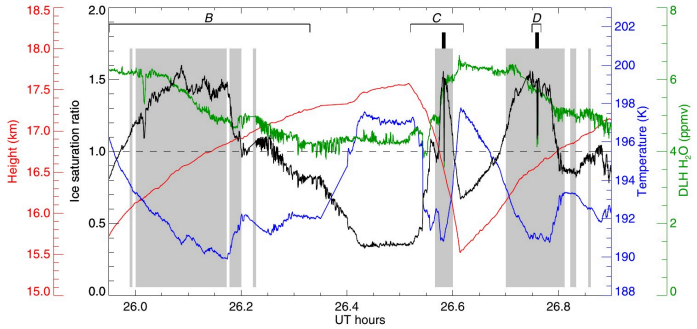

(a) Time series of in situ measurements during ascents and descents through the TTL of Global Hawk. Grey shading indicates when ice was detected, and black bars denote high ice concentrations (N > 200/L).

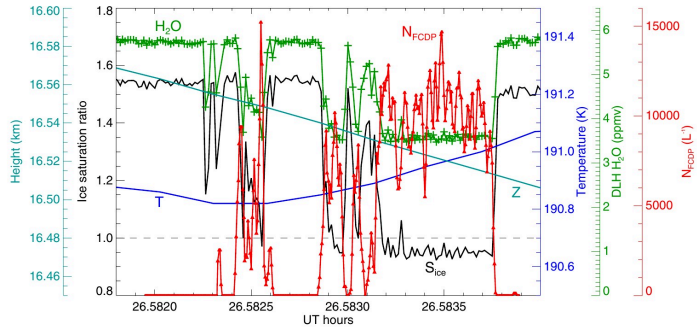

(b) Expansion of the time period labeled C in the upper panel with 0.05s time resolution.

Figure 3.13: ATTREX profiles. Note that the comparison with our altitude profiles should be read by following the plane's altitude in time (red curve upper panel, cyan curve lower panel).

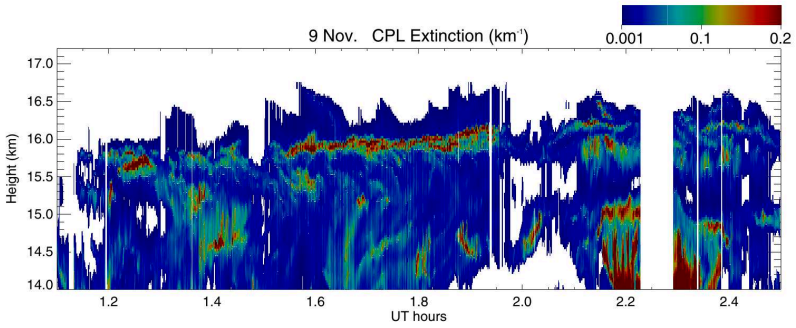

(a) Measured extinction in time and height indicated by the nadir-looking CPL (Cloud Physics Lidar). Flight segment on November 9. Narrow layers with high extinction are embedded in broader layers with low extinction.

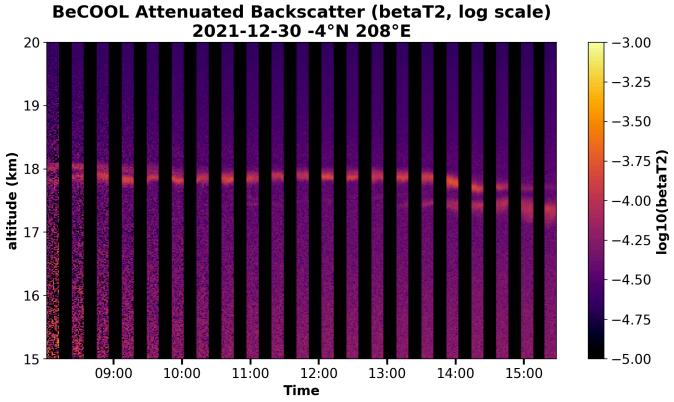

(b) BeCOOL lidar observation (attenuated backscatter in time and altitude) from ST2_C1_13_STR1 flight during boreal winter 2021. A persistent and thin cirrus cloud without underneath clouds.

Figure 3.14: Lidar measurements of cirrus clouds from ATTREX airborn and Stratéole-2 balloon.

Chapter 4

Sensitivity tests : temperature fluctuations variability and amplitude

Sommaire

4.1 Correlation of temperature fluctuations in the simulated domain

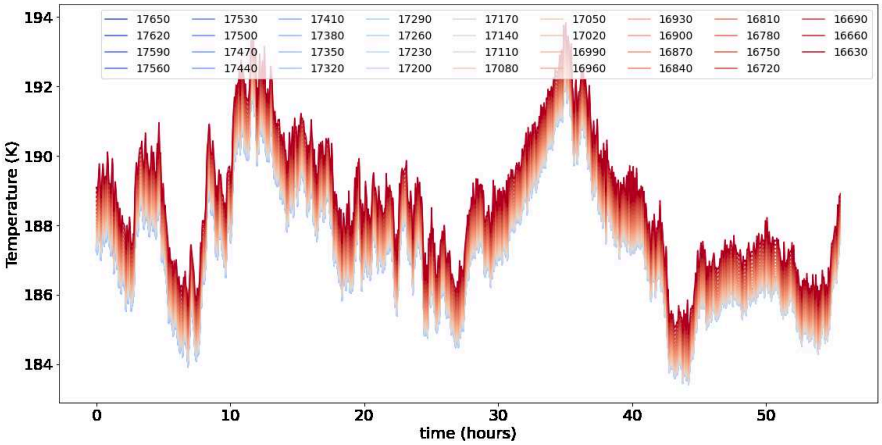

Figure 4.1: Temperature time series for different air parcels of the setup. Each one is labelled with its initial altitude. Note the evolution of $\bar{T}$ with altitude, extrapolated from the radiosonde profile of Kärcher et al. (2019). Note also the amplitude of the temperature perturbations, up to 10K between 25 and 35h of simulation.

In our paper, the W simulation maximized the variability of the temperature fluctuations by picking randomly time series of temperature fluctuations in each air mass. In other words, these temperature fluctuations were uncorrelated from one air parcel to the other. The generated cloud structure was thick, spreading over the whole simulation domain, and particles were present throughout the simulation duration. Comparison to observations (3.4) showed that despite a good statistical representation of the ice production, the vertical profile of the represented cirrus clouds was not satisfactory. In order to explore the importance of this simplification, we describe in this chapter an opposite simulation setup: time series of temperature fluctuations correlated between all air masses. Gravity waves have horizontal spatial scales of 1 to a few thousands of km, and a vertical scale of 10 m to 10 km. We therefore represent the domain with the same geometry as before (see table 1: Table of simulation definitions in the paper section 3.3) and initialized it with RH_i=1, but here the time series of wave-induced temperature fluctuations are the same for all air parcels (figure 4.1). This simulation is named STS for Single Time Serie. As a reminder, we still do not take into account disturbances induced by planetary waves.

Figures 4.2 display the evolution of the ice mass and number in time and altitude during this new experiment. Homogeneous cloud fractions are created, more scattered in time than in the "W" simulation. The first two nucleation events are terminated by a warm temperature fluctuation, and the last one produces the highest crystal density because it is associated with the coldest perturbation of the simulation. Aside from the effect of sedimentation between air layers, the occurrence and characteristics of these cloud fractions, in terms of ice crystal concentration and size will be very dependent on the history of the details of the time series

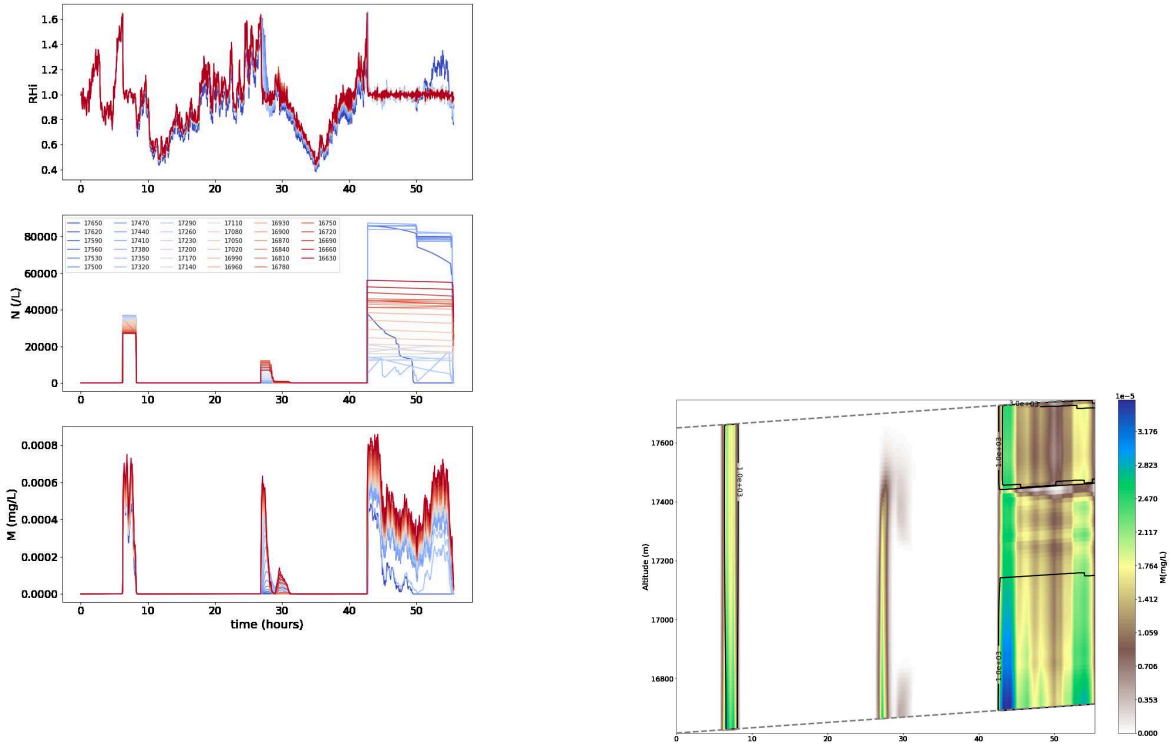

Figure 4.2: (left) Evolution of RH_i (upper panel), crystals number (middle panel) and ice mass (lower panel) for air parcels at different altitudes during the simulation. (right) Evolution of ice mass, averaged over the simulated domain, in time and altitude. Contours are crystals concentrations /L.

of T'. Indeed, the evolution in time of RH_i of each air mass is superimposed until the first nucleation event (which will produce an almost identical number of crystals, as seen on the contours of concentration on figure 4.2). The slight difference between the crystals created as a function of altitude (and temperature) becomes more pronounced when a new nucleation event takes place: the ice production (N and M, shown in the lower panels) is more different with altitude during the 3rd nucleation event where the lowest air masses (red) have enough crystals to dampen the temperature-related fluctuations in RH_i, which would prevent further nucleation, whereas higher (blue) ones do not.

Ice crystals population Regarding the ice crystal population created in STS, figure 4.3 displays a narrow distribution, peaking at 2 microns of radius. The widest crystal size distribution is created during the 2nd nucleation event, correlated with a lower crystal concentration explained by a lower cooling rate triggering nucleation. Except during this event located at about 17400 m altitude, the largest crystals come from sedimentation, they are located at the bottom of the setup and are responsible for the maximum ice mass (figure 4.2).

The created cloud fraction is lowered to 30% in the STS simulation but the ice-crystal population produced is otherwise similar to the W simulation (table 4.1).

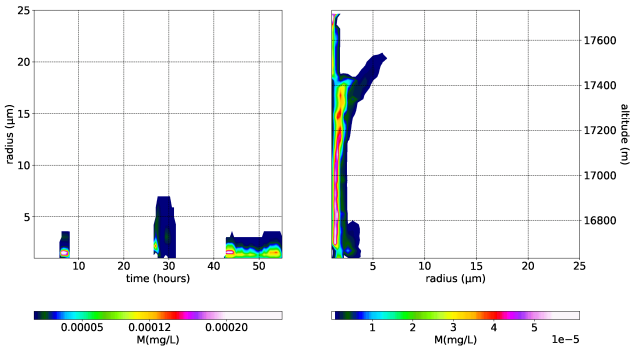

Figure 4.3: Evolution of ice crystals population in time (left panel) and altitude (right panel). Only bins filled with more than 1 crystal per cubic meter are filled.

Table 4.1: Ice production comparison between the W and STS simulations. The cloud fraction is calculated as in the article of the previous section, it is the fraction of time where N_{ice}>10/L.

	Min size (μm)	Max size (μm)	Mean size (μm)	Mean concentration (/L)	Mean mass (μg)	Cloud fraction (%)
'STS'	0.25	6.97	1.2	1521	0.1	30
'W'	0.3	13	1.6	1385	0.5	98

4.2 Sensitivity to the wave amplitude

We have seen in the first part of the thesis that the amplitude of the gravity-wave momentum fluxes, as well as the temperature variance, varied with the distance to the convection. This last section is thus devoted to the study of the sensitivity of ice crystal population to wave amplitude. As shown in section 3.1, cooling rates determine the initial concentration of ice crystals in homogeneous nucleation, and thus are a key driver of the whole life cycle of cirrus clouds. The cooling rates are proportional to the amplitude of the wave and to the intrinsic frequency $\hat{\omega}$.
The impact of wave frequencies has already been investigated: Dinh et al. (2016) and Jensen et al. (2016) for instance have shown that higher-frequency waves are associated with higher cooling rates, which increases the ice concentration. Conversely, when the wave period is close to the nucleation timescale, the effect is rather to limit this concentration: the warm phase of the wave-induced temperature fluctuation can halt the nucleation, producing a so-called "quenched event" of nucleation (Jensen et al., 2010; Spichtinger and Krämer, 2013). However, this effect has been shown to be rather minor compared to the increase of overall ice production coming from high frequency waves (Jensen et al., 2016).

The impact of the wave amplitudes has less been looked at. One can expect the same impact as the frequency in the sense that an increase in amplitude will increase the corresponding

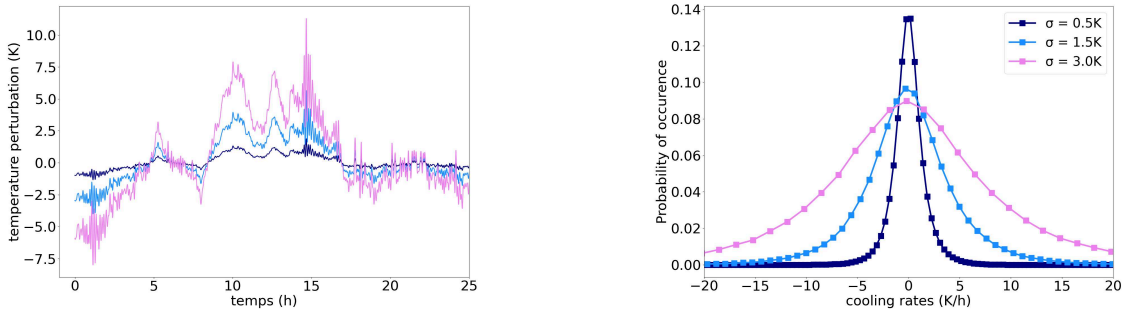

(a) 25 h long sample of temperature timeseries with the three different standard deviations.

(b) Distributions of the cooling rates in these simulations.

Figure 4.4: Temperature variability of the simulations with controlled temperature standard deviation.

generated cooling rates, but we keep here the whole spectrum of gravity waves, which is more realistic.

We have therefore performed 3 new simulations that use the balloon-borne observations of temperature, which fluctuations have a standard deviation (σ) of 1.5 (see section 3.3). However in the W simulation, σ can slightly vary from one air mass to the other depending on the sample used and its duration. Here, we constrain σ for each sample to three different standard deviations, respectively 0.5, 1.5 and 3 K (figure 4.4a). The corresponding cooling rates are shown in figure 4.4b, and display a respective increase of their widths with increasing σ. The setup geometry used is identical to that presented in the article: 420 air masses, distributed on 6 columns (see table 1: Table of simulation definitions in the paper section 3.3), and a wind shear of 10 m/s/km is used. All air masses are initialized with $RH_i = 1$.

Ice production The comparison of ice production in the different simulations (table 4.2 and figure 4.5) shows first that a standard deviation of only 0.5 K associated with cooling rates below 5 K/h is sufficient to nucleate ice in a non supersaturated environment (RH_i=1). Second, there is as expected an increase in the concentration of ice crystals with the wave amplitude, associated with the corresponding increase in cooling rates. This also is associated with the increase of the cloud fraction and the increase of the ice mass. Table 4.2 displays an increase of the average ice mass for higher σ, associated with a shift of the average size towards the bigger sizes (figure 4.5). The simulation with σ=0.5 K gives results close to the case without waves detailed in the paper. Conversely, there is only little difference in ice crystal population between 1.5 to 3 K standard deviation. Note that the smaller maximum size in the 0.5 K simulation is explained by the randomness of the temperature fluctuations. Indeed, the evolution of ice mass (figure 4.6) displays only 3 main nucleation events, and two of them are in the lower half of the simulated domain. The crystals are certainly less numerous and can therefore grow larger, but it is during their sedimentation that their size increases the most (section 3.2). Here RH_i is initialized at 1, contrary to the simulation without waves (NW), the crystals migrate in a non-supersaturated environment and can not reach the size of the NW simulation. Lastly, note that the crystals nucleated at the top of the setup are

Table 4.2: Ice production for the different wave amplitudes.

	Min size (μm)	Max size (μm)	Mean size (μm)	Mean concentration (/L)	Mean mass (μg)	cloud fraction (%)
σ = 0.5 K	0.35	12	2.7	2.7	0.43	12
σ = 1.5 K	0.3	13	1.8	1505	83	97
σ = 3 K	0.25	13	1.6	7463	225	98

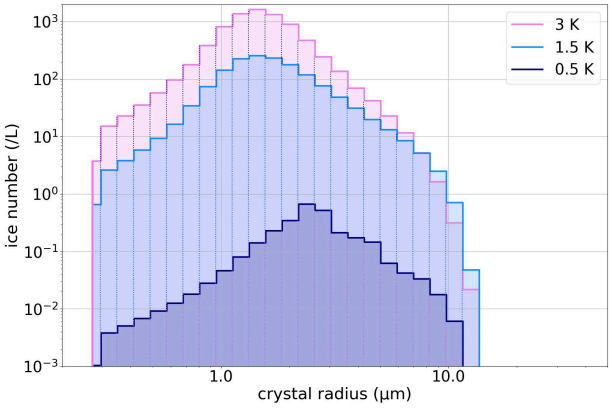

Figure 4.5: Comparison of ice crystal populations between the 3 simulations with constrained standard deviations.

quickly sublimated, with a warm temperature variation: the less nucleation events generated by the waves, the more the characteristics of the cirrus will depend on the details of the time series of temperature fluctuation. Many nucleation (or many simulations) events would be necessary to obtain more statistics robustness.

On the other hand, the evolution of ice mass with altitude and time for the 0.5 K simulation (figure 4.6) shows perhaps a case closer to the observations with more scattered and fine cloud fractions. One way to look at it is that gravity waves fluctuations are superposed on the temperature fluctuations associated with planetary waves, whose amplitude is larger and will create the supersaturation. The gravity-wave impact would therefore be reduced. The 0.5 K simulation thus somehow illustrates what could TTL cirrus look like in a dynamical field dominated by large-scale structures and where the effect of gravity-waves is less prominent.

Comparison to observations At last, comparison of the simulated ice production to ATTREX measurements (figure 4.7a) shows a significant difference between the ice density described in the W simulation described in the previous section (paper), which had on average a standard deviation of 1.5 K, and the one here with a constrained σ of 1.5 K. The latter increases the occurrence of densities between 1 and 100 crystals/L, but slightly decreases the occurrence of larger numbers of crystals. The few wave events with the highest amplitude are responsible for these large concentrations and were removed. This new ice concentration

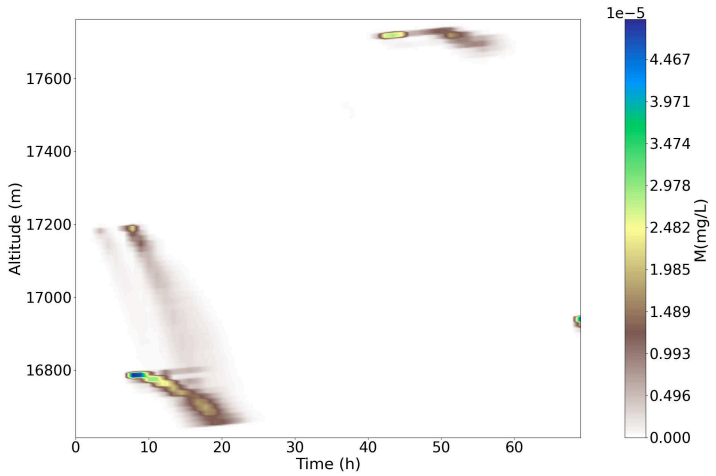

Figure 4.6: Evolution of ice mass (/L) in time and altitude for the simulation with $\sigma = 0.5$ K.

distribution fits even better the observations. The simulation with $\sigma = 3$ K fits well the low-concentration events but overestimates completely the large ones. On the contrary, with σ= 0.5 K the occurrences of large crystal concentrations measured by 2DS are well represented. Note however that the 2DS instrument is unable to detect crystals with a $r \leq 5\mu$m, which are responsible for these large concentrations. Finally, the comparison of ice crystal population with ATTREX measurements is described figure 4.7b. The crystal population does not vary much between the $\sigma = 1.5$ K and $\sigma = 3$ K simulation. Both simulations tend to overestimate the observed number of crystals between $r = 1$ and $r = 5$ microns. On the other hand, the simulation with 0.5 K completely misses the large crystals, as explained above.

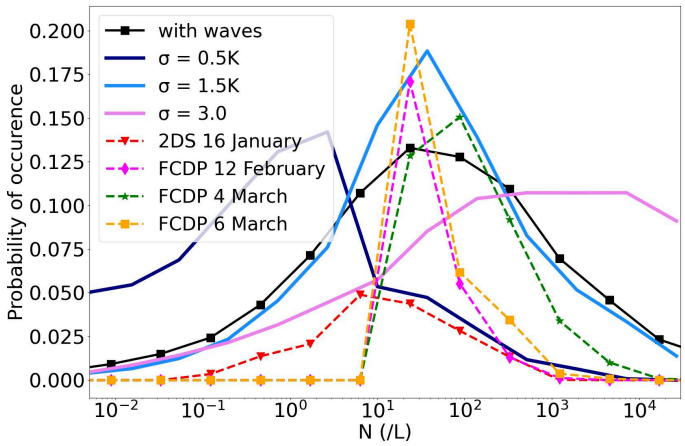

(a) Comparison of ice crystal concentrations in our simulations (solid lines) and (dashed) 2014 ATTREX measurements. In ATTREX measurements, the minimum detectable concentration by the FCDP and 2DS instruments respectively are $\approx$ 10 /L and 0.1 /L.

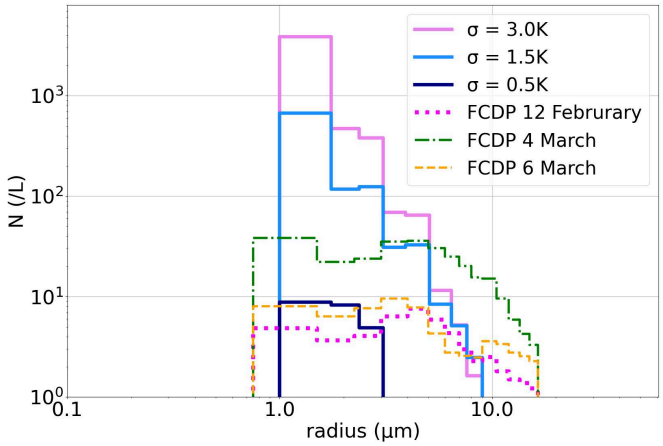

(b) Comparison of ice crystal population in the different simulations (solid lines) and in 2014 ATTREX FCDP measurements. Distributions are shown in cloud fraction only, i.e. $N_{ice} > 10$ /L.

Figure 4.7: Comparison of ice production to ATTREX observations.

Chapter 5

Conclusions and perspectives

Sommaire

This thesis was carried out to learn more about the impact of dynamic processes on tropical in-situ cirrus clouds life cycle, using the Stratéole-2 observations. Stratéole-2 provides a very rich dataset that was proven to be useful to study tropical gravity waves, by enabling direct momentum fluxes calculation in an intrinsic framework, and by resolving the whole gravity waves spectrum. The impact of these small scales waves on the mean flow is still poorly resolved in climate models, only represented by parameterizations that need more observational constraints. This motivated the first part of the thesis, which also allowed us to better understand the observations, describe the context of formation of these waves and their characteristics in the tropics, before looking at their impacts on microphysics.
Second, the clouds direct radiative effects and feedback on the circulation are only poorly represented in climate models and stand as prevalent in the uncertainties to predict a changing climate. In addition, in-situ observations are still too sparse to provide a complete view of cloud life cycles (Bony et al., 2006). At last, regarding cirrus clouds formed in-situ, one main uncertainty comes from the temperature variability generated by the gravity waves.
Stratéole-2 observations combined with a microphysics representation thus provides a good frame for a step towards a better understanding of cirrus clouds life cycle, that will be useful for further assessment of their radiative impact. As many variables are at stake, we decided to provide simple experiments to assess the interplay of dynamics with microphysical processes. This motivation led to the second and third chapter of the thesis.

5.1 Observation of gravity-wave activity at the TTL

The first chapter of the thesis focuses on the tropical gravity wave activity using the observations of Stratéole-2. A first question raised was to determine how the observed activity of gravity waves is related to tropical deep convection, at synoptic and planetary scale.
The balloons flew for more than 600 days during the two first campaigns that took place in 2019 (C0) and 2021 (C1). They followed the air masses in a quasi-Lagrangian frame, measuring pressure and temperature with a temporal resolution of 30 s, allowing the resolution of the whole gravity-wave spectrum. Momentum fluxes associated with gravity waves were inferred from the balloons measurements, in two different frequency bands: a "wide frequency" (WF) with periods from 15 min to 1 day, and a "high frequency" (HF) with periods from 15 min to 1 h. In order to study the link between wave activity and convection, the convective context of the observations was inferred thanks to maps of brightness temperature, with convective cells localized by a brightness temperature ≤ 235 K.
First, the case study (wave event) of January 15th 2020, during which the balloon 01_STR1 was flying over a major convective system east of the Solomon Islands, provided a clear observation of gravity-wave generation by convection, preferentially during the development of the convective system.
Then, still at a synoptic scale, we highlighted the dependency of wave amplitude to the distance from the nearest convective system. We found not only a monotonic decrease of the amplitude when moving away from the convection, but an even stronger decrease for high frequency waves, which propagation is more vertical. Statistically, 90% of the above-average

momentum fluxes was measured within 400 km of the convection. This is clear confirmation that convection is the primary source of gravity waves at the tropics. At last, the variability of momentum fluxes decreases with distance to convection, highlighting the intermittency of the sources and some background value (around 4 mPa for the "WF" interval) far from convective systems.
At the planetary scale, we found a concomitant geographical behavior of convection and gravity wave activity, with higher momentum fluxes recorded where convection is most active. Tropical convection is observed to be ubiquitous, with more than half of the measurements within 200 km of a convective cell, and a quarter within 50 km. This contributes to decrease the overall intermittency of tropical gravity waves, calculated with the weight of the 10% highest values on the mean value. Therefore, the measured global intermittency is quite low compared to extratropical observations, despite the intermittency of the sources.
At last, we highlighted the importance of short period gravity waves as the average value of momentum flux for the "WF" range was carried by waves with periods between 15 min and 1 h at the level of 30%. The intermittency and the relative contributions of "HF" to "WF" are both consistent with the -1 dependency with intrinsic frequency found for gravity wave momentum fluxes (Podglajen et al., 2016).
The comparison results at the planetary scale between C0 and C1 showed the robustness of our results, with comparable values in the most active convective regions, and differences that could be explained by different planetary scale convective configurations.

A second question raised was to quantify the contribution of the observed gravity waves to the QBO forcing. Both campaigns took place in the eastward phase of the QBO, a little closer to the transition phase for the second campaign, with slightly weaker winds, but this did not drastically change our results. We calculated for C0 that the measured gravity waves were responsible for up to half of the forcing to drive this oscillation.

This thesis has thus allowed a first exploration of the gravity waves momentum fluxes in the lower stratosphere and their relation to the surrounding flow. The method used was a direct comparison between observations, which can therefore serve as a reference or validation for the convective gravity-wave parameterizations in climate models. A first possible improvement is the choice of the convection metric for gravity-wave generation.
We used the distance to the nearest convective cell because it is a simple criterion clearly indicative of what we thought was important (convection in the vicinity). Yet, this criterion has shown limitations because it does not take into account the structure of the convective environment. For instance it does not differentiate if there is one or more convective cells around. Another approach would be to use the variance of the convection calculated in a disk around the position of the balloon, which radius would remain to be defined.
The direction of the gravity waves should also be more looked at: one expects an influence on the waves by the direction of the wind between the main centers of tropospheric convection and the gravity wave signatures. More precisely, more intense waves upstream of convection, especially if there are strong winds. Therefore, another lead for the observation of gravity-wave direction of propagation would be to take into account the wind shear between the

surrounding convection and the balloons. At last, it would be interesting to conduct the same analysis with a different phase, i.e with a different background wind filter and to assess again the gravity-wave contribution to the QBO driving.

5.2 Gravity waves impact on TTL in-situ cirrus clouds

The second chapter of this thesis investigates the effect of gravity waves on in-situ formed TTL cirrus clouds. Our approach to address this question is to use idealized simulations of microphysics combined to lagrangian gravity waves observations from the balloons. Simple experiments are explored with a model precise enough to assess the impact on microphysical characteristics, essential to understand the life cycle of cirrus and the drying of the air masses.

Dinh and Durran microphysical box model is a representation of the microphysics in 0 dimensions. We extended it into a 1.5D representation, to assess the effect of sedimentation and some crude horizontal mixing. The microphysical scheme represents homogeneous nucleation and diffusional growth of the ice particles, in 36 size bins from ∼0.2 to ∼100 microns. In the interest of clarity in the illustration of the processes affecting our results, we present different simulations increasing in complexity: first, a simple ascent of an air parcel, then the addition of dimensions on the vertical and horizontal with columns of air parcels, allowing the sedimentation and horizontal mixing of crystals by wind shear. In all simulations, the air masses follow a vertical "background" temperature profile, inferred from radiosonde measurements, at a low speed of 0.5 mm/s, typical of a large-scale ascent speed in the TTL. Wave-induced temperature fluctuations are directly derived from the Stratéole-2 balloon observations and can be superposed on this mean ascent.

These simulations, and the modeling framework in general are designed to explore the interplay of the different processes at stake in shaping the properties of in-situ cirrus clouds near the tropical tropopause, namely nucleation, growth, and sedimentation of crystals, gravity waves and differential advection in the vertical.

We highlighted the role of sedimentation in shaping the ice crystal population and on the related air parcel dehydration with two complementary simple simulations, representing respectively a perfect and a differential sedimentation of ice crystals. In these simulations, air parcels were not impacted by gravity-waves and the nucleated ice crystals were either falling according to their terminal velocity or simply removed from the simulation. These simulations show the importance of the crystal fall streaks. In a supersaturated environment, sedimenting crystals are able to grow much larger than sizes reached during or soon after nucleation. They contribute to dehydrate the atmosphere over an altitude range much larger than that of the nucleating layer.

Then, a first question was to quantify the impact of gravity waves on ice production, ice crystals density and population.
We addressed it by comparing two similar simulations representing the ascent of air parcels

distributed among several columns, with one of them describing as well the impact of wave-driven temperature variability. Without gravity waves, no ice crystals nucleation is possible above the cold point tropopause. The low cooling rates generate a rather narrow ice crystal population, peaking at 9 microns, which doesn't compare well to observations. In contrast, in the simulation with waves, ice production is increased with many nucleation events generated, at all altitudes. The increase in nucleation events and ice crystal density is a direct consequence of the wave-induced increased cooling rates. The size distribution of the ice crystal population is broadened by the production of crystals at different times with a wider spectrum of cooling rates, up to 4 K/h. This new distribution is closer to the ATTREX observations, although no cloud condensation nuclei were included in the simulations. These results tend to show the importance of a realistic representation of gravity waves to reproduce TTL cirrus observations. Last, we have found that gravity waves significantly increase the cloud fraction near the cold point tropopause. But a more accurate study of this increase would require less idealized simulations.

A second question that we addressed relates to the corresponding wave impact on the dehydration of air parcels.
In the simulation without the waves, the dehydration is rather small with RH_i decreasing only of a few percents, associated with a poor production of ice crystals. Dehydration near the cold point tropopause is almost zero despite initial conditions near nucleation. On the other hand, the highly enhanced ice production by gravity waves has the effect of restoring RH_i to 1 very efficiently. Waves are associated with a 20% decrease in the water vapor mixing ratio for air masses that have penetrated the stratosphere. Overall, the wave-induced dehydration at the cold point is about 2 ppmv. At last, we found that the many small crystals generated by the waves and advected with the air masses may not impact the dehydration directly, but can stop the growth of the incoming crystals that sediment out of higher air mass and thus reduce their dehydration efficiency.

Observations showed a mean standard deviation of 1.5 K of the wave driven temperature fluctuations. As the increase of cooling rates by gravity waves is determinant in the ice production, the impact of its evolution with gravity waves amplitudes was also addressed. First, we carried out a small change on the observed time series of T' by constraining each of them to the same standard deviation of 1.5 K. This increases the occurrence of ice concentration between 1 and 100 crystals/L, but decreases the occurrence of larger concentrations. Indeed, those large concentrations are created in the simulation where the standard deviation can vary between air masses, in air masses that experience the largest wave temperature disturbances. This new simulation produced ice densities even closer to observations. Second, we found that decreasing the standard deviation to 0.5 K gives closer results to the simulation without waves, but allows nucleation above the cold point tropopause. This case limits the impact of the waves and might be more representative of a flow impacted by other dynamic structures such as planetary scales waves. On the other hand, increasing wave amplitude with a standard deviation of 3 K, like increasing their frequency, generate larger cooling rates. The increase in amplitude shifts the peak of the distributions to smaller sizes, but only slightly

when varying from 1.5 to 3 K.

Last, we wanted to also address the effect of waves on cloud structure. First we explored two opposite simple situations, with the effect of gravity waves completely uncorrelated or correlated from one air mass to another, knowing that a situation closer to the TTL conditions would be between the two experiments. When wave-induced temperature fluctuations are completely uncorrelated from one air mass to the other, cirrus clouds appear randomly in the whole simulated domain. The structure of the cloud is highly heterogeneous and random, different from cirrus observations. The temperature fluctuations associated with gravity-waves allow the creation of pockets of high ice crystals concentration, in which RH_i is close to 1, which might remind some profiles of the ATTREX campaigns observations. On the other hand, when temperature fluctuations are correlated between the air parcels, cirrus clouds appear at definite time periods with a more homogeneous structure. This case might be closer to reality given the vertical wavelength of gravity waves. A more layered structure is also found with the decrease of the wave amplitude or the correlation of the fluctuations. In this case, longer simulations might allow to represent finer clouds.

As a general conclusion, our results show the importance of a coupled treatment of TTL gravity waves observations and microphysics. They showed the crucial representation of small scale variability to assess tropical cirrus clouds properties and life cycle.

Our simulations are limited by their simplicity. Regarding the physics of the setup, it was limited by the oversimplified motion of air parcels. It was also limited by the non well constrained correlation of the impact of gravity waves on air parcels, and the limited amount of processes represented. At last, some simulations were calling for more trials to reduce the sensitivity to details of the temperature time series, and longer simulations to assess in a more stable state the long terms impact of waves on cirrus clouds.
To go further, one would like to address the radiative impact of cirrus clouds, especially since the cloud fraction was significantly increased in the presence of gravity-waves. Lidar simulation applied on our results would furthermore enable us to better compare our simulated cirrus with observations and assess their radiative impact, even though the structure of the simulated cirrus clouds should be improved. Another direction for further investigation would be to complement the model with an additional nucleation scheme, like heterogeneous nucleation by adding some ice nuclei that nucleate at a lower supersaturation threshold. We would expect this improvement to reduce the very high ice crystals density and maybe compare better with observations. Although, the uncertainties regarding the nature and characteristics of the numerous ice nuclei might make difficult to conclude on the results. Lastly, it is known that cirrus clouds are formed in cold anomalies of planetary waves, so we could also assess at the impact of the combination of small and large scale waves on ice production.

Bibliography

Alcala, C. M. and Dessler, A. E. (2002). Observations of deep convection in the tropics using the Tropical Rainfall Measuring Mission (TRMM) precipitation radar. *J. Geophys. Res.*, 107:17–1–17–7.

Alexander, M. J., Beres, J. H., and Pfister, L. (2000). Tropical stratospheric gravity wave activity and relationships to clouds. *J. Geophys. Res.*, 105(D17):22299–22309.

Alexander, M. J. and Holton, J. R. (1997). A Model Study of Zonal Forcing in the Equatorial Stratosphere by Convectively Induced Gravity Waves. *J. Atmos. Sci.*, (3):408–419.

Alexander, M. J., Holton, J. R., and Durran, D. R. (1995). The Gravity Wave Response above Deep Convection in a Squall Line Simulation. *J. Atmos. Sci.*, 52:2212–2226.

Alexander, M. J. and Pfister, L. (1995). Gravity wave momentum flux in the lower stratosphere over convection. *Geophys. Res. Lett.*, 22:2029–2032.

Alexander, M. J., Richter, J. H., and Sutherland, B. R. (2006). Generation and trapping of gravity waves from convection with comparison to parameterization. *J. Atmos. Sci.*, 63:2963–2977.

Angell, J. K. and Pack, D. H. (1960). Analysis of some preliminary low-level constant level balloon (tetroon) flights. *Mon. Weather Rev.*, (7):235–248.

Baldwin, M. P., Gray, L. J., Dunkerton, T. J., Hamilton, K., Haynes, P. H., Randel, W. J., Holton, J. R., Alexander, M. J., Hirota, I., Horinouchi, T., Jones, D. B. A., Kinnersley, J. S., Marquardt, C., Sato, K., and Takahashi, M. (2001). The quasi-biennial oscillation. *Rev. Geophys.*, 39:179–229.

Bardeen, C. G., Toon, O. B., Jensen, E. J., Marsh, D. R., and Harvey, V. L. (2008). Numerical simulations of the three-dimensional distribution of meteoric dust in the mesosphere and upper stratosphere. *J. Geophys. Res.*, 113.

Baumgartner, M., Rolf, C., Grooß, J.-U., Schneider, J., Schorr, T., Möhler, O., Spichtinger, P., and Krämer, M. (2022). New investigations on homogeneous ice nucleation: the effects of water activity and water saturation formulations. *Atmos. Chem. Phys.*, 22:65–91.

Beres, J. H., Alexander, M. J., and Holton, J. R. (2002). Effects of tropospheric wind shear on the spectrum of convectively generated gravity waves. *J. Atmos. Sci.*, 59:1805–1824.

Boccara, G., Hertzog, A., Vincent, R. A., and Vial, F. (2008). Estimation of Gravity Wave Momentum Flux and Phase Speeds from Quasi-Lagrangian Stratospheric Balloon Flights. Part I: Theory and Simulations. *J. Atmos. Sci.*, 65:3042–3055.

Boehm, M. T. and Verlinde, J. (2000). Stratospheric influence on upper tropospheric tropical cirrus. *Geophys. Res. Lett.*, 27:3209–3212.

Bony, S., Colman, R., Kattsov, V. M., Allan, R. P., Bretherton, C. S., Dufresne, J.-L., Hall, A., Hallegatte, S., Holland, M. M., Ingram, W., Randall, D. A., Soden, B. J., Tselioudis, G., and Webb, M. J. (2006). How Well Do We Understand and Evaluate Climate Change Feedback Processes? *J. Climate*, 19:3445–3482.

Booker, J. R. and Bretherton, F. P. (1967). The critical layer for internal gravity waves in a shear flow. *J. fluid mechanics*, 27:513–539.

Bramberger, M., Alexander, M. J., Davis, S., Podglajen, A., Hertzog, A., Kalnajs, L., Deshler, T., Goetz, J. D., and Khaykin, S. (2022). First super-pressure balloon-borne fine-vertical-scale profiles in the upper TTL: Impacts of atmospheric waves on cirrus clouds and the QBO. *Geophys. Res. Lett.*, 49.

Bretherton, C. (1988). Group velocity and the linear response of stratified fluids to internal heat or mass sources. *J. Atmos. Sci.*, 45(1):81–94.

Bretherton, C. S. and Smolarkiewicz, P. K. (1989). Gravity Waves, Compensating Subsidence and Detrainment around Cumulus Clouds. *J. Atmos. Sci.*, 46(6):740–759.

Bretherton, F. P. (1964). Low frequency oscillations trapped near the equator. *Dyn. Meteorol. Oceano.*, 16:181.

Brewer, A. W. (1949). Evidence for a world circulation provided by the measurements of helium and water vapour distribution in the stratosphere. *Qu. J. Roy. Meteo. Soc.*, 75:351–363.

Böhm, H. P. (1989). A General Equation for the Terminal Fall Speed of Solid Hydrometeors. *J. Atmos. Sci.*, pages 2419–2427.

Chun, H.-Y. and Baik, J.-J. (1998). Momentum flux by thermally induced internal gravity waves and its approximation for large-scale models. *J. Atmos. Sci.*, 55(21):3299–3310.

Collis, R. T. H., Fernald, F. G., and Alder, J. E. (1968). Lidar Observations of Sierra-Wave Conditions. *J. Applied Meteo.*, (2):227–233.

Corti, T. (2005). Mean radiative energy balance and vertical mass fluxes in the equatorial upper troposphere and lower stratosphere. *Geophys. Res. Lett.*, 32.

Corti, T., Luo, B. P., Fu, Q., Vömel, H., and Peter, T. (2006). The impact of cirrus clouds on tropical troposphere-to-stratosphere transport. *Atmos. Chem. Phys.*, 6:2539–2547.

Cziczo, D. J., DeMott, P. J., Brooks, S. D., Prenni, A. J., Thomson, D. S., Baumgardner, D., Wilson, J. C., Kreidenweis, S. M., and Murphy, D. M. (2004). Observations of organic species and atmospheric ice formation. *Geophys. Res. Lett.*, 31.

de F.Forster, P. M. and Shine, K. P. (2002). Assessing the climate impact of trends in stratospheric water vapor. *Geophys. Res. Lett.*, 29:10–1–10–4.

Dewan, E. M., Picard, R. H., O'Neil, R. R., Gardiner, H. A., Gibson, J., Mill, J. D., Richards, E., Kendra, M., and Gallery, W. O. (1998). MSX satellite observations of thunderstorm-generated gravity waves in mid-wave infrared images of the upper stratosphere. *Geophys. Res. Lett.*, (7):939–942.

Dinh, T. and Durran, D. R. (2012). A hybrid bin scheme to solve the condensation/evaporation equation using a cubic distribution function. *Atmos. Chem. Phys.*, 12:1003–1011.

Dinh, T. and Fueglistaler, S. (2014). Microphysical, radiative, and dynamical impacts of thin cirrus clouds on humidity in the tropical tropopause layer and lower stratosphere. *Geophys. Res. Lett.*, 41:6949–6955.

Dinh, T., Podglajen, A., Hertzog, A., Legras, B., and Plougonven, R. (2016). Effect of gravity wave temperature fluctuations on homogeneous ice nucleation in the tropical tropopause layer. *Atmos. Chem. Phys.*, 16:35–46.

Dunkerton, T. J. and Crum, F. X. (1995). Eastward propagating ∼2- to 15-day equatorial convection and its relation to the tropical intraseasonal oscillation. *J. Geophys. Res.*, 100:25781.

Ern, M., Preusse, P., Alexander, M. J., and Warner, C. D. (2004). Absolute values of gravity wave momentum flux derived from satellite data. *J. Geophys. Res.*

Fovell, R., Durran, D., and Holton, J. R. (1992). Numerical Simulations of Convectively Generated Stratospheric Gravity Waves. *J. Atmos. Sci.*, 49:1427–1442.

Frank, W. M. and Roundy, P. E. (2006). The role of tropical waves in cyclogenesis. *Mon. Weather Rev.*, 134:2397–2417.

Fritts, D. C. (1979). The excitation of radiating waves and kelvin-helmholtz instabilities by the gravity wave-critical level interaction. *J. Atmos. Sci.*, 36(1):12–23.

Fritts, D. C. (1993). *Gravity Wave Sources, Source Variability and Lower and Middle Atmosphere Effects*, pages 191–208. Springer Netherland.

Fritts, D. C. and Alexander, M. J. (2003). Gravity wave dynamics and effects in the middle atmosphere. *Rev. Geophys.*, 41:3–1–3–64.

Froyd, K. D., Murphy, D. M., Sanford, T. J., Thomson, D. S., Wilson, J. C., Pfister, L., and Lait, L. (2009). Aerosol composition of the tropical upper troposphere. *Atmospheric Chemistry and Physics*, 9(13):4363–4385.

Fu, Q. (2007). A new parameterization of an asymmetry factor of cirrus clouds for climate models. *J. Atmos. Sci.*, 64:4140–4150.

Fueglistaler, S. (2005). Stratospheric water vapor predicted from the lagrangian temperature history of air entering the stratosphere in the tropics. *J. Geophys. Res.*, 110(D8).

Fueglistaler, S. and Baker, M. B. (2006). A modelling study of the impact of cirrus clouds on the moisture budget of the upper troposphere. *Atmos. Chem. Phys.*, pages 1425–1434.

Fueglistaler, S., Dessler, A. E., Dunkerton, T. J., Folkins, I., Fu, Q., and Mote, P. W. (2009). Tropical tropopause layer. *Rev. Geophys.*, 47.

Fueglistaler, S., Wernli, H., and Peter, T. (2004). Tropical troposphere-to-stratosphere transport inferred from trajectory calculations. *J. Geophys. Res.*, 109.

Fujiwara, M., Hasebe, F., Shiotani, M., Nishi, N., Vömel, H., and Oltmans, S. J. (2001). Water vapor control at the tropopause by equatorial kelvin waves observed over the galápagos. *Geophys. Res. Lett.*, 28:3143–3146.

Fujiwara, M., Iwasaki, S., Shimizu, A., Inai, Y., Shiotani, M., Hasebe, F., Matsui, I., Sugimoto, N., Okamoto, H., Nishi, N., Hamada, A., Sakazaki, T., and Yoneyama, K. (2009). Cirrus observations in the tropical tropopause layer over the western pacific. *J. Geophys. Res.*, 114.

Fujiwara, M., Kita, K., and Ogawa, T. (1998). Stratosphere-troposphere exchange of ozone associated with the equatorial kelvin wave as observed with ozonesondes and rawinsondes. *J. Geophys. Res.*, 103:19173–19182.

Gage, G. C. R. K. S. (1981). On the annual variation in height of the tropical tropopause. *J. Atmos. Sci.*, pages 1928–1938.

Gardner, C. S. and Shelton, J. D. (1985). Density response of neutral atmospheric layers to gravity wave perturbations. *J. Geophys. Res.*, (A2):1745.

Gettelman, A., Salby, M. L., and Sassi, F. (2002). Distribution and influence of convection in the tropical tropopause region. *J. Geophys. Res.*, 107:ACL 6–1–ACL 6–12.

Gruber, A. (1974). The wavenumber-frequency spectra of satellite-measured brightness in the tropics. *J. Atmos. Sci.*, 31:1675–1680.

Haynes, P. and Shuckburgh, E. (2000). Effective diffusivity as a diagnostic of atmospheric transport: 2. troposphere and lower stratosphere. *J. Geophys. Res.*, 105:22795–22810.

Held, I. M. and Soden, B. J. (2000). Water vapor feedback and global warming. *Ann. Rev. Energy and Envi.*, 25(1):441–475.

Hertzog, A., Basdevant, C., Vial, F., and Mechoso, C. R. (2004). The accuracy of stratospheric analyses in the northern hemisphere inferred from long-duration balloon flights. *Qu. J. Roy. Meteo. Soc.*, 130:607–626.

Hertzog, A., Cocquerez, P., Guilbon, R., Valdivia, J.-N., Venel, S., Basdevant, C., Boccara, G., Bordereau, J., Brioit, B., Vial, F., Cardonne, A., Ravissot, A., and E.Schmitt (2007). Stratéole/Vorcore—Long-duration, Superpressure Balloons to Study the Antarctic Lower Stratosphere during the 2005 Winter. *J. Atmos. Oceanic Technol.*, 24:2048–2061.

Heymsfield, A. J. (2005). Extinction-ice water content-effective radius algorithms for CALIPSO. *Geophys. Res. Lett.*, 32.

Hicks, J. J. and Angell, J. K. (1968). Radar Observations of Breaking Gravitational Waves in the Visually Clear Atmosphere. *J. Applied Meteo.*, (1):114–121.

Holton, J. R. (1972). Waves in the equatorial stratosphere generated by tropospheric heat sources. *J. Atmos. Sci.*, 29:368–375.

Holton, J. R. (1973). On the frequency distribution of atmospheric kelvin waves. *J. Atmos. Sci.*, 30:499–501.

Holton, J. R. (1979). Equatorial wave-mean flow interaction: A numerical study of the role of latitudinal shear. *J. Atmos. Sci.*, 36:1030–1040.

Holton, J. R. (1983). The Influence of Gravity Wave Breaking on the General Circulation of the Middle Atmosphere. *J. Atmos. Sci.*, 40(10):2497–2507.

Holton, J. R., Beres, J. H., and Zhou, X. (2002). On the vertical scale of gravity waves excited by localized thermal forcing. *J. Atmos. Sci.*, 59(12):2019–2023.

Holton, J. R. and Gettelman, A. (2001). Horizontal transport and the dehydration of the stratosphere. *Geophys. Res. Lett.*, 28:2799–2802.

Holton, J. R., Haynes, P. H., McIntyre, M. E., Douglass, A. R., Rood, R. B., and Pfister, L. (1995). Stratosphere-troposphere exchange. *Rev. Geophys.*, 33:403–439.

Homeyer, C. R., McAuliffe, J. D., and Bedka, K. M. (2017). On the development of above-anvil cirrus plumes in extratropical convection. *J. Atmos. Sci.*, 74:1617–1633.

Hoyle, C. R., Luo, B. P., and Peter, T. (2005). The origin of high ice crystal number densities in cirrus clouds. *J. Atmos. Sci.*, 62:2568–2579.

Immler, F., Krüger, K., Fujiwara, M., Verver, G., Rex, M., and Schrems, O. (2008). Correlation between equatorial kelvin waves and the occurrence of extremely thin ice clouds at the tropical tropopause. *Atmos. Chem. Phys.*, 8:4019–4026.

James, R., Bonazzola, M., Legras, B., Surbled, K., and Fueglistaler, S. (2008). Water vapor transport and dehydration above convective outflow during asian monsoon. *Geophys. Res. Lett.*, 35.

Jensen, E. J., Lawson, R. P., Bergman, J. W., Pfister, L., Bui, T. P., and Schmitt, C. G. (2013). Physical processes controlling ice concentrations in synoptically forced, midlatitude cirrus. *J. Geophys. Res.*, 118:5348–5360.

Jensen, E. J. and Pfister, L. (2004). Transport and freeze-drying in the tropical tropopause layer. *J. Geophys. Res.*, 109.

Jensen, E. J., Pfister, L., Ackerman, A. S., Tabazadeh, A., and Toon, O. B. (2001). A conceptual model of the dehydration of air due to freeze-drying by optically thin, laminar cirrus rising slowly across the tropical tropopause. *J. Geophys. Res.*, 106:17237–17252.

Jensen, E. J., Pfister, L., and Bui, T. P. (2012). Physical processes controlling ice concentrations in cold cirrus near the tropical tropopause. *J. Geophys. Res.*, 117.

Jensen, E. J., Pfister, L., Bui, T.-P., Lawson, P., and Baumgardner, D. (2010). Ice nucleation and cloud microphysical properties in tropical tropopause layer cirrus. *Atmos. Chem. Phys.*, 10:1369–1384.

Jensen, E. J., Toon, O. B., Pfister, L., and Selkirk, H. B. (1996). Dehydration of the upper troposphere and lower stratosphere by subvisible cirrus clouds near the tropical tropopause. *Geophys. Res. Lett.*, 23(8):825–828.

Jensen, E. J., Ueyama, R., Pfister, L., Bui, T. V., Alexander, M. J., Podglajen, A., Hertzog, A., Woods, S., Lawson, R. P., Kim, J.-E., and Schoeberl, M. R. (2016). High-frequency gravity waves and homogeneous ice nucleation in tropical tropopause layer cirrus. *Geophys. Res. Lett.*, 43:6629–6635.

Karoly, D. J., Roff, G. L., and Reeder, M. J. (1996). Gravity wave activity associated with tropical convection detected in TOGA COARE Sounding data. *Geophys. Res. Lett.*, 23:261–264.

Kay, J. E. and Wood, R. (2008). Timescale analysis of aerosol sensitivity during homogeneous freezing and implications for upper tropospheric water vapor budgets. *Geophys. Res. Lett.*, 35(10).

Kerr-Munslow, A. M. and Norton, W. A. (2006). Tropical wave driving of the annual cycle in tropical tropopause temperatures. part i: ECMWF analyses. *J. Atmos. Sci.*, 63:1410–1419.

Kiladis, G. N., Wheeler, M. C., Haertel, P. T., Straub, K. H., and Roundy, P. E. (2009). Convectively coupled equatorial waves. *Rev. Geophys.*, 47.

Kim, J.-E. and Alexander, M. J. (2015). Direct impacts of waves on tropical cold point tropopause temperature. *Geophys. Res. Lett.*, 42:1584–1592.

Kim, J.-E., Alexander, M. J., Bui, T. P., Dean-Day, J. M., Lawson, R. P., Woods, S., Hlavka, D., Pfister, L., and Jensen, E. J. (2016). Ubiquitous influence of waves on tropical high cirrus clouds. *Geophys. Res. Lett.*, 43:5895–5901.

Kirk-Davidoff, D. B., Hintsa, E. J., Anderson, J. G., and Keith, D. W. (1999). The effect of climate change on ozone depletion through changes in stratospheric water vapour. *Nature*, 402:399–401.

Knopf, D. A., Alpert, P. A., and Wang, B. (2018). The role of organic aerosol in atmospheric ice nucleation: A review. *Earth Space Chem.*, 2:168–202.

Koop, T. (2004). Homogeneous ice nucleation in water and aqueous solutions. *Zeitschrift für Physikalische Chemie*, 218:1231–1258.

Koop, T. (2015). Atmospheric water. *Water: Fundamentals as the Basis for Understanding the Environment and Promoting Technology*, pages 45–75.

Koop, T., Luo, B., Tsias, A., and Peter, T. (2000). Water activity as the determinant for homogeneous ice nucleation in aqueous solutions. *Nature*, 406:611–614.

Krämer, M., Rolf, C., Spelten, N., Afchine, A., Fahey, D., Jensen, E., Khaykin, S., Kuhn, T., Lawson, P., Lykov, A., Pan, L. L., Riese, M., Rollins, A., Stroh, F., Thornberry, T., Wolf, V., Woods, S., Spichtinger, P., Quaas, J., and Sourdeval, O. (2020). A microphysics guide to cirrus – Part 2: Climatologies of clouds and humidity from observations. *Atmos. Chem. Phys.*, 20:12569–12608.

Krämer, M., Schiller, C., Afchine, A., Bauer, R., Gensch, I., Mangold, A., Schlicht, S., Spelten, N., Sitnikov, N., Borrmann, S., de Reus, M., and Spichtinger, P. (2009). Ice supersaturations and cirrus cloud crystal numbers. *Atmos. Chem. Phys.*, 9:3505–3522.

Kärcher, B. (2003). Simulating gas-aerosol-cirrus interactions: Process-oriented microphysical model and applications. *Atmos. Chem. Phys.*, pages 1645–1664.

Kärcher, B., Dörnbrack, A., and Sölch, I. (2014). Supersaturation Variability and Cirrus Ice Crystal Size Distributions. *J. Atmos. Sci.*, 71:2905–2926.

Kärcher, B., Jensen, E. J., and Lohmann, U. (2019). The Impact of Mesoscale Gravity Waves on Homogeneous Ice Nucleation in Cirrus Clouds. *Geophys. Res. Lett.*, 46:5556–5565.

Kärcher, B. and Lohmann, U. (2002). A parameterization of cirrus cloud formation: Homogeneous freezing of supercooled aerosols. *J. Geophys. Res.*, 107:AAC 4–1–AAC 4–10.

Kärcher, B. and Podglajen, A. (2019). A Stochastic Representation of Temperature Fluctuations Induced by Mesoscale Gravity Waves. *J. Geophys. Res.*, 124:11506–11529.

Lane, T. P., Reeder, M. J., and Clark, T. L. (2001). Numerical Modeling of Gravity Wave Generation by Deep Tropical Convection. *J. Atmos. Sci.*, 58:1249–1274.

Lindzen, R. S. and Holton, J. R. (1968). A theory of the quasi-biennial oscillation. *J. Atmos. Sci.*, 25:1095–1107.

Liu, C. and Zipser, E. J. (2005). Global distribution of convection penetrating the tropical tropopause. *J. Geophys. Res.*, 110.

Lohmann, U. and Roeckner, E. (1995). Influence of cirrus cloud radiative forcing on climate and climate sensitivity in a general circulation model. *J. Geophys. Res.*, 100:16305.

Luo, B. P. (2003). Dehydration potential of ultrathin clouds at the tropical tropopause. *Geophys. Res. Lett.*, 30.

Mace, G. G., Zhang, Q., Vaughan, M., Marchand, R., Stephens, G., Trepte, C., and Winker, D. (2009). A description of hydrometeor layer occurrence statistics derived from the first year of merged cloudsat and CALIPSO data. *J. Geophys. Res.*, 114.

Magee, N., Moyle, A. M., and Lamb, D. (2006). Experimental determination of the deposition coefficient of small cirrus-like ice crystals near -50°c. *Geophys. Res. Lett.*, 33(17).

Mapes, B. E. (1993). Gregarious tropical convection. *J. Atmos. Sci.*, 50(13):2026–2037.

Massie, S., Gettelman, A., Randel, W., and Baumgardner, D. (2002). Distribution of tropical cirrus in relation to convection. *J. Geophys. Res.*, 107:AAC 19–1–AAC 19–16.

Massman, W. J. (1978). On the nature of vertical oscillations of constant volume balloons. *J. Applied Meteo.*, 17:1351–1356.

Matsuno, T. (1966). Quasi-geostrophic motions in the equatorial area. *J. Meteorol. Soc. of Japan. Ser. II*, 44:25–43.

McFarquhar, G. M., Heymsfield, A. J., Spinhirne, J., and Hart, B. (2000). Thin and subvisual tropopause tropical cirrus: Observations and radiative impacts. *J. Atmos. Sci.*, 57:1841–1853.

McLandress, C., Alexander, M. J., and Wu, D. L. (2000). Microwave limb sounder observations of gravity waves in the stratosphere: A climatology and interpretation. *J. Geophys. Res.*, 105(D9):11947–11967.

Mote, P. W., Rosenlof, K. H., McIntyre, M. E., Carr, E. S., Gille, J. C., Holton, J. R., Kinnersley, J. S., Pumphrey, H. C., Russell, J. M., and Waters, J. W. (1996). An atmospheric tape recorder: The imprint of tropical tropopause temperatures on stratospheric water vapor. *J. Geophys. Res.*, 101:3989–4006.

Murata, K.-I. and Tanaka, H. (2013). General nature of liquid–liquid transition in aqueous organic solutions. *Nat. Comm.*, 4.

Murphy, D. M. (2014). Rare temperature histories and cirrus ice number density in a parcel and a one-dimensional model. *Atmos. Chem. Phys.*, 14:13013–13022.

Murphy, D. M. and Koop, T. (2005). Review of the vapour pressures of ice and supercooled water for atmospheric applications. *Qu. J. Roy. Meteo. Soc.*, 131:1539–1565.

Murphy, D. M., Thomson, D. S., and Mahoney, M. J. (1998). In situ measurements of organics, meteoritic material, mercury, and other elements in aerosols at 5 to 19 kilometers. *Science*, 282:1664–1669.

Murray, B. J., Wilson, T. W., Dobbie, S., Cui, Z., Al-Jumur, S. M. R. K., Möhler, O., Schnaiter, M., Wagner, R., Benz, S., Niemand, M., Saathoff, H., Ebert, V., Wagner, S., and Kärcher, B. (2010). Heterogeneous nucleation of ice particles on glassy aerosols under cirrus conditions. *Nature Geoscience*, 3:233–237.

Nachbar, M., Duft, D., and Leisner, T. (2019). The vapor pressure of liquid and solid water phases at conditions relevant to the atmosphere. *J. of Chemi. Phy.*, 151:064504.

Nastrom, G. D. (1980). The response of superpressure balloons to gravity waves. *J. Applied Meteo.*, (8):1013–1019.

Nesbitt, S. W. and Zipser, E. J. (2003). The diurnal cycle of rainfall and convective intensity according to three years of TRMM measurements. *J. Climate*, 16(10).

Newell, R. E. and Gould-Stewart, S. (1981). A stratospheric fountain? *J. Atmos. Sci.*, 38:2789–2796.

Norton, W. A. (2006). Tropical wave driving of the annual cycle in tropical tropopause temperatures. part II: Model results. *J. Atmos. Sci.*, 63:1420–1431.

Ortland, D. A. and Alexander, M. J. (2014). The Residual-Mean Circulation in the Tropical Tropopause Layer Driven by Tropical Waves. *J. Atmos. Sci.*, 71:1305–1322.

Pfister, L., Chan, K. R., Bui, T. P., Bowen, S., Legg, M., Gary, B., Kelly, K., Proffitt, M., and Starr, W. (1993a). Gravity waves generated by a tropical cyclone during the STEP tropical field program: A case study. *J. Geophys. Res.*, 98(D5):8611–8638.

Pfister, L., Scott, S., Loewenstein, M., Bowen, S., and Legg, M. (1993b). Mesoscale Disturbances in the Tropical Stratosphere Excited by Convection: Observations and Effects on the Stratospheric Momentum Budget. *J. Atmos. Sci.*, 50:1058–1075.

Pfister, L., Selkirk, H. B., Jensen, E. J., Schoeberl, M. R., Toon, O. B., Browell, E. V., Grant, W. B., Gary, B., Mahoney, M. J., Bui, T. V., and Hintsa, E. (2001). Aircraft observations of thin cirrus clouds near the tropical tropopause. *J. Geophys. Res.*, 106:9765–9786.

Piani, C., Durran, D., Alexander, M. J., and Holton, J. R. (2000). A numerical study of three-dimensional gravity waves triggered by deep tropical convection and their role in the dynamics of the QBO. *J. Atmos. Sci.*, 57:3689–3702.

Plumb, R. A. (1982). The circulation of the middle atmosphere. *Aust. Meteor. Mag.*, (30):107–121.

Plumb, R. A. (1996). A "tropical pipe" model of stratospheric transport. *J. Geophys. Res.*, 101:3957–3972.

Plumb, R. A. (2002). Stratospheric transport. *J. Meteorol. Soc. of Japan. Ser. II*, 80:793–809.

Podglajen, A., Hertzog, A., Plougonven, R., and Legras, B. (2016). Lagrangian temperature and vertical velocity fluctuations due to gravity waves in the lower stratosphere. *Geophys. Res. Lett.*, 43:3543–3553.

Podglajen, A., Plougonven, R., Hertzog, A., and Jensen, E. (2018). Impact of gravity waves on the motion and distribution of atmospheric ice particles. *Atmos. Chem. Phys.*, pages 10799–10823.

Potter, B. E. and Holton, J. R. (1995). The role of monsoon convection in the dehydration of the lower tropical stratosphere. *J. Atmos. Sci.*, 52:1034–1050.

Prasad, A. A., Sherwood, S. C., Reeder, M. J., and Lane, T. P. (2019). Rapidly evolving cirrus clouds modulated by convectively generated gravity waves. *J. Geophys. Res.*

Pruppacher, H. R., Klett, J. D., and Wang, P. K. (1998). Microphysics of clouds and precipitation. *Aerosol Science and Tech.*, 28:381–382.

Rabier, F., Cohn, S., Cocquerez, P., Hertzog, A., Avallone, L., Deshler, T., Haase, J., Hock, T., Doerenbecher, A., Wang, J., Guidard, V., Thépaut, J.-N., Langland, R., Tangborn, A., Balsamo, G., Brun, E., Parsons, D., Bordereau, J., Cardinali, C., Danis, F., Escarnot, J.-P., Fourrié, N., Gelaro, R., Genthon, C., Ide, K., Kalnajs, L., Martin, C., Meunier, L.-F., Nicot, J.-M., Perttula, T., Potts, N., Ragazzo, P., Richardson, D., Sosa-Sesma, S., and Vargas, A. (2013). The concordiasi field experiment over antarctica: First results from innovative atmospheric measurements. *Bull. Am. Meteorol. Soc.*, 94(3):ES17–ES20.

Randel, W. J., Garcia, R., and Wu, F. (2008). Dynamical balances and tropical stratospheric upwelling. *J. Atmos. Sci.*, 65:3584–3595.

Randel, W. J., Garcia, R. R., and Wu, F. (2002). Time-dependent upwelling in the tropical lower stratosphere estimated from the zonal-mean momentum budget. *J. Atmos. Sci.*, 59:2141–2152.

Randel, W. J., Wu, F., Vömel, H., Nedoluha, G. E., and Forster, P. (2006). Decreases in stratospheric water vapor after 2001: Links to changes in the tropical tropopause and the brewer-dobson circulation. *J. Geophys. Res.*, 111.

Reed, R. J. and Vicek, C. L. (1969). The annual temperature variation in the lower tropical stratosphere. *J. Atmos. Sci.*, pages 163–167.

Ren, C., MacKenzie, A. R., Schiller, C., Shur, G., and Yushkov, V. (2007). Diagnosis of processes controlling water vapour in the tropical tropopause layer by a lagrangian cirrus model. *Atmos. Chem. Phys.*, 7:5401–5413.

Robinson, G. D. (1980). The transport of minor atmospheric constituents between troposphere and stratosphere. *Qu. J. Roy. Meteo. Soc.*, 106:227–253.

Rosenfield, J. E., Considine, D. B., Schoeberl, M. R., and Browell, E. V. (1998). The impact of subvisible cirrus clouds near the tropical tropopause on stratospheric water vapor. *Geophys. Res. Lett.*, 25:1883–1886.

Rosenlof, K. H. (1995). Seasonal cycle of the residual mean meridional circulation in the stratosphere. *J. Geophys. Res.*, 100:5173.

Salby, M. L. and Garcia, R. R. (1987). Transient Response to Localized Episodic Heating in the Tropics. Part I: Excitation and Short-Time Near-Field Behavior. *J. Atmos. Sci.*, 44(2):458–498.

Sato, K., Hashiguchi, H., and Fukao, S. (1995). Gravity waves and turbulence associated with cumulus convection observed with the UHF/VHF clear-air doppler radars. *J. Geophys. Res.*, (D4):7111–7119.

Schoeberl, M., Dessler, A., Ye, H., Wang, T., Avery, M., and Jensen, E. (2016). The impact of gravity waves and cloud nucleation threshold on stratospheric water and tropical tropospheric cloud fraction. *Earth and Space Sci.*, 3(8):295–305.

Schoeberl, M. R. and Dessler, A. E. (2011). Dehydration of the stratosphere. *Atmos. Chem. Phys.*, 11:8433–8446.

Sherwood, S. C. (1999). On moistening of the tropical troposphere by cirrus clouds. *J. Geophys. Res.*, 104:11949–11960.

Shimizu, A. and Tsuda, T. (1997). Characteristics of kelvin waves and gravity waves observed with radiosondes over indonesia. *J. Geophys. Res.*, 102(D22):26159–26171.

Shutts, G. J. and Gray, M. E. B. (1994). A numerical modelling study of the geostrophic adjustment process following deep convection. *Qu. J. Roy. Meteo. Soc.*, 120(519):1145–1178.

Skrotzki, J., Connolly, P., Schnaiter, M., Saathoff, H., Möhler, O., Wagner, R., Niemand, M., Ebert, V., and Leisner, T. (2013). The accommodation coefficient of water molecules on ice – cirrus cloud studies at the AIDA simulation chamber. *Atmos. Chem. Phys.*, 13(8).

Smith, W. L., Ackerman, S., Revercomb, H., Huang, H., DeSlover, D. H., Feltz, W., Gumley, L., and Collard, A. (1998). Infrared spectral absorption of nearly invisible cirrus clouds. *Geophys. Res. Lett.*, 25:1137–1140.

Solomon, S., Garcia, R. R., Rowland, F. S., and Wuebbles, D. J. (1986). On the depletion of antarctic ozone. *Nature*, 321:755–758.

Solomon, S., Rosenlof, K. H., Portmann, R. W., Daniel, J. S., Davis, S. M., Sanford, T. J., and Plattner, G.-K. (2010). Contributions of Stratospheric Water Vapor to Decadal Changes in the Rate of Global Warming. *Science*, 327:1219–1223.

Song, I.-S., Chun, H.-Y., and Lane, T. P. (2003). Generation mechanisms of convectively forced internal gravity waves and their propagation to the stratosphere. *J. Atmos. Sci.*, 60:1960–1980.

Spang, R., Eidmann, G., Riese, M., Offermann, D., Preusse, P., Pfister, L., and Wang, P.-H. (2002). CRISTA observations of cirrus clouds around the tropopause. *J. Geophys. Res.*, 107:CRI 2–1–CRI 2–18.

Spichtinger, P. and Gierens, K. M. (2009). Modelling of cirrus clouds – part 1b: Structuring cirrus clouds by dynamics. *Atmos. Chem. Phys.*, 9:707–719.

Spichtinger, P. and Krämer, M. (2013). Tropical tropopause ice clouds: a dynamic approach to the mystery of low crystal numbers. *Atmos. Chem. Phys.*, 13(19):9801–9818.

Stephan, C. and Alexander, M. J. (2015). Realistic simulations of atmospheric gravity waves over the continental U.S. using precipitation radar data. *J. Adv. Mod. Earth Syst.*, 7(2):823–835.

Straub, K. H. and Kiladis, G. N. (2003). Interactions between the boreal summer intraseasonal oscillation and higher-frequency tropical wave activity. *Mon. Weather Rev.*, 131:945–960.

Straub, K. H., Kiladis, G. N., and Ciesielski, P. E. (2006). The role of equatorial waves in the onset of the south china sea summer monsoon and the demise of el niño during 1998. 42:216–238.

Taylor, J. R., Randel, W. J., and Jensen, E. J. (2011). Cirrus cloud-temperature interactions in the tropical tropopause layer: a case study. *Atmos. Chem. Phys.*, 11:10085–10095.

Thompson, A. M., Allen, A. L., Lee, S., Miller, S. K., and Witte, J. C. (2011). Gravity and rossby wave signatures in the tropical troposphere and lower stratosphere based on southern hemisphere additional ozonesondes (SHADOZ), 1998–2007. *J. Geophys. Res.*, 116.

Thornberry, T. D., Rollins, A. W., Avery, M. A., Woods, S., Lawson, R. P., Bui, T. V., and Gao, R.-S. (2017). Ice water content-extinction relationships and effective diameter for TTL cirrus derived from in situ measurements during ATTREX 2014. *J. Geophys. Res.*, 122:4494–4507.

Toon, O. B., Turco, R. P., Westphal, D., Malone, R., and Liu, M. (1988). A multidimensional model for aerosols: Description of computational analogs. *J. Atmos. Sci.*, 45:2123–2144.

Torrence, C. and Compo, G. P. (1998). A Practical Guide to Wavelet Analysis. *Bull. Am. Meteorol. Soc.*, 79:61–78.

Trier, S. B. and Sharman, R. D. (2016). Mechanisms influencing cirrus banding and aviation turbulence near a convectively enhanced upper-level jet stream. *Mon. Weather Rev.*, 144:3003–3027.

Tsuda, T., Murayama, Y., Wiryosumarto, H., Harijono, S. W. B., and Kato, S. (1994). Radiosonde observations of equatorial atmosphere dynamics over Indonesia: 2. Characteristics of gravity waves. *J. Geophys. Res.*, (D5):10507.

Ueyama, R., Jensen, E. J., Pfister, L., and Kim, J.-E. (2015). Dynamical, convective, and microphysical control on wintertime distributions of water vapor and clouds in the tropical tropopause layer. *J. Geophys. Res.*, 120.

Vincent, R. A. and Alexander, M. J. (2000). Gravity waves in the tropical lower stratosphere: An observational study of seasonal and interannual variability. *J. Geophys. Res.*, 105(D14):17971–17982.

Vincent, R. A. and Hertzog, A. (2014). The response of superpressure balloons to gravity wave motions. *Atmos. Meas. Tech.*, 7:1043–1055.

Virts, K. S., Wallace, J. M., Fu, Q., and Ackerman, T. P. (2010). Tropical tropopause transition layer cirrus as represented by CALIPSO lidar observations. *J. Atmos. Sci.*, 67:3113–3129.

Wang, P.-H., Minnis, P., McCormick, M. P., Kent, G. S., and Skeens, K. M. (1996). A 6-year climatology of cloud occurrence frequency from stratospheric aerosol and gas experiment II observations (1985-1990). *J. Geophys. Res.*, 101(D23):29407–29429.

Wang, T. and Dessler, A. E. (2012). Analysis of cirrus in the tropical tropopause layer from CALIPSO and MLS data: A water perspective. *J. Geophys. Res.*, 117.

Webster, P. J. (1972). Response of the tropical atmosphere to local, steady forcing. *Monthly Weather Review*, 100:518–541.

Yoshida, K. (1959). A theory of the cromwell current (the equatorial undercurrent) and of the equatorial upwelling. *J. of Oceano. Soc. of Japan*, 15:159–170.

Yulaeva, E., Holton, J. R., and Wallace, J. M. (1994). On the cause of the annual cycle in tropical lower-stratospheric temperatures. *J. Atmos. Sci.*, pages 169–174.

Zangvil, A. (1975). Temporal and spatial behavior of large-scale disturbances in tropical cloudiness deduced from satellite brightness data. *Mon. Weather Rev.*, 103:904–920.

Zangvil, A. and Yanai, M. (1980). Upper tropospheric waves in the tropics. part i: Dynamical analysis in the wavenumber-frequency domain. *J. Atmos. Sci.*, 37:283–298.

Zangvil, A. and Yanai, M. (1981). Upper tropospheric waves in the tropics. part II. association with clouds in the wavenumber-frequency domain. *J. Atmos. Sci.*, 38:939–953.

Zhou, X. and Wang, B. (2007). Transition from an eastern pacific upper-level mixed rossby-gravity wave to a western pacific tropical cyclone. *Geophys. Res. Lett.*, 34.

Chapter 6

Communications related to this PhD thesis

Scientific papers:

- **Corcos, M.**, Hertzog, A., Plougonven, R., Podglajen, A., Observation of Gravity Waves at the Tropical Tropopause Using Superpressure Balloons. *JGR Atmospheres*, 2021, `https://doi.org/10.1029/2021JD035165`.

- **Corcos, M.**, Hertzog, A., Plougonven, R., Podglajen, A., A simple model to assess the impact of gravity waves on ice crystal populations in the Tropical Tropopause Layer. *ACP*, 2021, in review.

International conferences:

Posters

- **Corcos, M.**, Hertzog, A., Plougonven, R., Podglajen, A., A Simple model to asses gravity waves impact on ice crystals population at the TTL *EGU General Assembly Conference*, 2022.

- **Corcos, M.**, Hertzog, A., Plougonven, R., Podglajen, A., Observation of gravity waves at the Tropical Tropopause Layer using Stratéole-2 superpressure balloons. *Journées Jeune Chercheurs CNES*, 2022.

- **Corcos, M.**, Hertzog, A., Plougonven, R., Podglajen, A., Observation of gravity waves at the Tropical Tropopause Layer using Stratéole-2 superpressure balloons. *AMS General Assembly Conference*, 2022.

- **Corcos, M.**, Hertzog, A., Plougonven, R., Podglajen, A., Quantification of tropical gravity waves using high resolution balloons.*EGU General Assembly Conference*, 2021.

Talks

- **Corcos, M.**, Hertzog, A., Plougonven, R., Podglajen, A., Observation of gravity waves at the Tropical Tropopause Layer using Stratéole-2 superpressure balloons. *SPARC gravity waves*, 2022.
- **Corcos, M.**, Hertzog, A., Plougonven, R., Podglajen, A., Observation of gravity waves at the Tropical Tropopause Layer using Stratéole-2 superpressure balloons.*25th ESA Symposium balloons and rockets*, 2021.

Invited seminars:

- **Corcos, M.**, Hertzog, A., Plougonven, R., Podglajen, A., Observation of Tropical Gravity Waves : Use of superpressure balloons of Stratéole-2. *Journal Club of Rice University, Standford Univeristy, NCAR Boulder*, 2021.
- **Corcos, M.**, Hertzog, A., Plougonven, R., Podglajen, A., A simple model to assess the impact of gravity waves on ice crystals populations in the Tropical Tropopause Layer. *NOAA (National Oceanic and Atmospheric Administrator)*, 2022.
- **Corcos, M.**, Hertzog, A., Plougonven, R., Podglajen, A., Observation of Gravity Waves at the Tropical Tropopause Using Superpressure Balloons. *Max Planck Institute*, 2022.